Calcium dynamics in signaling micro domains of cardiac myocytes

- a modelling study

by
Johan Hake

Thesis submitted for the degree of Philosophiae Doctor
Department of Informatics
Faculty of Mathematics and Natural Sciences
University of Oslo
October 2009

Preface

This thesis is submitted in partial fulfillment of the requirements for the degree of Philosophiae Doctor, to the Department of Informatics, Faculty of Mathematics and Natural Sciences, University of Oslo. All research has been conducted at the Center for Biomedical Computing, at Simula Research Laboratory, during the period between August 2005 and July 2009. In this period I had paternity leave for a total duration of 4 month. I would like to express my gratitude to Simula for financial support, and for excellent working conditions.

Several people, to whom I am very grateful, have contributed to this work. First, I want to mention my supervisors Dr Glenn Lines, Dr Joakim Sundnes and Prof. Ole Sejersted. A special thanks go to Glenn for his patient, availability and for his clear thought. I also want to thank my co-supervisor Ole, whom I have had a few but very enlightening discussions with. I am grateful, for having worked in the Department of Scientific computing, under the visionary leadership of Prof. Hans Petter Langtangen. As an employee of Simula I also stand in gratitude to Prof. Aslak Tveito, who's resolute and clear leadership, has paved the way for the phenomenal working environment of Simula. Thanks also to the FEniCS project and all its members. A special thanks in this regard goes to Anders Logg for his steady and clear vision, Martin Alnäs for his critical views, and Ola Skavhaug and Kent Andre Mardal, for sharing their knowledge of the deep magic of SWIG. I am grateful for the few moments I have been able to share my thoughts with Dr. William Louch, who's enthusiastic approach to science has given me much. It is also natural to thank my friend, former supervisor, nad neighbour Dr. Hans Ekkhard Plesser, whom also gave me the advice to apply for a PhD position at Simula.

Finally to my beloved girls: Hanna, Emma and Jorunn, to whom I owe everything.

Johan Hake, Oslo, July 2009

Contents

List of Papers

- **Paper I**

Stochastic binding of Ca^{2+} ions in the dyadic cleft; continuous versus random walk description of diffusion
J. Hake, G. T. Lines
Biophys. J. 94, 4184, 2008.

- **Paper II**

A coupled stochastic and deterministic model of Ca^{2+} dynamics in the dyadic cleft
J. Hake
Submitted for publication in:
Logg A., Mardal K. and Wells G. (Ed.)
Automated Scientific Computing
Coming at Springer in Autumn 2009

- **Paper III**

Mechanisms underlying delayed and dyssynchronous Ca^{2+} release in failing cardiomyocytes examined by computer modeling
J. Hake, W. E. Louch, O. M. Sejersted, G. T. Lines
Submitted for publication.

Introduction

Heart failure (HF) is a progressive and chronic disease, characterized by an impaired ability of the heart to fill and pump blood. HF remains a serious health problem throughout the industrialized world [1]. For instance, in the United States alone, over 5 million people currently suffer with HF, and over 600,000 new cases are diagnosed each year [2]. Patients with heart failure suffer severely from the symptoms, and the available treatments are often insufficient.

The precise mechanisms underlying the failing phenotype remain unclear. However, there is general agreement that decreased myocardial function in this condition involves depressed contractility of heart cells (cardiomyocytes). Alterations in cellular Ca^{2+} homeostasis are believed to be central to these alterations [3]. Experimental models of HF is commonly used to study the physiological conditions behind HF [4], and medical treatments can be tested using such models. In recent years, computational studies have emerged as a complement to the experimental ones. Using laws from physics and chemistry, modelers have been able to describe physiological phenomena using mathematical and statistical equations [5]. The computational models can be used to test hypotheses about the function of cardiomyocytes and possible treatments, which cannot be done using experimental models.

In this thesis I will focus on a computational model of Ca^{2+} dynamics in an intracellular sub-domain of a cardiomyocyte that is inaccessible for direct experimental measurements: The dyadic cleft. The thesis consists of this introduction, and three papers. In Paper I, two different models of the diffusion dynamics in the cleft are compared. In Paper II a hybrid stochastic and deterministic approach to model the Ca^{2+} dynamics in the dyadic cleft is presented. In the second part of Paper II I also present a solver that can be used to simulate coupled stochastic and deterministic models: `diffsim`. Finally, in Paper III, results obtained applying this solver to a computational model of the dyadic cleft are presented.

In this introduction of the thesis, I first give a brief physiological background for the Ca^{2+} dynamics in the dyadic cleft. Secondly I review some published computational studies, which models the Ca^{2+} dynamics in the dyadic cleft. In the last part, I present the papers and point to future work. The presentation of the papers will focus on the main findings, and where appropriate, also discuss the results with respect to some of the reviewed studies. In the future work section I discuss how the work can be extended in future studies of the field of modelling the local Ca^{2+} dynamics in the dyadic cleft.

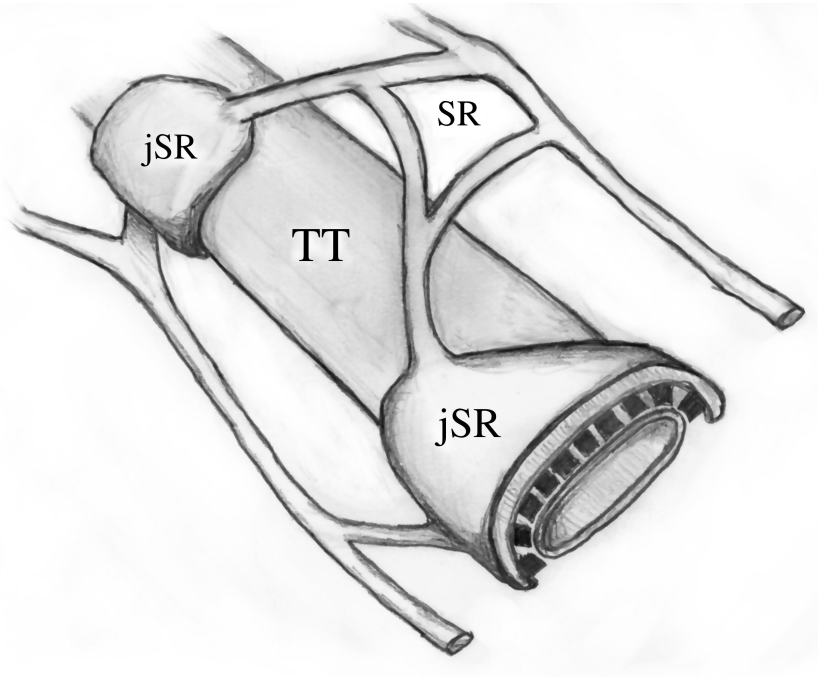

Figure 1: The figure shows the relationship between the TT, the SR and the jSR. The volume between the jSR and the TT defines the dyadic cleft. The black structures in the cleft are Ryanodine receptors. These are large channel proteins from which the Ca^{2+} from the SR is released from.

1 Physiological background

The contraction of a cardiomyocyte is triggered by an electric signal that, for each beat, travels through the heart. This signal propagates using both passive (diffusion) and active (excitation of single cells) properties of the heart tissue. The electric signal lives in the tissue as a potential difference (the membrane potential) between the intra- and extracellular domain of a cardiomyocyte. The membrane potential has a resting value that is negative and commonly found in the range [-85,-60] mV. A negative membrane potential is labelled hyperpolarized, while a positive such is labelled depolarized. The membrane potential is called an action potential (AP) when it is sustained with active properties of the membrane. When an AP arrives a cardiomyocyte, it activates ion channels at the cell membrane (sarcolemma). These ion channels let different ion species either in or out when the channel is open. Most ion channels are ion specific and only let a single type of ion through. The direction of the current is dependent on the electro-chemical gradient across the membrane. The gradient is defined in terms of the membrane potential and the concentration gradients of the particular ion species. The cell membrane of ventricular cardiomyocytes has pipe-like invaginations called transverse tubule (TT). These perforate the cardiomyocyte and, loosely speaking brings the cell membrane into the cell. Ion channels that reside on the TT have direct access, and therefore more effective access, to the interior of the cardiomyocyte.

One particular ion type, Ca^{2+}, is central for the function of the cardiomyocyte. Ca^{2+} controls the force that makes the cardiomyocyte contract and relax during a heart beat. When the Ca^{2+} concentration in the cytosol (the main intracellular domain) is

high, Ca^{2+} binds to contractile proteins and thus contraction is triggered. When the Ca^{2+} concentration is reduced, Ca^{2+} unbinds from the contractile proteins and the cardiomyocyte relaxes. These two phases correlate with the heart functions of systole (contraction) and diastole (relaxation), and they are equally important for the pumping function. The systolic function controls how well the blood is ejected from the heart and the diastolic function controls how much blood the heart can refill with. The main source of Ca^{2+} to the cytosol is from an internal Ca^{2+} container, the sarcoplasmic reticulum (SR). The SR forms a network inside the cardiomyocyte that wraps the contractile proteins. By this arrangement, the distance the Ca^{2+} need to diffuse, is minimized. At the TT, the network like SR, forms larger containers, called junctional SR (jSR). These wrap the TT, as illustrated in Fig.1. The volume between the jSR and the TT defines the narrow ($\sim$ 15 nm [6, 7]) dyadic cleft (also called just a dyad).

Ca^{2+} release from SR is facilitated by a channel called the Ryanodine receptor (RyR). The RyRs are gathered in clusters of up to hundreds of single channels [7]. The opening of these channels is induced by single Ca^{2+} ions attaching to them [8, 9]. This process is commonly known as the Ca^{2+} induced Ca^{2+} release (CICR) [10]. The triggering Ca^{2+} mostly come from the L-type Ca^{2+} channel (LCC). The CICR is tightly controlled in the small volume of the dyadic cleft, known as the local control model [11]. Here, LCCs are situated at the TT opposing the RyRs at the SR. Recent results show that many LCCs need to open several times to trigger a release [12]. This thesis is mostly concerned with the triggering of the Ca^{2+} release. But equally important is the termination of the release, which is not yet well understood [13, 14]. The Ca^{2+} release from a single dyad defines a release event and is commonly called a spark [15]. A single cardiomyocyte consists of tens of thousands of dyads and during the systolic phase, a concerted Ca^{2+} release from these discrete units sums up to the whole cell Ca^{2+} transient, which triggers the contraction of the cardiomyocyte. In a healthy cardiomyocyte, the regularly organized TT network will ensure spatial synchrony of the sparks.

During HF, the cardiomyocyte's ability to contract and relax is impaired. This is caused by an altered Ca^{2+} regulation in the cell [16]. HF leads to a progressive reorganization of the TT, while the cardiomyocyte undergoes hypotrophy [17]. The result is a dyssynchronous and delayed Ca^{2+} activation. Louch et al. [17] correlate areas of disrupted and absent TTs, with areas of delayed Ca^{2+} release. In paper III, we use a detailed computational model to investigate causes of such Ca^{2+} release patterns.

An important modulator of the Ca^{2+} dynamics in the dyadic cleft is a Ca^{2+} buffer and the electric field, both caused by the negatively charged phospholipid head-groups at the sarcolemma [18–20]. The buffer and the electric field do not alter the qualitative understanding of the CICR, but they alter the quantitative modeling of the Ca^{2+} dynamics in the cleft [21, 22]. In paper II, I show how the electric field can be resolved in a computational model of the dyadic cleft.

A second possible modulator of the Ca^{2+} dynamics in the dyad is the Na^+/Ca^{2+} exchanger (NCX). The NCX is a protein that exchanges one Ca^{2+} with three Na^+. NCX is the main Ca^{2+} extractor during the relaxation phase [23]. When the NCX extracts Ca^{2+} from the cell, the NCX is working in forward mode, or in Ca^{2+} efflux mode. In the context of the dyad, it has been proposed that the NCX working in Ca^{2+} influx mode can modulate the timing of the RyR release[24, 25]. In paper III, we use a

computational model to investigate the ability of a single NCX that works in reverse mode, to trigger Ca^{2+} release. It has also been shown that NCXs positioned in the dyad will extract more Ca^{2+} than cytosolic NCXs, due to the higher local Ca^{2+} concentration in the dyad during release [26, 27].

2 Review of computational models

In this section, a brief overview of some of the published models of the Ca^{2+} dynamics in the dyadic cleft is given, together with an explanation of their findings that correlates with the work of this thesis. The models will be presented in chronological order and the list together with each presentation is not exhaustive.

Computational models that are used in studies of the Ca^{2+} dynamics in the dyadic cleft can roughly be categorized into two types: integrative and standalone models. The former type couples the Ca^{2+} dynamics in a single dyad with that of the whole cell. These models are often called multi-scale models as they combine the length and time scales of the Ca^{2+} dynamics in the dyad, to that of a whole cell. These models have been used to couple the discrete nature of spark generation to the continuous nature of whole cell dynamics. The standalone models only model the Ca^{2+} dynamics of a single dyad. In this manner, they can often be more detailed than the integrative models. In this thesis, I have focused on the standalone models. However, the importance of integrative models should also be recognized. In the last section of this introduction, I will discuss strategies for how the standalone model I have considered, can be coupled to a larger intracellular domain.

The models reviewed in this section, can further be divided into discrete and continuous models, depending on how the Ca^{2+} diffusion in the dyad is modeled. Unless otherwise stated, I assume that the diffusion is modeled continuously. In the presentation of Paper I, I will take a closer look at the discrete versus continuous modeling of Ca^{2+} diffusion in the dyad.

Standalone models

Peskoff et al. 1992
To the best of my knowledge, the first standalone model was developed by Peskoff et al. [26]. They models the effect of sarcolemmal binding sites to the Ca^{2+} dynamics in the dyad. The above reference is the second part of a companion study. The first part experimentally quantifies the presence of two different low and high affinity Ca^{2+} buffers at the sarcolemma [20]. For different values of the diffusion constant, they investigate the effect, of including or not including the sarcolemmal buffers, on the RyR release. To be able to solve their equations they reduce the problem to a 1D problem. An interesting observation that is relevant for Paper III, is the effect of using the buffer together with an included NCX. Peskoff et al. [26] show that when sarcolemmal buffers are used in their model, the $\left[Ca^{2+}\right]$ stays at an elevated level longer than if the buffer is not included. This increases the amount of Ca^{2+} extracted from the cardiomyocyte by any present NCX. Even if their model of the NCX and RyR release is simplistic, the results corresponds to some recent model results [27], see below. Peskoff et al. [26] also

conclude that the time constant for the inactivation process of the RyR must be larger than for the activation process. The Ca^{2+} release would otherwise finish to fast.

Langer and Peskoff 1996
Langer and Peskoff [28] consider an updated version of the model from Peskoff et al. [26], with new experimental findings of the sarcolemmal buffers. They also include simulations of the time before the release, using Ca^{2+} influx through both the LCC and from the NCX working in Ca^{2+} influx mode. They claim that a single LCC can raise the Ca^{2+} level to 1 μM within a distance of 50 nm, which should be sufficient to trigger Ca^{2+} release from a cluster of 9 RyRs within 0.5 ms. They further claim that the NCX working in Ca^{2+} influx mode elevates the $\left[Ca^{2+}\right]$ in the cleft to 0.5 μM which should be sufficient to trigger release from the same 9 RyRs within 10 ms. However if the RyRs would be this sensitive to cytosolic $\left[Ca^{2+}\right]$, they would statistically open too often to be functional. Their updated version of the sarcolemmal buffers includes a very slow unbinding rate, causing a relaxation to diastolic $\left[Ca^{2+}\right]$ (~ 0.1 μM) to take 150 ms. This is a long time and has to our knowledge not been repeated in any subsequent studies.

Soeller and Cannell 1997 and *Cannell and Soeller 1997*
The next two studies come from the companion papers of Soeller and Cannell [21] and Cannell and Soeller [29]. In the first paper, they study the Ca^{2+} response in the cleft from an open LCC channel prior to the RyR release. In their second paper, they study the dynamics of the CICR using stochastic modelling of the RyRs. In the first study, they use and develop a previously published model for the electric field in the dyad [30]. They show that the inclusion of the electric field has dramatic effects on the Ca^{2+} level in the dyadic cleft. Without the electric field the steady state Ca^{2+} response from an open LCC at the closest RyR is 158 μM, and with the electric field only 63 μM. The rise time of the $\left[Ca^{2+}\right]$ is also five fold increased with the electric field. They also run simulations using different parameters for the amplitude of the constant LCC current and they vary the size of the cleft.

In their second study, the different $\left[Ca^{2+}\right]$ responses from an open LCC from their first study are used to investigate under what circumstances this responses can trigger Ca^{2+} release from the RyRs [29]. They derive a model for the probability that a RyR will open given the transient $\left[Ca^{2+}\right]$ response from an open LCC, and by this include the discrete and stochastic nature of the RyR channel. Their dyad includes a single LCC and a different number of RyRs at different positions. The $\left[Ca^{2+}\right]$ dependency of the opening kinetics of the RyR model is of second order. They find that it is crucial that the RyR is juxtapositional to the LCC for reliable releases. The cumulative open probability for a RyR facing an open LCC raises towards 1 quite fast: after 0.2 ms, it is already at 0.8. This might be a too high value considering the recent results from Poláková et al. [12], where the coupling fidelity between an open LCC and a RyR is low: ~ 0.15.

Rice et al. 1999
In this study, the integrative behaviour of several dyads (500) is studied. In this sense this study could be classified as an integrative model but it does not provide

any feedback system. They use stochastic models for the included channels. Their model features so called graded release of Ca^{2+} and high gain. The graded release is a feature attributed to local control models, which so called common pool models cannot have [11]. In a common pool model, the volumes of all dyads are lumped into a single compartment. Due to the regenerative nature of CICR, common pool models will respond in an all or nothing manner. However, in cardiomyocytes the Ca^{2+} release is graded with respect to the triggering LCC current. The local control of CICR is introduced to solve this paradox. The gain is the ratio between the Ca^{2+} coming in from the RyRs over the amount of Ca^{2+} coming from the LCCs. In the local control model, the CICR is controlled by the stochastic activation of the RyRs in the thousands of dyads contained within a cardiomyocyte. Here, each dyad can respond in a more or less all or nothing manner and the graded release is attributed to a graded number of recruited dyads in a release.

Rice et al. [31] use a single compartment to model $\left[Ca^{2+}\right]$ in each dyad, assuming no spatial gradients in the cleft. Each cleft has a single LCC and 8 RyRs. They use an LCC model featuring a Ca^{2+} mode that models the Ca^{2+} inactivation developed in a previous study [32]. They use a model for the RyRs that features adaptation [33], which means that the RyRs get less sensitive after consecutive openings [34]. Their model is robust with respect to varying a set of parameters which is a good feature of a complex model.

Lines et al. 2006
In a detailed model of a dyad, Lines et al. [25] show that under certain circumstances an NCX working in Ca^{2+} influx mode can precede the LCC in triggering CICR. Their model is a 2-dimensional model of the dyad where a Ca^{2+} and a Na^{+} domain is coupled by the nonlinear NCX fluxes. They include local LCC and Na^{+} channel fluxes to the dyad by distributing the corresponding whole cell currents, to local channels in the domain. The whole cell currents are acquired from a simultaneously solved cell model of the AP. They find that when a Na^{+} channel and an NCX is colocalized and the diffusion constant is small, modeling the crowdedness of a dyad, Ca^{2+} from the NCX can precede the LCC in triggering Ca^{2+} release from the RyR. In Paper III, an attempt was made to reproduce the results with a more detailed model of the Ca^{2+} and Na^{+} dynamics, without success. This is probably due to differences in the modelling, which is elaborated in the paper.

Koh et al. 2006
The issue of representing few diffusing ions using a continuous representation of the $\left[Ca^{2+}\right]$ is addressed in the study of Koh et al. [35]. They use MCell [36, 37], a Random walk simulator to model the Ca^{2+} diffusion inside the cleft. They develop their own model of the LCC and adapt a published model for the RyR dynamics [38]. The geometry of the cleft is varied and the effect on the spark is registered. They find that the generation and the shape of the spark is not very sensitive to the width of the cleft but highly sensitive to the height. *Koh et al. 2006* also show that the number of participating ions in a cleft is highly variable between single runs, together with the time length of a single spark. The cardiomyocyte needs a reliable Ca^{2+} transient each beat, and they argue that the noise in the signal from each spark has to be integrated.

They therefore investigate how many dyads that has to be employed to get a reliable and noise free Ca^{2+} signal. The number of participating ions in the dyad is used as a measure for this signal. As will be discussed in our paper presentation below, I argue that it is not the number of participating ions that defines the stochasticity of a dyad, but rather the discrete and stochastic states of the included channels.

Tanskanen et al. 2007
The Ca^{2+} dynamics of a dyad is highly dependent on the structure of the dyad. Previous studies has shown that the height of the cleft and the relative position of the channels in the cleft can dramatically alter the Ca^{2+} response from an open Ca^{2+} source in the cleft. Recently we have also got a more precise understanding of the structure of the large proteins in the dyad, both the LCC [39] and the RyR [40]. In a study of the Ca^{2+} dynamics in the dyad, Tanskanen et al. [22] include the structural information of the LCC and RyR proteins in the geometry of the cleft. Similar to Koh et al. [35] they use a fully stochastic and discrete model for the Ca^{2+} dynamics in the whole dyad. Instead of using MCell that does not support electro diffusion, they use a simulator based on a discretized version of the Fokker-Planck equation [41]. In this manner, they include single ion interaction and ion interaction with an external electric field (from the sarcolemma). A dyad with 5 LCCs and 20 RyRs is used in their model. The integrated response from several hundred of such dyads shows the known features of local control of Ca^{2+}, such as graded release and high gain. The integrated gain from several dyads, is used as a measure of the impact of several changes in the model. They show that moving the binding site of Ca^{2+} at the RyRs from the rim of the RyR to the center increases the gain. The gain is also reduced when the proteins structures and the electric field is removed. These two findings are interesting as they point to the importance of local gradients in the dyad, which also will be emphasized in Paper III in this thesis.

Similar to the study of Koh et al. [35] they also show that the amount of Ca^{2+} ions in the cleft varies considerably during a single run. They use this result to demonstrate the stochastic nature of the Ca^{2+} diffusion in such a small volume, and argue that it is more appropriate to use a discrete and stochastic description of the Ca^{2+} diffusion. This argument is also complemented with the results from clever experiments: the gain is measured while scaling the diffusion coefficient together with the amplitude of the Ca^{2+} current from the LCCs and the RyRs. They show that the gain is actually dependent on the scaling factor. If the same experiments were done using a continuous model of diffusion, one would expect the gain not to be dependent on the scaling factor. This is because the continuous $\left[Ca^{2+}\right]$ would stay the same under the scaling. Tanskanen et al. [22] describe this as a *subtle, but potentially significant difference in predicted macroscopic behavior arising from the underlying stochastic simulation of Ca^{2+} motion in the dyad* [22]. I will address this issue further in the presentation of paper I below.

Integrative models

Stern et al. 1999
Stern et al. [42] follow up on the work of Stern [11] where the paradox of graded Ca^{2+} release was first explained and thoroughly examined. With their present study, they

present a model that uses local control of Ca^{2+} demonstrating graded Ca^{2+} release. The model does not integrate a full set of membrane currents, nor does it include a full AP, but it does integrate the whole cell Ca^{2+} handling with the local control of Ca^{2+} release. They model the gating of the LCCs and RyRs stochastically. The states of these channels are collected in a local state vector defining the discrete state of the whole dyad. The diffusional process inside the cleft is described using a partial differential equation which is discretized using a coarse grid ($\Delta x = 10$nm). To reduce computational cost, steady state $\left[Ca^{2+}\right]$ is assumed inside the cleft, reducing the local dynamics of the dyad to a set of discrete states. The number of RyRs they use in each dyad is either 25 or 121. In the more computationally intensive runs, the former number is used.

In their study they test six different models for the RyR gating. Four of the models were taken from the literature of isolated RyRs in lipid bi-layers. None of these schemes seem to work satisfactory, as the RyR did not close in a reliable way, nor opened enough when activated. This points out a still unsettled problem of reconciling RyR models from bi-layer experiments [43] with local control models of Ca^{2+} release. They point out that two features are required to achieve local and global stability: strong inactivation and cooperative activation by binding of more than one Ca^{2+}. The model they finally use is a phenomenological model with a second order $\left[Ca^{2+}\right]$ dependent activation kinetics. Stern [11] also present a solution to the published bi-layer models. They argue that there might be alosteric interaction between RyRs in a cluster. Based on this assumption, they introduced collaborative interaction between the nearest neighbours in a RyR cluster. This addition stabilize a previously unstable model. Interestingly they also point out that using higher order kinetics of the RyR model, hence introducing collaboration at a single RyR level, would also stabilize the model. Note that newer studies also support this assumption [44, 45]. In Paper III we use a fourth order kinetics for the RyR model.

Greenstein and Winslow 2002
Greenstein and Winslow [46] present the first study that integrates local control of Ca^{2+} release in a whole cell model of the canine AP. Each dyad is divided into four equally sized sub domains, with one LCC, five RyRs and one Ca^{2+} dependent transient outward chloride current (Ito2) in each. The four subdomains experience the same lumped $\left[Ca^{2+}\right]$. Their model features both macroscopic (as in single cell) phenomena such as modulation of AP duration by SR Ca^{2+} release, and detailed properties that need local control of Ca^{2+} such as graded release and high gain. In a full model study they use 12500 dyads, but most of their simulations were run using 2500 dyads.

Hinch et al. 2004
In this study, Hinch et al. [47] use a previously developed mathematical model of the spark generation [48] to reduce the heavy stochastic computations of the local control from Greenstein and Winslow [46]. Roughly this is done by reducing the number of channels in a single dyad to one LCC and one RyR. The Markov models describing the dynamics of these channels are reduced to only having two states each, open and closed. The number of discrete states of a single dyad is then given by the number of distinct combinations of the LCC and RyR model states: in total, four states. The $\left[Ca^{2+}\right]$ in the dyadic cleft is assumed being in quasi steady state, depending on only

global parameters ($\left[Ca^{2+}\right]$ in cytosol and in SR), and the discrete state of the dyad. With these assumptions, they have created a representation of a single dyad using only one Markov model, which is dependent on only global variables. This model is then evaluated as a continuous model of the average response of all dyads in a cell. Their model features graded release and high gain, which is typical for local control models.

Greenstein et al. 2006
The reduced model of local control from Hinch et al. [47], is used in the whole cell model from Greenstein and Winslow [46]. Greenstein et al. [49] use a more detailed model of the LCC and RyR, creating a Markov model of the dyad consisting of 40 states instead of 4. They also assume that a single dyad has 5 RyRs. But these are modelled using only one RyR model. They compensate by increasing the Ca^{2+} activation time and single RyR flux by 5. The model has the features of local control models with high gain and graded release.

Williams et al. 2007
In this study, Williams et al. [50] develop a whole cell probability density based model of the local Ca^{2+} control. They propose a multivariate probability density function for the state of a single dyad in a cell. The density function is dependent on the discrete state of the included channels of a dyad, the Ca^{2+} concentration of the dyad, and the Ca^{2+} concentration of the jSR. In their presentation of the model they choose to include one LCC and one RyR, each which could be either open or closed. The number of discrete states of a dyad is then four, which is analogue to the assumptions in Hinch et al. [47]. However, Williams et al. [50] also include a dependency of the local Ca^{2+} concentration of the dyad and the jSR. It is important to note the distinction between the probability density approach this study chooses, and the common pool models of the CICR. The common pool model can also model the Ca^{2+} concentration in the dyadic space and in jSR. However, the common pool model has one Ca^{2+} concentration for all dyads, while the probability density approach, models the probability that a single dyad has a certain local Ca^{2+} concentration. Hence, the model depends on the assumption of modelling the stochastic state of many dyads in the cell, which they show is a reasonable assumption.

With their model, Williams et al. [50] show common features of local control models such as high gain and graded release. They also couples the local Ca^{2+} dynamics to the whole cell $\left[Ca^{2+}\right]$ of the cytosol and network SR. This step makes the model an integrative model. The model they use for the local Ca^{2+} dynamics is from a previous study of the effect of local depletion of Ca^{2+} in jSR to the termination of Ca^{2+} release from SR [51]. This model features reliable terminations of the release only based on depletion of jSR and stochastic attrition of the RyRs. It is therefore important for Williams et al. [50] to include the local $\left[Ca^{2+}\right]$ of the jSR, so this feature is preserved in their integrative model. Last in their study they show that the Ca^{2+} concentration in the dyad is slaved by the present discrete state of the dyad and of the present Ca^{2+} concentration of jSR. This means that they can remove the dependency of the dyadic $\left[Ca^{2+}\right]$ from the probability density function. This reduction greatly speed up the simulations. I think the approach of modelling the spark termination with jSR depletion and slaving the dyadic $\left[Ca^{2+}\right]$ to jSR $\left[Ca^{2+}\right]$ is nice. It is probably an approach I would

look into if I would continue the work on modelling the dyadic Ca^{2+} dynamics.

Sher et al. 2008
The question of the role of NCX in the dyadic cleft is investigated by Sher et al. [27]. They use the whole cell model of Greenstein et al. [49] and modify it by including the $\left[Ca^{2+}\right]$ in the dyad. They split the whole cell NCX current into two parts: one that senses the $\left[Ca^{2+}\right]$ in the cytosol and one that senses the elevated $\left[Ca^{2+}\right]$ of the dyadic cleft. Different fractions of the NCX distribution are investigated. With their modification they find that the NCX is working in reverse mode during the very first part of the AP. During the notch, the high Ca^{2+} level of the dyad forces the NCX to work in forward mode. During the plateau phase, it turns to reverse mode again, and during relaxation, it returns to the forward mode. This is corresponds to early findings by Peskoff et al. [26], who also show that NCXs in the dyad promotes the forward mode of NCX. Even though the Ca^{2+} release is controlled locally, Sher et al. [27] use a common pool model to control the local NCX current. With this model choice, the NCX will not sense a real local $\left[Ca^{2+}\right]$, but rather a mean local $\left[Ca^{2+}\right]$ for all dyads in the cell. The NCX is non-linearly dependent on the $\left[Ca^{2+}\right]$ so this might not be a valid assumption. They also model the effect of an elevated local $\left[Na^{+}\right]$ in the dyad. They apply a constant elevated $\left[Na^{+}\right]$ of 30 mM during the first 5 ms and 20 mM during the first 40 ms of the AP. They show that the first elevation has large effect on the strength of the initial reverse mode NCX phase. The longer and more modest elevation does not effect the early reverse mode, but rather modifies the forward mode during the notch of the AP. In Paper III, we tried to elevate the Na^{+} concentration in the dyad to levels where it could have impact on the reverse mode NCX. However, we where not able to raise the mean $\left[Na^{+}\right]$ in the dyad to such high levels, as 30 mM. We could raise the local $\left[Na^{+}\right]$ to such levels but not for the whole cleft.

3 Summary of the papers

The work I have done in this thesis is collected in the three papers that I will briefly present in the following. The first paper is a methodological paper that compares a discrete and stochastic model of diffusion with a continuous and deterministic model of diffusion. As mentioned in the review above, this study relates to an ongoing issue about discrete versus continuous modelling of diffusion in small intracellular domains. In the second paper I present a model of the Ca^{2+} dynamics in the dyadic cleft. Following the results from the first paper, I model the $\left[Ca^{2+}\right]$ as a continuous field, and the channel dynamics with discrete and stochastic Markov models. Simplistic but runnable code that discretise and solve the problem is presented, together with a software, `diffsim`, that can be used to solve more complex models. In the third paper we have used `diffsim` to create a complex model of the dyadic cleft. The model is used to study potential causes of the delayed and dyssynchronous Ca^{2+} release during heart failure. We also study the effect of local Na^{+} gradients on the reverse mode NCX.

Paper I:
Stochastic binding of Ca^{2+} ions in the dyadic cleft; continuous versus random walk description of diffusion

> *A continuous approach to spatially resolved biochemical systems based on reaction-diffusion PDEs provides a deterministic description in terms of average species concentration. This description is accurate and effective so long as the number of molecules in a system is macroscopically large.*
> Slepchenko et al. [52]

> *Continuous systems make sense when dealing with a very large number of particles for all reactive species, or when considering average population behavior.*
> Lemerle et al. [53]

> *The number of signaling molecules in these microdomains is small enough to render the notion of continuous concentration changes invalid*
> Koh et al. [35]

The Ca^{2+} dynamics of the dyadic cleft is fundamentally stochastic. The channels regulating the CICR open and close stochastically and the small volume of the dyad makes the number of participating Ca^{2+} ions a highly variable quantity. Most of the time during diastole, there are no Ca^{2+} ions in the cleft. During systole, the variation of the number of Ca^{2+} ions is of the same magnitude as the averaged number. As mentioned in the model review above, this has been addressed in two recent studies of the Ca^{2+} dynamics of the dyadic cleft [22, 35]. However, the number of Ca^{2+} ions in the cleft varies at a much smaller time scale than the number of Ca^{2+} ions binding to receptors in the cleft. We therefore hypothesize that a continuous description of Ca^{2+} diffusion can be used together with a stochastic, and discrete representation of the event of single Ca^{2+} ions binding to receptors in the cleft. In paper I, we investigate the difference between a continuous model of diffusion and a discrete, and stochastic model. The comparison is performed with respect to stochastic bindings of single Ca^{2+} ions in the dyadic cleft.

We developed our own Random walk simulator implemented in `MatLab` (The MathWorks, Natick, MA). The positions of the included ions are updated at each time step, using a standard Random walk algorithm [37, 54]. For the reaction process, we developed our own bi-molecular binding algorithm. The algorithm is analytical and depends on the diffusion constant, the time step, and the distance between the two molecules. The time step and diffusion constant is known *a priori*. Therefore the binding probabilities could be precomputed with respect to the distance. We use the bi-molecular binding algorithm to calculate the binding probabilities between diffusing particles too.

The comparison tests were done by collecting single binding events from 4 tentative RyRs, distributed at even distances from the center to the rim of the dyad. We did this

for three different type of simulations, *i*) steady state $\left[Ca^{2+}\right]$ from one open LCC, *ii*) steady state $\left[Ca^{2+}\right]$ during diastole (where there are on average 0.02 ions in the cleft), and *iii*) transient $\left[Ca^{2+}\right]$, the response from three LCCs that switched between open and closed states. We did the same type of simulations using a continuous model of the concentration in the cleft, but without collecting binding events, just recording the $\left[Ca^{2+}\right]$ response. This response was used to test whether the collected binding events from the Random walk model could have been collected using the continuous model. We did this by evaluating the continuous model goodness-of-fit. With the parameters we used, we could not discriminate between the two models.

During our work with this paper, the study of Tanskanen et al. [22] was published. As previously discussed, they registered a difference between the macroscopic quantity of gain in their model, while scaling the strength of the fluxes into the dyad together with the diffusion constants. In a continuous model, this would not change the gain, however they did indeed register a change in gain. This change can be tracked down to the fundamental difference in the registering of single bind events. We also scaled our model correspondingly and found that we could reproduce their reported difference, when we scaled the Ca^{2+} influx and the diffusion constant. However we also needed to reduce the spatial length scale of the Random walk model. This length scale is defined by:

$$\sigma = \sqrt{2D\Delta t}, \tag{1}$$

where D is the diffusion constant and Δt is the time step of the simulation. This length scale is the averaged distance an ion moves each time step in each of the spatial directions. This gave us a Random walk model that behaved differently with respect to the binding process, when both D and σ is changed. We also found a third parameter that could be tuned to get this different behaviour, namely the binding rate of the receptor, k^+. Previously in the study we have used a dimensionless version of the binding rate, k^{+*}, in a validation study of the Random walk model. The dimensionless binding rate is expressed by:

$$k^{+*} = k^+ / \left(4\pi D\sigma N a\right) \tag{2}$$

where k^+ is the binding rate of the receptor and Na Avogadro's number. This one parameter can be used to find what combinations of the three parameters that will cause the different behaviour of the two models. We found that if $k^{+*} < 0.013$, it was not possible to register any difference between the two models.

The rate k^{+*}, gives us the time scale of diffusion divided by the time scale of binding, for an ion close to a receptor. When k^{+*} is small, the diffusional process is dominant and a close ion will then mostly move away from the receptor. Interestingly, the closeness of an ion is dependent on the discretization parameter σ of the Random walk process. If k^{+*} was only dependent on model parameters, it would have made the decision of what method to use more straight forward. However, it makes sense that it is dependent on a discretization parameter if one consider the binding of an ion as a first passage process. It is well known that we need to adjust escape rates for absorbing boundaries in Random walk processes [55]. We do not adjust the escape rate in our Random walk model and hence the difference. This is illustrated by our numerical experiments when we do not remove a bound ion from the solution, see Fig. 12 **C**. Here, we see that the

binding rate predicted by the continuous model is within the 95 % confidence interval of the discrete model. This logic implies that one hypothetically could make σ as small as one would like, hence forcing a difference between the two models. However it does not make any sense to reduce it to a size smaller than the physical size of the ion or water molecule.

With this study we moderate the strong opinions (see the quotes in the beginning of this presentation), about the use of a continuous model of diffusion, when a small number of particles are involved. We assume that the discreteness of a dyad is not determined by how many ions there are in a cleft, or their exact position, but rather whether they are bound to discrete receptors or not. With this assumption, we show that if the diffusional process is fast compared to the reaction process one can use a continuous model of diffusion.

Paper II: A coupled stochastic and deterministic model of Ca^{2+} dynamics in the dyadic cleft

In the first paper, we found that one can capture the stochasticity of a dyad using a continuous description of the diffusional process. This statement is true as long as the diffusional process is fast compared to the reactional process. In paper II, I develop a more complex model of a single dyad than the one used in the first study. A continuous description of the diffusional process is used, which is describe with an advection-diffusion partial differential equation (PDE). The advection term comes from the electric field from the sarcolemma in the model. Channel dynamics are described using discrete and stochastic Markov chain models. Runnable `Python` code, which discretise and solves the PDE is provided. The system is discretized using a finite element method implemented using `PyDOLFIN` (`www.fenics.org/dolfin`). A time stepping scheme that can be used to couple the discrete and continuous models is also presented. Last in this paper, I introduce a software, `diffsim`, which lets a modeler use a high level declarative language to define coupled systems of continuous and discrete variables. More specifically, `diffsim` lets a user define arbitrary diffusional domains with several different diffusive ligands, and couple these with discrete stochastic Markov models. `diffsim` uses `PyDOLFIN` together with `NumPy` to discretise and solve the diffusional problem, and `NumPy` to solve the stochastic problem, using a modified Gillespie method [56, 57].

The continuous problem is advection dominated close to the sarcolemma, where the electric field is strongest. Ordinary finite element techniques fails to discretise such problems properly: the solution can oscillate or fail to converge [58]. I adopt an upwind technique to stabilize the linear system. This technique emphasize upwind contributions in the spatial discretization of the problem, with the result of stabilizing the system. When analyzed, such techniques can be viewed as introducing an upwind

artificial diffusion. The streamline-upwind/Petrov-Galerkin method is used to stabilize our problem [58]. This method adds the upwind diffusion as a discontinuous contribution to the testfunction in the streamline direction.

The system is stabilized using the SUPG method. However, the electric field creates a steep gradient in the Ca^{2+} concentration close to the sarcolemma. To be able to resolve the solution properly, higher resolution of the mesh in this area is needed. Unfortunately this creates quite large mesh, and quality has to be compromised to obtain solvability. The quality of the numerical solutions from three different meshes, are investigated in paper II. The meshes are created with a finer resolution at the point where the field is the strongest, but each with a different grade of refinement. Numerical solutions are computed and compared to an analytical solution, by computing the error measured in an L^2-norm. For each mesh, an optimal stabilization parameter τ, is found. The optimal τ for each mesh, is defined as the one that minimize the error. Not surprisingly, the mesh with the finest resolution gives the smallest error.

The solution of our test problem can qualitatively be divided into two different regions. A small part close to the TT, where the electric field is strongest, and a larger region where the electric field is diminutive. The solution has a steep spatial gradient in the first region, and it is more or less constant in the second one. Given a certain value of the stabilization parameter τ, the method cannot resolve both of these regions correctly. This results in either a good approximation of the Ca^{2+} concentration at the TT or at the SR. This observation is interesting, because it is at these two points the Ca^{2+} field interacts with stochastic boundaries, and sarcolemmal buffers. This introduces an uncertainty with respect to any parameters used to model these interactions, an uncertainty a modeler needs to be aware of.

I am not aware of any studies that solves the advection-diffusion equation in 3 dimensions for the dyadic cleft. Neither am I aware of any studies that couples the continuous Ca^{2+} field with stochastic and discrete Markov models for the dyadic cleft. With this paper I have described a method using publicly available tools: `PyDOLFIN` together with `diffsim` (`www.fenics.org/apps`), that does this. The computational effort of the model is unfortunately quite large. This is because the method requires high mesh resolution close to the TT.

In this paper summary, I think it is natural to emphasize the use of `Python` in scientific computing. In the first paper I used `MatLab`, as this was the language I was acquainted with, when I started my PhD. `MatLab` is also a natural choice for many scientific programmers. However `Python` is a programming language that is emerging as a natural choice in the scientific computing community. Together with `NumPy` (`numpy.scipy.org`), and `SciPy` (`www.scipy.org`), `Python` provides a high level programming language with similar abilities as `MatLab`. With `MatPlotLib` (`matplotlib.sourceforge.net`) we get a plotting program for 2D plots, which is able to produce figures with printing quality. High performance computing libraries such as `PETSc` (`www.mcs.anl.gov/petsc`) and `Trilinos` (`trilinos.sandia.gov`) are also accessible through the `Python` interface. In this thesis I have used `PyDOLFIN`, the python interface to `DOLFIN`, for Paper II and III. `DOLFIN` is an acronym for Dynamic Object-oriented Library for FINite element computation, and is a part of the software packages provided by the `FEniCS` project (`www.fenics.org`).

Paper III: Mechanisms underlying delayed and dyssynchronous Ca^{2+} release in failing cardiomyocytes examined by computer modeling

In our third paper we use `diffsim`, the software presented in paper II, to create a complex computational model of the Ca^{2+} dynamics in the dyadic cleft. We use the computational model to investigate possible contributions to the delayed and dyssynchronous Ca^{2+} release of a cardiomyocyte during HF. The model is also used to investigate if a single NCX, working in reverse mode, can trigger Ca^{2+} release when it is co-localized with a Na^+ channel (NaC) in the dyad.

In many of the integrative models reviewed above, a crucial assumption about the $\left[Ca^{2+}\right]$ in the dyadic cleft is made: it is homogeneous inside a single dyad. All local ion gradients in the dyad is ignored, and the LCCs and RyRs in a single dyad sense the same $\left[Ca^{2+}\right]$. The assumption is made so the computational cost of the integrative models can be reduced. However, we think that important aspects of the ion dynamics of the dyadic cleft may be is lost. Previously it has been shown that large local ion gradients are created in the dyad when ion channels are open [21]. Local receptors sense these gradients and act accordingly. In Paper III we exploits the local gradients created in the dyad in both our two studies. In the first study we show that the sharp Ca^{2+} gradient, created from an open LCC, can be used to reduce the computational cost of a large dyad. In the second study we co-localize an NCX with an open NaC. Here we see how the local Na^+ gradient influence the reverse mode of the NCX.

In the first study we investigate the timing of the Ca^{2+} release of a dyad and two possible contributions to delayed and dyssynchronous release during HF. In this study we assume that the release is triggered only by Ca^{2+} from the LCCs. The timing of Ca^{2+} release is then determined by the kinetics of the LCC and the RyR, the strength of the $\left[Ca^{2+}\right]$ response from a single LCC, and the number of LCCs and RyRs in the dyad. A recent study claims that there are many, between 20-40 LCCs in a single dyad [12]. We chose 20 LCC in our dyad. The number of RyRs follows from this number, as five RyRs for each LCC [22, 59], which give us a dyad with 100 RyRs. We used a published Markov model scheme for the LCC [32], and adjust the rates so the model fit the experimental data provided by Poláková et al. [12]. The electrical field from the sarcolemma is included as presented in Paper II, and the amplitude of an LCC is also fitted to published values. The size of the dyad follows from the number of the included RyRs. This is because the RyRs are aligned in a regular 2D lattice grid [60], see Fig. 1**B** in paper III. A cylindrical dyad with 100 RyRs, must have radius of ~ 200 nm. With this size of the domain we are unfortunately not able to resolve the transient $\left[Ca^{2+}\right]$. Instead we use a quasi steady state solution, as an approximation of the Ca^{2+} response for an open LCC.

We apply two different APs to drive the model. One AP comes from a healthy cardiomyocyte and the other one comes from a failing cardiomyocyte. A simplistic model of the RyR kinetics is used. The activation rate of this model is fitted so the Ca^{2+} release time of the first RyR, using the healthy AP, fits experimental results provided in the study. We show that changes in AP shape can delay the time to release and increase

dyssynchrony. This is because the HF AP reduces the driving force to the Ca^{2+} current from an open LCC. HF alters the structure of the dyad. We investigate how potential changes in the the geometry of a dyad, here modeled as an increase of the cleft height, contributes to the delayed and dyssynchronous release of a dyad. We find that small increase in the height of the dyad, can cause delayed and dyssynchronous release.

High level of cytosolic $\left[Na^{+}\right]$ will contribute to the Ca^{2+} influx during reverse mode of an NCX. In the second study of this paper, we use our model to see if a strong local Na^{+} gradient from an open NaC, could be utilized by a co-localized NCX, to trigger Ca^{2+} release. In a previous study we have shown that this is the case [25]. In this study we used a scaled version of the whole cell current for the local NaC. In our model we represent a single current as being either on or off. We hypothesised that modelling the current from the NaC in this way, we would get a larger local Na^{+} current and hence larger reverse mode NCX current. Somewhat surprisingly we got the opposite result. We measured the Na^{+} and Ca^{2+} response at the mouth of the NCX, while applying a voltage ramp, from -50 to 50 mV. We see that during the hyperpolarized membrane potentials we get a strong $\left[Na^{+}\right]$ response. At these potentials are the NCX current held at a low level. During the depolarized membrane potentials we see a stronger reverse mode NCX, but the $\left[Na^{+}\right]$ response from the open NaC is small at these membrane potentials. These results indicate that Ca^{2+} influx from a single NCX working in reverse mode, cannot trigger CICR alone. We also control a side effects of a key model assumption in the study of Lines et al. [25]. Here they model the crowdedness of a dyad by lowering the diffusion coefficient of Na^{+} dramatically. In this way they managed to hold onto a high $\left[Na^{+}\right]$ close to an NCX. The diffusion constant of Na^{+} is believed to be half that of the diffusion constant of Ca^{2+} [28]. We use a varying Ca^{2+} diffusion constant and registered the potential response in the dyad for an open RyR. We show that a low Ca^{2+} diffusion constants will cause un-physiological high $\left[Ca^{2+}\right]$ in the cleft.

With this study we have quantified possible contributions to the delayed and dyssynchronous release observed during HF [17], using a detailed computational model of the dyadic cleft. We have also used the model to study possible effects of local Na^{+} gradients to the reverse mode NCX. In both of the studies in Paper III, we utilised the local ion gradients established in the cleft after an open ion channel.

4 Future work

It is my belief that the results presented in this thesis may shed light on some important aspects of the computational modeling of the Ca^{2+} dynamics in the dyadic cleft. However, there is a number of issues I would like to investigate further.

The choice of what model to use to represent the $\left[Ca^{2+}\right]$ in the dyadic cleft has to be based on quantitative measures rather than qualitative measures. In our first study, we show that the discreteness of a dyad can be captured by a model using continuous representation of the $\left[Ca^{2+}\right]$ and stochastic and discrete representation of the binding of single Ca^{2+} ions to receptors. This assumption holds for the parameter regime we have chosen in our study. However we show that with different discretization parameters for the Random walk process, we can force a difference. In this introduction we hypothesise

that this is because the first passage process is modelled more correctly using a smaller discretization parameter. This is illustrated by not removing a bound ion from the solution in the Random walk model. Then we get the same amount of bound ions using the two models. It would have been interesting to include a binding flux to the continuous model. In this way we model the removal of an ion from the solution. This might revert the differences between the two models for small σ. It would also be interesting to ask the modellers of the Tanskanen et al. [22] study, to reduce their discretization parameter from 1 nm to let say 0.5 nm, to see if this would alter their results.

In paper II, I use a finite element method together with a streamline-upwind/Petrov-Galerkin stabilizing method to discretise and solve an advection-diffusion PDE. Stabilizing methods are a large research field in the finite element method community, and other methods exists [61]. A family of finite element methods are discontinuous-Galerkin methods, which can be used to enforce the upwind contribution at the element interface level [62]. I successfully used discontinuous Galerkin methods on our test problem (result not shown), but unfortunately it introduce a number of extra degrees of freedom to the linear problem. A recent study combines the attractive low numbers of degrees of freedom from the continuous methods, with the upwinding abilities of the discontinuous method [63]. Labeur and Wells [63] claim that *for linear elements, only minor modifications are required to existing continuous finite element codes*, which sound very attractive. I also recognize that I can do a minor modification to our stabilizing parameters, τ_e. In this parameter, the local mesh size is included. We have just used the diameter of the sphere that circumscribes the local tetrahedron, as our local mesh size. Instead we could use the a length based on the size of the element in the direction of the field [64].

In the last paper, we use a detailed computational model to investigate the dyssynchronous and delayed release in failing cardiomyocytes. Our study limits to the activation time of the RyRs. A natural extension would be to also include the release flux from SR, hence including the spark generation. With this extension, it would make it easier to evaluate the model, and to create predictions that have further relevance for the experimental community. Such an extension would require a better model for the RyR. We would also need to resolve the Ca^{2+} gradients from the open RyRs. It might be possible to use a similar method as we did for the LCC flux, that is to say a quasi steady state approach. We could for example record the steady state Ca^{2+} response from an open RyR. This response is dependent on the $\left[Ca^{2+}\right]$ in jSR, which would then be the dependent variable for the recorded Ca^{2+} response. The response can then be applied to the neighbouring RyR, triggering further release. We should be able to evaluate how well this quasi-steady state approach is, by making numerical experiments on a reduced system.

By assuming a quasi steady state Ca^{2+} response we over-estimates the $\left[Ca^{2+}\right]$ at the included RyRs, as the transient raise to the steady state value is not included. We show that the error is not big as the steady state is established fast. However, we have not included the sarcolemmal buffers in our model. This would prolong the time to steady state and make our quasi steady state approximation worse. It would be natural to quantify the error made with the quasi steady state approach, with and without

sarcolemmal buffers.

It would also be interesting to try to reduce our model so it could be included in an integrative model of the whole cardiomyocyte. However we probably have to take another approach to reduce the computational effort, than the two studies presented above, that is to say Greenstein et al. [49] and Williams et al. [50]. Both of these studies assume that the $\left[Ca^{2+}\right]$ in the dyadic cleft is homogeneous. With this assumption all LCCs and RyRs in the dyad sense the same $\left[Ca^{2+}\right]$. This is clearly not true. We show that the gradients are important, as it is only the juxtapositional LCC that can trigger release from a RyR. We use this observation to reduce the computational effort of our model. This reduction might be taken further, reducing the whole dyad to a single discrete Markov model. Such reduction will need thorough mathematical analysis together with numerical experiments.

A strength of the finite element methods is that it let us solve the advection-diffusion equation on a unstructured mesh, capable of describing almost arbitrary geometry. Therefore it would be natural to extend our computational mesh with the current knowledge of the geometrical structure of the included channel proteins. Tanskanen et al. [22] do include this information in their model. They show that it does make a difference on the gain of their model, when the structure of the proteins is included. We should try using our quasi steady state approach for the $\left[Ca^{2+}\right]$, on such meshes too.

There are some uncertainties in the modeling of the possible contribution of Ca^{2+} release from the NCX, we would like to pursue. The actual NCX model we have used is from a whole cell model of rabbit [65]. The model is tuned for the whole cell intracellular environment of a rabbit. Our model is of a mouse, which has a higher resting $\left[Na^{+}\right]$. We are also utilizing local concentration gradients, which can be higher than the whole cell concentration. Hence it would be appropriate to tune the rates of the NCX model according to the intracellular environment of a mouse model and to the higher local ion gradients in the dyad.

Last but certainly not least, we anticipate a follow up study on the model for the electric field from the sarcolemma. The development of the model that defines the strength and the shape of the field comes mainly from two studies: Bers et al. [30] and Soeller and Cannell [21]. During the implementation of our model we found discrepancies between the two presentations and obvious errors. We were also not able to reproduce the field strength reported by Soeller and Cannell [21]. We had to tune the charge density parameter to get the same strength as they got. The importance of the electric field is not only for the study of numerical methods, but rather the effect it has on the local $\left[Ca^{2+}\right]$. A small change in the strength has large effect on the $\left[Ca^{2+}\right]$. The model also assume a monovalent 1-1 electrolyte which is clearly wrong. The negative charge in a cell comes mainly from negatively charged proteins. These does not have the same access to the dyadic cleft as the Cl^{-}. This might not have a large impact but our belief in the current model of the electric field is not strong.

Bibliography

1. Cowie, M. R., Mosterd, A., Wood, D. A., Deckers, J. W., Poole-Wilson, P. A., Sutton, G. C., and Grobbee, D. E. 1997. The epidemiology of heart failure. Eur. Heart J. 18:208–225.

2. Rosamond, W., Flegal, K., Furie, K., Go, A., Greenlund, K., Haase, N., Hailpern, S. M., Ho, M., Howard, V., Kissela, B., Kittner, S., Lloyd-Jones, D., McDermott, M., Meigs, J., Moy, C., Nichol, G., O'Donnell, C., Roger, V., Sorlie, P., Steinberger, J., Thom, T., Wilson, M., Hong, Y., Committee, A. H. A. S., and Subcommittee, S. S. 2008. Heart disease and stroke statistics–2008 update: a report from the american heart association statistics committee and stroke statistics subcommittee. Circulation 117:e25–146.

3. Bers, D. M. 2001. Excitation-Contraction Coupling and Cardiac Contractile Force Kluwert Academic, Dordrecht, The Netherlands 2nd edition.

4. Hasenfuss, G. and Pieske, B. 2002. Calcium cycling in congestive heart failure. J. Mol. Cell. Cardiol. 34:951–969.

5. Keener, J. and Sneyd, J. 1998. Mathematical Physiology Springer.

6. Fawcett, D. W. and McNutt, N. S. 1969. The ultrastructure of the cat myocardium. i. ventricular papillary muscle. J. Cell Biol. 42:1–45.

7. Franzini-Armstrong, C., Protasi, F., and Ramesh, V. 1999. Shape, size, and distribution of Ca^{2+} release units and couplons in skeletal and cardiac muscles. Biophys. J. 77:1528–1539.

8. Beuckelmann, D. J. and Wier, W. G. 1988. Mechanism of release of calcium from sarcoplasmic reticulum of guinea-pig cardiac cells. J. Physiol. 405:233–255.

9. Balke, C. W. and Wier, W. G. 1991. Ryanodine does not affect calcium current in guinea pig ventricular myocytes in which Ca^{2+} is buffered. Circ. Res. 68:897–902.

10. Fabiato, A. 1983. Calcium-induced release of calcium from the cardiac sarcoplasmic reticulum. Am. J. Physiol. 245:C1–14.

11. Stern, M. D. 1992. Theory of excitation-contraction coupling in cardiac muscle. Biophys. J. 63:497–517.

12. Poláková, E., Zahradníková, A., Pavelková, J., Zahradník, I., and Zahradníková, A. 2008. Local calcium release activation by dhpr calcium channel openings in rat cardiac myocytes. J Physiol 586:3839–3854.

13. Stern, M. D. and Cheng, H. 2004. Putting out the fire: what terminates calcium-induced calcium release in cardiac muscle? Cell Calcium 35:591–601.

14. Cheng, H. and Lederer, W. J. 2008. Calcium sparks. Physiol Rev 88:1491–1545.

15. Cheng, H., Lederer, W. J., and Cannell, M. B. 1993. Calcium sparks: elementary events underlying excitation-contraction coupling in heart muscle. Science 262:740–744.

16. Bers, D. M. 2006. Altered cardiac myocyte ca regulation in heart failure. Physiology (Bethesda) 21:380–387.

17. Louch, W. E., Mørk, H. K., Sexton, J., Strømme, T. A., Laake, P., Sjaastad, I., and Sejersted, O. M. 2006. T-tubule disorganization and reduced synchrony of Ca^{2+} release in murine cardiomyocytes following myocardial infarction. J. Physiol. 574:519–533.

18. McLaughlin, S. G., Szabo, G., and Eisenman, G. 1971. Divalent ions and the surface potential of charged phospholipid membranes. J. Gen. Physiol. 58:667–687.

19. Langner, M., Cafiso, D., Marcelja, S., and McLaughlin, S. 1990. Electrostatics of phosphoinositide bilayer membranes. theoretical and experimental results. Biophys. J. 57:335–349.

20. Post, J. A. and Langer, G. A. 1992. Sarcolemmal calcium binding sites in heart: I. molecular origin in "gas-dissected" sarcolemma. J. Membr. Biol. 129:49–57.

21. Soeller, C. and Cannell, M. B. 1997. Numerical simulation of local calcium movements during l-type calcium channel gating in the cardiac diad. Biophys. J. 73:97–111.

22. Tanskanen, A. J., Greenstein, J. L., Chen, A., Sun, S. X., and Winslow, R. L. 2007. Protein geometry and placement in the cardiac dyad influence macroscopic properties of calcium-induced calcium release. Biophys. J. 92:3379–3396.

23. Bers, D. M., Despa, S., and Bossuyt, J. 2006. Regulation of Ca^{2+} and Na^{+} in normal and failing cardiac myocytes. Ann. N. Y. Acad. Sci. 1080:165–177.

24. Litwin, S. E., Li, J., and Bridge, J. H. 1998. Na-ca exchange and the trigger for sarcoplasmic reticulum ca release: studies in adult rabbit ventricular myocytes. Biophys. J. 75:359–71.

25. Lines, G. T., Sande, J. B., Louch, W. E., Mørk, H. K., Grøttum, P., and Sejersted, O. M. 2006. Contribution of the Na^{+}/Ca^{2+} exchanger to rapid Ca^{2+} release in cardiomyocytes. Biophys. J. 91:779–792.

26. Peskoff, A., Post, J. A., and Langer, G. A. 1992. Sarcolemmal calcium binding sites in heart: II. mathematical model for diffusion of calcium released from the sarcoplasmic reticulum into the diadic region. J. Membr. Biol. 129:59–69.

27. Sher, A. A., Noble, P. J., Hinch, R., Gavaghan, D. J., and Noble, D. 2008. The role of the Na^{+}/Ca^{2+} exchangers in Ca^{2+} dynamics in ventricular myocytes. Prog Biophys Mol Biol 96:377–398.

28. Langer, G. A. and Peskoff, A. 1996. Calcium concentration and movement in the diadic cleft space of the cardiac ventricular cell. Biophys. J. 70:1169–1182.

29. Cannell, M. B. and Soeller, C. 1997. Numerical analysis of ryanodine receptor activation by l-type channel activity in the cardiac muscle diad. Biophys. J. 73:112–22.

30. Bers, D. M., Philipson, K. D., and Peskoff, A. 1985. Calcium at the surface of cardiac plasma membrane vesicles: cation binding, surface charge screening, and Na-Ca exchange. J. Membr. Biol. 85:251–261.

31. Rice, J. J., Jafri, M. S., and Winslow, R. L. 1999. Modeling gain and gradedness of Ca^{2+} release in the functional unit of the cardiac diadic space. Biophys. J. 77:1871–1884.

32. Jafri, M. S., Rice, J. J., and Winslow, R. L. 1998. Cardiac Ca^{2+} dynamics: the roles of ryanodine receptor adaptation and sarcoplasmic reticulum load. Biophys. J. 74:1149–68.

33. Keizer, J. and Smith, G. D. 1998. Spark-to-wave transition: saltatory transmission of calcium waves in cardiac myocytes. Biophys. Chem. 72:87–100.

34. Keizer, J. and Levine, L. 1996. Ryanodine receptor adaptation and Ca^{2+}(-)induced Ca^{2+} release-dependent Ca^{2+} oscillations. Biophys. J. 71:3477–3487.

35. Koh, X., Srinivasan, B., Ching, H. S., and Levchenko, A. 2006. A 3D Monte Carlo analysis of the role of dyadic space geometry in spark generation. Biophys. J. 90:1999–2014.

36. Stiles, J. R., Helden, D. V., Bartol, T. M., Salpeter, E. E., and Salpeter, M. M. 1996. Miniature endplate current rise times less than 100 microseconds from improved dual recordings can be modeled with passive acetylcholine diffusion from a synaptic vesicle. Proc. Natl. Acad. Sci. U. S. A. 93:5747–5752.

37. Stiles, J. R. and Bartol, T. M. 2001. Monte carlo methods for simulating realistic synaptic microphysiology using mcell in E. D. Schutter, editor, Computational Neuroscience: Realistic Modeling for Experimentalists pages 87–127 CRC Press.

38. Saftenku, E., Williams, A. J., and Sitsapesan, R. 2001. Markovian models of low and high activity levels of cardiac ryanodine receptors. Biophys. J. 80:2727–2741.

39. Wang, M.-C., Collins, R. F., Ford, R. C., Berrow, N. S., Dolphin, A. C., and Kitmitto, A. 2004. The three-dimensional structure of the cardiac l-type voltage-gated calcium channel: comparison with the skeletal muscle form reveals a common architectural motif. J. Biol. Chem. 279:7159–7168.

40. Liu, Z., Zhang, J., Li, P., Chen, S. R. W., and Wagenknecht, T. 2002. Three-dimensional reconstruction of the recombinant type 2 ryanodine receptor and localization of its divergent region 1. J. Biol. Chem. 277:46712–46719.

41. Wang, H., Peskin, C. S., and Elston, T. C. 2003. A robust numerical algorithm for studying biomolecular transport processes. J. Theor. Biol. 221:491–511.

42. Stern, M. D., Song, L. S., Cheng, H., Sham, J. S., Yang, H. T., Boheler, K. R., and Ríos, E. 1999. Local control models of cardiac excitation-contraction coupling. a possible role for allosteric interactions between ryanodine receptors. J. Gen. Physiol. 113:469–489.

43. Zahradníková, A. and Zahradník, I. 1996. A minimal gating model for the cardiac calcium release channel. Biophys. J. 71:2996–3012.

44. Zahradník, I., Györke, S., and Zahradníková, A. 2005. Calcium activation of ryanodine receptor channels–reconciling RyR gating models with tetrameric channel structure. J. Gen. Physiol. 126:515–527.

45. Zahradníková, A., Poláková, E., Zahradník, I., and Zahradníková, A. 2007. Kinetics of calcium spikes in rat cardiac myocytes. J. Physiol. 578:677–691.

46. Greenstein, J. L. and Winslow, R. L. 2002. An integrative model of the cardiac ventricular myocyte incorporating local control of Ca^{2+} release. Biophys. J. 83:2918–2945.

47. Hinch, R., Greenstein, J. L., Tanskanen, A. J., Xu, L., and Winslow, R. L. 2004. A simplified local control model of calcium-induced calcium release in cardiac ventricular myocytes. Biophys. J. 87:3723–3736.

48. Hinch, R. 2004. A mathematical analysis of the generation and termination of calcium sparks. Biophys. J. 86:1293–1307.

49. Greenstein, J. L., Hinch, R., and Winslow, R. L. 2006. Mechanisms of excitation-contraction coupling in an integrative model of the cardiac ventricular myocyte. Biophys. J. 90:77–91.

50. Williams, G. S. B., Huertas, M. A., Sobie, E. A., Jafri, M. S., and Smith, G. D. 2007. A probability density approach to modeling local control of calcium-induced calcium release in cardiac myocytes. Biophys. J. 92:2311–2328.

51. Huertas, M. A. and Smith, G. D. 2007. The dynamics of luminal depletion and the stochastic gating of Ca^{2+}-activated Ca^{2+} channels and release sites. J. Theor. Biol. 246:332–354.

52. Slepchenko, B. M., Schaff, J. C., Carson, J. H., and Loew, L. M. 2002. Computational cell biology: spatiotemporal simulation of cellular events. Annu. Rev. Biophys. Biomol. Struct. 31:423–441.

53. Lemerle, C., Ventura, B. D., and Serrano, L. 2005. Space as the final frontier in stochastic simulations of biological systems. FEBS Lett. 579:1789–1794.

54. Berg, H. C. 1993. Random Walks in Biologywell Princeton University Press, 41 William street, Princeton, New Jersey 08540 expanded edition 164 pages.

55. Redner, S. 2001. A Guide to First-Passage Processes Cambridge University Press.

56. Gillespie, D. T. 1977. Exact stochastic simulation of coupled chemical reactions J. Phys. Chem. 81:2340–2361.

57. Rüdiger, S., Shuai, J. W., Huisinga, W., Nagaiah, C., Warnecke, G., Parker, I., and Falcke, M. 2007. Hybrid stochastic and deterministic simulations of calcium blips. Biophys. J. 93:1847–1857.

58. Brooks, A. N. and Hughes, T. J. R. 1982. Streamline upwind/petrov-galerkin formulations for convection dominated flows with particular emphasis on the incompressible navier-stokes equations Computer Methods in Applied Mechanics and Engineering 32:199–259.

59. Bers, D. M. and Stiffel, V. M. 1993. Ratio of ryanodine to dihydropyridine receptors in cardiac and skeletal muscle and implications for e-c coupling. Am J Physiol 264:C1587–C1593.

60. Wagenknecht, T., Radermacher, M., Grassucci, R., Berkowitz, J., Xin, H. B., and Fleischer, S. 1997. Locations of calmodulin and fk506-binding protein on the three-dimensional architecture of the skeletal muscle ryanodine receptor. J. Biol. Chem. 272:32463–32471.

61. Codina, R. 1998. Comparison of some finite element methods for solving the diffusion-convection-reaction equation Computer Methods in Applied Mechanics and Engineering 156:185–210.

62. Arnold, D. N., Brezzi, F., Cockburn, B., and Marini, L. D. 2002. Unified Analysis of Discontinuous Galerkin Methods for Elliptic Problems SIAM J. Numer. Anal. 39:1749–1779.

63. Labeur, R. J. and Wells, G. N. 2007. A galerkin interface stabilisation method for the advection-diffusion and incompressible navier-stokes equations Computer Methods in Applied Mechanics and Engineering 196:4985–5000.

64. Tezduyar, T. and Park, Y. 1986. Discontinuity-capturing finite element formulations for nonlinear convection-diffusion-reaction equations. Comp. Methods Appl. Mech. Eng. 59:307–325.

65. Shannon, T. R., Wang, F., Puglisi, J., Weber, C., and Bers, D. M. 2004. A mathematical treatment of integrated ca dynamics within the ventricular myocyte. Biophys. J. 87:3351–3371.

Paper I:
Stochastic binding of Ca^{2+} ions in the dyadic cleft; continuous versus random walk description of diffusion

Stochastic binding of Ca^{2+} ions in the dyadic cleft; continuous versus random walk description of diffusion

J. Hake[1], **G. T. Lines**[1,2]

[1] Center for Biomedical Computing, Simula Research Laboratory,
P. O. Box 134, N-1325 Lysaker, Norway

[2] Department of Informatics, University of Oslo,
P. O. Box 1080 Blindern, N-0316 Oslo, Norway

Abstract:

Ca^{2+} signalling in the dyadic cleft in ventricular myocytes is fundamentally discrete and stochastic. We study the stochastic binding of single Ca^{2+} ions to receptors in the cleft using two different models of diffusion: a stochastic and discrete Random Walk (RW) model, and a deterministic continuous model. We investigate whether the latter model, together with a stochastic receptor model, can reproduce binding events registered in fully stochastic RW simulations. By evaluating the continuous model goodness-of-fit, for a large range of parameters, we present evidence that it can. Further, we show that the large fluctuations in binding rate observed at the level of single time steps are integrated and smoothed at the larger time scale of binding events, which explains the continuous model goodness-of-fit. With these results we demonstrate that the stochasticity and discreteness of the Ca^{2+} signalling in the dyadic cleft, determined by single binding events, can be described using a deterministic model of Ca^{2+} diffusion together with a stochastic model of the binding events, for a specific range of physiological relevant parameters. Time-consuming RW simulations can thus be avoided. We also present a new analytical model of bi-molecular binding probabilities, which we use in the RW simulations and the statistical analysis.

1 Introduction

It is an important and contentious issue whether diffusion in signalling micro domains can be modelled deterministically and continuously, or if stochastic and discrete Random Walk (RW) methods should be employed [1–6]. Signalling micro domains are used by the cell to convey information and it is important to use accurate and reliable simulation methods when these processes are studied. Traditionally, they have been studied using Fick's second law of diffusion together with macroscopic rate laws, where the latter are used to model chemical reactions. These laws provide a deterministic prediction of the changes of the average number of molecules in a process over time. The solutions are continuous functions of both space and time. Reaction diffusion processes in macroscopic environments, where fluctuations from the predicted average number of particles in a solution are small, are modelled successfully by these laws. The laws were originally empirical but they are also well-founded in statistical physics [7]. In recent years, as smaller and smaller sub-cellular domains have been studied, researchers have focused on the discreteness and stochasticity of the physiological processes. This has raised issues for the deterministic models [4, 8]. In sub-cellular micro domains, the number of involved molecules is small and the fluctuations from the predicted average number of molecules involved become dominant. Three dimensional (3D) RW simulators have been developed to incorporate the discreteness and stochasticity of the signalling in intracellular micro domains. One well-established simulator is MCell [9, 10], which has been used in some recent studies of sub-cellular signalling. The results of these studies illustrate clearly the fundamental discreteness and stochasticity of the studied processes [1, 11, 12]. Another approach to modelling the discreteness and stochasticity of a sub-cellular process is to model the diffusion and possible buffer dynamic with a deterministic and continuous model together with a stochastic model of receptors that switch states randomly according to the concentration at the receptor site, i.e., modelling the binding of single molecules to a receptor stochastically. Different versions of this method have recently been used to study the functionality of the well-studied signalling micro domain of the dyadic cleft, in ventricular myocytes [13–15], and also in a whole cell study of the Ca^{2+} dynamics in the endoplasmic reticulum [16]. Although this method is already in use, the fundamental problem of using a continuous and deterministic representation of a small number of diffusing molecules has not been addressed. This issue is of great concern when signalling in the dyadic cleft is studied, because the volume of this domain is in the magnitude of atto litres. This concern is illustrated by the fact that during diastole, when the myocyte is relaxing, the cytosolic $\left[Ca^{2+}\right]$ is as low as 0.1 μM, leaving, on average, 0.02 Ca^{2+} ions present in the cleft. Hereafter, we will relate to this model, i.e., the continuous and deterministic description of Ca^{2+} diffusion together with a stochastic and discrete description of single receptors, as "the continuous model".

The dyadic cleft is a signalling micro domain in which the Ca^{2+} induced Ca^{2+} release mechanism is controlled tightly [17, 18]. A travelling action potential triggers the influx of external Ca^{2+} through the L-type Ca^{2+} channels (LCCs). From the mouth of a LCC, which are located at the membrane of a T-tubule (TT), Ca^{2+} diffuses into the cleft. The cleft is narrow, about 15 nm wide [19, 20], and a unitary LCC current creates a

very high Ca^{2+} concentration in the cleft, $\simeq 10 - 200\mu$M [21], compared to the value at rest , $\simeq 0.1\mu$M. This Ca^{2+} signal triggers both the inactivation of the LCC current and further Ca^{2+} release from the opposing Ryanodin receptors (RyRs) [22, 23], which are attached to the sarcoplasmic reticulum (SR), an intracellular Ca^{2+} store. What causes the reliable termination of Ca^{2+} release from the RyR is still a debated issue [24]. However, among the proposed explanatory hypotheses, inactivation due to binding of single Ca^{2+} ions to receptors in the dyadic cleft, is well-established [25, 26]. For a recent review of the Ca^{2+} dynamics in the cleft, see Bers and Guo [27], and the references therein.

For a long time, continuous and deterministic models have been used to study Ca^{2+} dynamics in the dyadic cleft [21, 28–31], and its role in the release of Ca^{2+}. Two recent studies of Ca^{2+} dynamics use a discrete RW model to describe the Ca^{2+} diffusion in the cleft [12, 32]. Koh et al. [12] uses MCell and argues that few Ca^{2+} ions in a small volume cannot properly be simulated with a continuous model of diffusion. However, they do not present any results that support this claim. Tanskanen et al. [32] present an impressive study that includes physiological details on a micro-scale level, such as the electrostatic force from the sarcolemmar and the geometrical structures of the large membrane proteins in the cleft, while integrating the Ca^{2+} release from many clefts, and thus obtaining a measure of the Ca^{2+} release from the whole cell. In contrast to Koh et al. [12], they explicitly address the difference between their model and an equivalent model that uses a deterministic description of Ca^{2+} diffusion. They do this by measuring the effect on the excitation-contraction coupling (ECC) gain when they vary the diffusion constant of Ca^{2+}, together with the parameters that determine the influx of Ca^{2+} ions to the cleft. They show that the ECC gain varies with the parameters [see Fig. 12 in 32]. This result points to a "subtle but potentially significant difference in predicted macroscopic behaviour arising from the underlying stochastic simulation of Ca^{2+} motion in the dyad." The rationale for this statement is that if they had changed the same parameters in an equivalent model using a deterministic description of Ca^{2+} diffusion, they would not have registered any differences in ECC gain because the receptors situated in the cleft would have experienced the same level of Ca^{2+} concentration. In our study we examine the discrete events in the cleft that are actually modelled differently in a continuous vs a RW model of diffusion in the dyadic cleft; namely, the binding of single Ca^{2+} ions to single receptors. By doing this, we strip the model of Ca^{2+} dynamics in the dyadic cleft of many important physiological details that affect the generation and termination of a spark [12, 21, 32], but the comparison between the actual differences between the two diffusion models become clearer.

We also present what is, to our knowledge, a novel model of bi-molecular binding probabilities between single diffusive ligands and single stationary or mobile receptors that are used in our RW simulator. The model is analytical. It depends only on the diffusion constant of the ligand, the macroscopic binding rate, the time step of the RW algorithm, and the distance between the two molecules at the beginning of the time step. The first three parameters are all known before a simulation starts and the binding probabilities are precomputed with respect to distance for the reactions that are included in the simulation. During a simulation, look-up tables are used. The error introduced by the model is studied thoroughly for a large set of parameters. We find

that for a given time step, the error introduced by the bi-molecular interaction model is much smaller than the error introduced by the RW simulation, due to an absorbing boundary in our model. Hence, we can use larger time steps for the time-consuming reaction process.

The results of the statistical goodness-of-fit tests reveal that the continuous model, for a specific parameter range, can reproduce the registered binding events from the RW simulations. This is somewhat unexpected, because the binding probability in the continuous model is linear with respect to the $\left[Ca^{2+}\right]$ at a single receptor and is also constant during steady-state simulations. This is in contrast to the binding probabilities in the RW model, which depend directly on the distance between a RyR and any nearby Ca^{2+} ions. We find that the large variations in binding rates at the time scale of a single time step, $\simeq 1.25 \times 10^{-4}$ ms, are integrated and smoothed at the time scale of binding events, $\simeq 0.5$ ms. These results refine the statements made in a number of recent studies [2, 6, 10, 12], which claim that when the number of participating particles in a volumes falls, a deterministic description of concentration is invalid or does not make sense, and fully stochastic methods have to be employed. Our study reveals that the extra discreteness and stochasticity that a full RW model introduce are integrated at the time scale of binding events, to the same value given by the continuous model. This also explain why the average description of the $\left[Ca^{2+}\right]$ in the cleft, given by the continuous model, is sufficient when the registration of single binding events is studied. The result is parameter-dependent. For small values of the diffusion constant, we find a difference between the two models similar to that which Tanskanen et al. [32] find. We further investigate the cause of this difference and the quantitative dependency of the parameters.

This paper is divided into five main sections. The introduction is followed by a theory section in which we describe the models and how we solve them. Also in the theory section, we derive and analyze the model of bi-molecular binding probabilities. In the next section, Methods, we explain how we performed our simulations and which statistical tests we used. The results of our simulations and tests are presented in the Results section and then discussed in the Discussion section.

2 Theory

2.1 Continuous model

Ca^{2+} diffusion in the continuous model is described by a well-known reaction-diffusion model, which consists of a set of coupled partial differential equations (PDEs) [33, 34]. Symmetry in the angular and z direction were assumed, thus reducing the full 3D model to a 1D model in the radial direction. If c, B_m and B_s denote, respectively, the concentration of Ca^{2+}, mobile buffer and stationary buffer, the full system is given by

$$\left.\begin{aligned} \frac{\partial c}{\partial t} &= D_c\nabla_r^2 c + R_m(c,B_m) + R_s(c,B_s), \\ \frac{\partial B_m}{\partial t} &= D_m\nabla_r^2 B_m + R_m(c,B_m), \end{aligned}\right\} \quad r\in(0,\mathrm{R})\subset\mathbb{R},\, t>0, \tag{1}$$

$$\frac{\partial B_s}{\partial t} = R_s(c,B_s), \qquad r\in[0,\mathrm{R})\subset\mathbb{R},\, t>0, \tag{2}$$

$$\tag{3}$$

The reaction terms are given by

$$\begin{aligned} R_m(c,B_m) &= -k_m^+ B_m\, c + k^-(B_m^T - B_m), \\ R_s(c,B_s) &= -k_s^+ B_s\, c + k^-(B_s^T - B_s), \end{aligned} \tag{4}$$

where B_m^T and B_s^T are the total concentration of the two buffer types. D_c and D_b are the diffusion constants of Ca^{2+} and the mobile buffer, respectively. ∇_r^2 is the radial diffusion operator

$$\nabla_r^2 = \frac{\partial^2}{\partial r^2} + \frac{1}{r}\frac{\partial}{\partial r}. \tag{5}$$

The initial conditions are given by

$$\left.\begin{aligned} c(r,0) &= 0, \\ B_m(r,0) &= B_m^T, \\ B_s(r,0) &= B_s^T, \end{aligned}\right\} \quad r\in[0,\mathrm{R}]\subset\mathbb{R}, t=0, \tag{6}$$

and the boundary conditions are given by

$$-D_c\frac{\partial c}{\partial r} = J_{in}, \qquad -D_m\frac{\partial B_m}{\partial r} = 0, \qquad r=0,\, t>0, \tag{7}$$

$$c(r,t) = C_c, \qquad B_m(r,t) = B_m^T, \qquad r=R,\, t>0, \tag{8}$$

where J_{in} is the LCC line source, C_c the Ca^{2+} concentration in cytosole, and R the radius of the cleft. The actual values of the parameters we used in the simulations are given in the Method section below. The full system was solved using explicit finite different schemes [35].

The binding of single Ca^{2+} ions could not be modelled literally in the continuous model, because single Ca^{2+} ions do not exist in the model. However, in a Markov chain model of a RyR, the Ca^{2+}-dependent transition between one state to another is an indirect model of the physiological event of a Ca^{2+} ion binding to a receptor at a channel [36, 37]. Given that we did not want to simulate the dynamics of the whole RyR, but only the transition between two $\left[Ca^{2+}\right]$-dependent states, we reduced the channel model to only include two states: one with Ca^{2+} bound, cR, and one with Ca^{2+} unbound, R,

$$R \underset{k^-}{\overset{c\,k^+}{\rightleftharpoons}} cR. \tag{9}$$

The total binding rate depends on the Ca^{2+} concentration, c, at the position of the receptor together with the on rate, k^+. The unbinding rate depends only on the off rate k^- and is thus Ca^{2+}-independent. The independency of $\left[Ca^{2+}\right]$ in the off rate makes the transition from the bound state to the unbound state model-independent, and we could therefore exclude it from our study because we were only interested in the differences. Effectively, this meant that we removed the bound state, cR, from the receptor model, thus reducing the receptor model to a one-state model that serves as an indicator of Ca^{2+} binding events.

With this reduction of the channel model, we were able to represent the registration of single Ca^{2+} binding events at a RyR, in the continuous model, with a Poisson processes, determined only by the rate or intensity function $\lambda(t) = c(t)k^+$ [38]. The probability that one Ca^{2+} ion would bind to a RyR was modelled as 1 minus the probability of zero bindings:

$$P_{_B}(t) = 1 - \mathrm{e}^{-\lambda(t)\Delta t}\,. \tag{10}$$

We had to retain the quantity $\lambda(t)\Delta t$, which represents the expected number of binding events during a time step, much smaller than 1, and by that minimizing the probability of getting more than one binding event during a time step. When the $\left[Ca^{2+}\right]$ was fixed at each receptor, i.e., during the steady-state, we had a homogeneous Poisson process with constant rate $\lambda = c\,k^+$. In the transient simulation, where the $\left[Ca^{2+}\right]$ varied at each receptor, the Poisson process was inhomogeneous with rate $\lambda(t) = c(t)k^+$. The model reduction, together with the observation that the registration of binding events could be represented by a Poisson process, were used in the goodness-of-fit tests, as shown in the Methods section below.

2.2 Random Walk model

Our discrete model of diffusion is based on a RW description of Brownian motion [39]. The model is a simple, but powerful stochastic model of diffusion. In a simulation, the position of each diffusive ligand in the cleft is tracked. For each ligand and time step, a random displacement, $\Delta\boldsymbol{r} = (\Delta x,\, \Delta y,\, \Delta z)$, is sampled from a trivariate probability density and added to the position of the ligand. The distribution is a solution to Fick's second law of diffusion for a point source [33]. With homogeneous diffusion constant, D, and a fixed time step, Δt, the trivariate probability density is given by

$$f(\Delta\boldsymbol{r},\Delta t,D) = \frac{1}{(4\,\pi\,D\,\Delta t)^{\frac{3}{2}}}\;\mathrm{e}^{-\frac{\Delta x^2+\Delta y^2+\Delta z^2}{4\,D\,\Delta t}}\,. \tag{11}$$

The expected radial displacement of a single RW step is $r_{_E} = \sqrt{6D\Delta t}$. The spatial scale of the simulation is hence set by D and Δt. Three different types of diffusive ligands were simulated in the RW model: Ca^{2+}, and a diffusive buffer with and without bound Ca^{2+}. We used the same diffusion constant for the two buffer molecules, D_b. Two different types of boundary were used: one reflective and one absorbing, $\partial\Omega_{\mathrm{N2}}$ and $\partial\Omega_{\mathrm{D}}$ in Fig. 6. If a particle, Ca^{2+} or mobile buffer, crossed one of the reflective boundaries it was mirrored into the volume again. If a Ca^{2+} ion crossed the absorbing boundary it was removed from the simulation, to allow the modelling of a Ca^{2+} concentration in cytosole that was assumed to be zero. During a simulation, we kept the total concentration of the

mobile buffer constant in the cleft. This was achieved by not allowing a buffer molecule cross to the $\partial\Omega_{\mathrm{D}}$ boundary, i.e., if a buffer molecule ended outside the boundary a new displacement was sampled until it was inside. In addition, if the buffer molecule had a Ca^{2+} ion attached to it when it ended outside the boundary, the Ca^{2+} was removed, due to the assumed zero $\left[Ca^{2+}\right]$ in the Cytosole.

We implemented two different possible sources of Ca^{2+} ions in the cleft: *i*) one or more LCC, or *ii*) passive influx from the cytosole. The Ca^{2+} ions that entered through a LCC were introduced into the centre of the cleft at a random height, to mimic the line source used in the continuous model; see above. The number of Ca^{2+} ions entering the cleft through the current per ms is given by $J_{LCC} = N_O\,\bar{i}_{LCC}/(z\,e)$, where N_O is the number of open channels, e the elementary charge, and z the valence of the Ca^{2+} ion. The number of Ca^{2+} ions entering the cleft from the cytosole is given by $J_{cyt} = C_{cyt}\,Na\,V/\bar{t}$. These ions were placed at a random position at the boundary $\partial\Omega_{\mathrm{D}}$. Here, C_{cyt} is the Ca^{2+} concentration in cytosole, Na Avogadro's number, and V the volume of the cleft. $\bar{t}$ is the average time each Ca^{2+} ion spent in the cleft, given that it entered at the boundary $\partial\Omega_{\mathrm{D}}$. When there were no buffers in the cleft, this value was found to be $\bar{t} \simeq 3.6 \times 10^{-4}$ ms.

Stochastic modelling of single receptors

In addition to handling the RW of single Ca^{2+} ions in a continuous 3D space, we wanted to let these ions bind to single receptors and study the resulting binding statistics. We did not find any software that was able to do this when we started our study, e.g. MCell 2 only supported single binding events to a density of receptors at the membrane. Therefore, we decided to develop our own model of bi-molecular interactions.

Not only RyRs were treated as single receptors in the discrete RW model, but also all buffer molecules, so we had to deal with Ca^{2+} unbinding from receptors too. This was in contrast to the continuous case, in which only the event of Ca^{2+} binding to single RyR receptors was treated stochastically. The probability that a Ca^{2+} ion will unbind from a receptor during a time step depends solely on the unbinding rate k^- for the receptor and the size of the time step and is given by

$$P_{UB} = 1 - \mathrm{e}^{-k^-\,\Delta t}\,. \tag{12}$$

The probability that a Ca^{2+} ion and a receptor will bind was calculated using the same macroscopic rate law that was used in the continuous case; see Eq. 9. It is counter intuitive to use a macroscopic law between single discrete molecules, because these do not have the macroscopic property of concentration. However, because the position of a diffusive ligand is given by a probability distribution between the time steps, we used this distribution to calculate the average number density of a single diffusive particle at a certain distance and time [7]. This quantity is deterministic and predicts the expected density or concentration of a particle.

Despite the fact that the concept of average number density has been used before [7] we argue that a single diffusive particle is described more appropriately in terms of its expected concentration, which is given in Molar and can thus be used in the macroscopic rate law, as intended. The word *expected* also reflects the deterministic *a*

priori knowledge of the contribution to the average concentration that a particle would make if the position were sampled many times.

We derived the concept of expected concentration by dividing the entire spatial domain that surrounds the diffusive ligand into N equally spaced shells. Each shell had a volume of $\Delta V_i = 4\pi\Delta S_i^2\delta s$, where $\Delta S_i = i\,\delta s$, $\delta s \propto 1/N$ and $i = 1 \ldots N$. Fixing the time to $t < \Delta t$, we sampled the position of the diffusive ligand K times. Let N_i be the number of times the ligand occurred in the shell at ΔS_i. Dividing this by K, we obtained the averaged number of times the ligand occurred in the ith shell. Then, the average number density of the particle in the same shell is given by

$$\bar{n}_i = \frac{N_i}{K\,\Delta V_i}. \tag{13}$$

Dividing this by Avogadro's number, Na, we arrived at the average concentration given in Molar. Given that we were sampling a deterministic probability distribution K times, we used this information to express the expected number of times a particle occurred in the ith shell, after time t:

$$N_{_E i} = K \times P(_{\Delta S_i,t}) = K \times f(_{\Delta S,t}) \times \Delta V_i. \tag{14}$$

Substituting N_i in Eq. 13 with this value, and letting $N \to \infty$, we obtain the expected concentration that this ligand exsert after t ms at distance ΔS,

$$c_{_E}(_{\Delta S,t,D}) = \frac{1}{Na} f(_{\Delta S,t}) = \frac{1}{Na(4\,\pi\,D\,t)^{\frac{3}{2}}} \mathrm{e}^{-\frac{\Delta S^2}{4\,D\,t}}. \tag{15}$$

Here we have divided by Avogadro's constant to obtain the concentration in Molar. We see that the $c_{_E}$ is directly proportional to the probability distribution in Eq. 11, which makes sense. The expected concentration of a single Ca^{2+} ion after $t = 45$ ns, with $D = D_c = 10^5$ nm^{2}ms^{-1}, is plotted against ΔS in the left panel of Fig. 1, solid line.

The expected concentration, $c_{_E}$, a Ca^{2+} ion exsert to a nearby receptor, ΔS nm away after τ ms, was used to calculate the probability of not binding during a tiny time interval $\Delta\tau \ll \Delta t$. For this we used the macroscopic rate law from Eq. 9 together with the Poisson probability distribution for zero events,

$$P_{nb}(_{\Delta S,\tau,D,\Delta\tau}) = \mathrm{e}^{-k^+ c_{_E}(_{\Delta S,\tau,D})\Delta\tau}\,. \tag{16}$$

The probability of not binding during the whole time step Δt, equals the product of this quantity evaluated for $\tau_i = \Delta\tau(i + 1/2)$, where $i = 0, \ldots, N$, and $N = \Delta t/\Delta\tau$. Keeping D, Δt, k^+ and ΔS constant, this probability is

$$P_{_{NB}} = \prod_{i=0}^{N} \mathrm{e}^{-k^+ c_{_E}(\tau_i)\Delta\tau} = \mathrm{e}^{-k^+ \sum_{i=0}^{N} c_{_E}(\tau_i)\Delta\tau} = \mathrm{e}^{-k^+ \bar{c}_{_E}\Delta t}, \tag{17}$$

where $\bar{c}_{_E}$ equals the average value of $c_{_E}$, the receptor experience during a time step. In the limit where $\Delta\tau \to 0$ and $N \to \infty$, $\bar{c}_{_E}$ becomes

$$\bar{c}_{_E} = \lim_{N\to\infty} \frac{1}{\Delta t} \sum_{i=0}^{N} c_{_E}(\tau_i)\Delta\tau = \frac{1}{\Delta t} \int_0^{\Delta t} c_{_E}(\tau) d\tau. \tag{18}$$

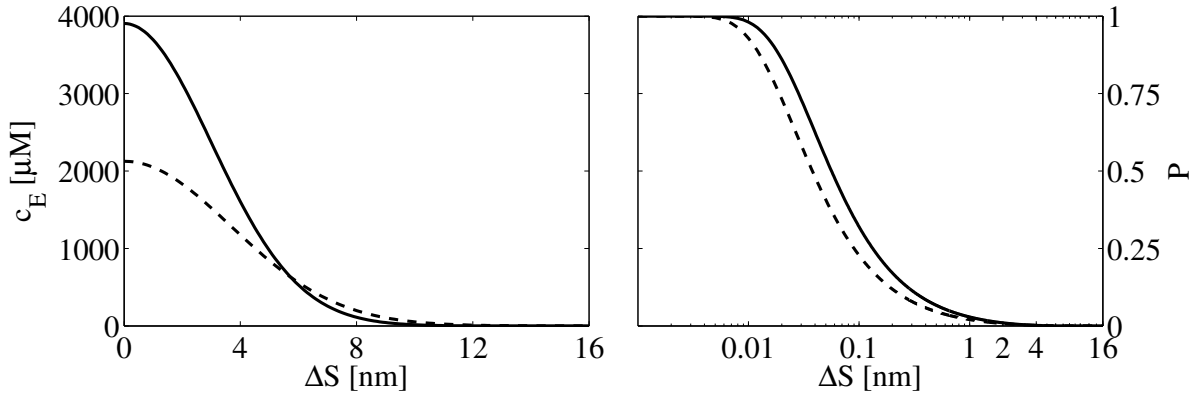

Figure 1: The left panel shows the expected $\left[\mathrm{Ca}^{2+}\right]$, as given by Eq. 15, experienced by a receptor situated a distance ΔS from it, at $t = 45$ ns. The diffusion constant of Ca^{2+} is $D_c = 10^5$ nm^{2}ms^{-1}. The solid line represents the $\left[\mathrm{Ca}^{2+}\right]$ experienced by a stationary receptor and the dashed line represents the $\left[\mathrm{Ca}^{2+}\right]$ experienced by a mobile receptor, with $D_b = D_c/2$, as given by Eq. 26. The right panel shows the corresponding probabilities that a Ca^{2+} ion will bind to a stationary receptor, solid line, and to a mobile receptor, dashed line, as given by Eq. 24, where $\Delta t = 45$ ns and $k^+ = 30\ \mu\mathrm{M}^{-1}\mathrm{s}^{-1}$. The probabilities are plotted against the distance between the Ca^{2+} ion and the receptor. Note the logarithmic scale used for ΔS in the right panel.

Using the function for $c_{_E}$ from Eq. 15, in this equation we get

$$\bar{c}_{_E} = \frac{1}{(4\,\pi\,D)^{\frac{3}{2}}\,Na\Delta t}\int_0^{\Delta t}\tau^{-\frac{3}{2}}\mathrm{e}^{-\frac{\Delta S^2}{4\,D\,\tau}}d\tau. \tag{19}$$

With change of variables, the integral on the right hand side can be represented by the upper incomplete gamma function [40]. The lower part of such a function is defined as

$$\Gamma_{inc}(x,\alpha) = \frac{1}{\Gamma(\alpha)}\int_0^x t^{\alpha-1}\mathrm{e}^{-t}dt \tag{20}$$

and the upper part is defined from this

$$\Gamma_{inc}^{upper}(x,\alpha) = \frac{1}{\Gamma(\alpha)}\int_x^\infty t^{\alpha-1}\mathrm{e}^{-t}dt = 1 - \Gamma_{inc}(x,\alpha). \tag{21}$$

After the change of variables, the integral in Eq. 19 becomes

$$\int_0^{\Delta t}\tau^{-\frac{3}{2}}\mathrm{e}^{-\frac{\Delta S^2}{4\,D\,\tau}}d\tau = \frac{\sqrt{4D}}{\Delta S}\int_{\frac{\Delta S^2}{4D\Delta t}}^\infty t^{-\frac{1}{2}}\mathrm{e}^{-t}dt = \frac{\sqrt{4\pi D}}{\Delta S}\left[1 - \Gamma_{inc}\left(\tfrac{\Delta S^2}{4D\Delta t},\tfrac{1}{2}\right)\right], \tag{22}$$

where the identity of $\Gamma(\frac{1}{2}) = \sqrt{\pi}$ has been used. Using this in Eq. 19, we obtained an analytical expression of the average expected concentration that a receptor experiences during a time step from a nearby ligand:

$$\bar{c}_{_E} = \frac{1}{4\,\pi\,D\,\Delta s\,Na\,\Delta t}\left[1 - \Gamma_{inc}\left(\tfrac{\Delta S^2}{4D\Delta t},\tfrac{1}{2}\right)\right]. \tag{23}$$

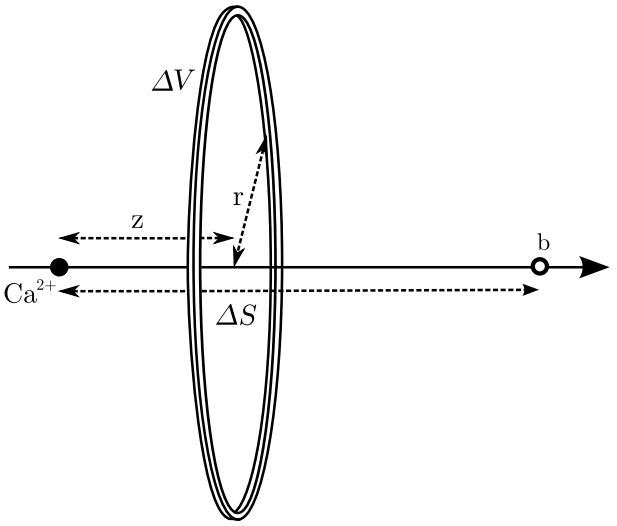

Figure 2: The figure shows the coordinate used to integrate the $\left[Ca^{2+}\right]$ experienced by the buffer molecules, b. The position of the Ca^{2+} ion defines the origin and the distance between the two particles is ΔS.

Assuming that the quantity $k^+\bar{c}_{E}\Delta t \ll 1$, we can write the probability of registering only one binding event as

$$P_{B} = 1 - P_{NB} = 1 - \mathrm{e}^{\bar{\lambda}\Delta t}, \tag{24}$$

where $\bar{\lambda} = k^+\bar{c}_{E}$. This equation is analogous to Eq. 10, applied only to a single ligand. The expected number of binding events during a time step is $\langle N_{B}\rangle = \bar{\lambda}\Delta t$. For the continuous case, we had to keep this value much smaller than one, in order to minimize the probability of getting two or more binding events during a time step. See also the validity study below.

The binding probability for a Ca^{2+} ion near to a mobile receptor, i.e. a mobile buffer, was modelled in the same way as for the stationary receptor, with one exception. A mobile buffer moves during a time step, which leads to a difference in the expected concentration experienced by the buffer from a nearby Ca^{2+} ion. Instead of evaluating c_{E} at a single point, as for the stationary receptor, we evaluated it for all possible positions, $c_{E}(\boldsymbol{r}, t)$, and weighted these with the probability, $p_m(\boldsymbol{r}, t)$, that the buffer was present. For an arbitrary spatial point $\boldsymbol{r}$, this quantity is

$$c^{p}_{Em}(\boldsymbol{r}, t) = c_{E}(\boldsymbol{r}, t) \times p_m(\boldsymbol{r}, t) = \frac{f_c(\boldsymbol{r}, t)}{Na} f_m(\boldsymbol{r}, t)\Delta V(\boldsymbol{r}), \tag{25}$$

where f_c and f_m are the values of the probability density for the Ca^{2+} and the mobile buffer molecule, respectively. The superscript, p, denotes the concentration at a single spatial position. Using angular symmetry, a cylindrical coordinate system was chosen to integrate, c^{p}_{Em} over all spatial points. The Cartesian coordinate line, z, was placed in line with the two particles; see Fig. 2, and the position of the Ca^{2+} ion defines the origin. The distance between the two particles is ΔS. The result of the integration was the expected Ca^{2+} concentration experienced by a nearby mobile receptor, at time, t,

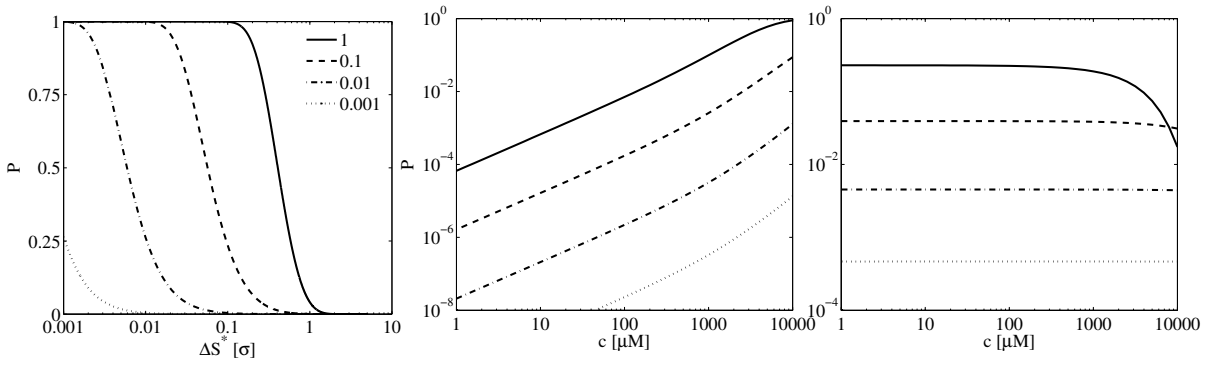

Figure 3: The figures show the results of our study of the validity of the model of the bi-molecular binding probability in Eq. 24. The left and the middle panels show the probability of registering two or more binding events at a receptor. The left panel shows the probability generated by a single ligand, with respect to the dimensionless quantities, ΔS^* and k^{+*}, whereas the centre panel shows the overall probability of registering two or more binding events at a receptor in an infinite medium with constant concentration, c, for different values of k^{+*}. The right panel shows the absolute value of the relative difference between the probability of registering a binding event from the continuous model and the RW model. The curves in the centre and right panels were computed using $\sigma = 5$ nm and $D = 10^5$ nm^2 ms^{-1}. These curves would be shifted downwards if a smaller σ were chosen.

separated by a distance ΔS,

$$\begin{aligned} c_{Em}(\Delta S,t) &= \frac{1}{4\pi^2 Na\left(4\,D_c\,D_b\,t^2\right)^{\frac{3}{2}}}\int_{-\infty}^{\infty}\int_{0}^{\infty} r\mathrm{e}^{-\frac{r^2+z^2}{4D_c t}}\mathrm{e}^{-\frac{r^2+(\Delta S-z)^2}{4D_b t}}\,dr\,dz, \\ &= \frac{1}{Na(4\pi(D_c+D_b)t)^{\frac{3}{2}}}\mathrm{e}^{-\frac{\Delta S^2}{4(D_c+D_b)t}} \end{aligned} \tag{26}$$

Here, D_c and D_b are the diffusion constants of the Ca^{2+} ion and the mobile buffer. Notice that this expression is identical to the expected concentration experienced by a stationary receptor, i.e. Eq. 15, with $D = D_c + D_b$. This result made it possible to use Eq. 24 to calculate the binding probability of a Ca^{2+} ion to a nearby mobile receptor, merely by setting the diffusion constant, D, to the sum of the diffusion constants of the two particles. In Fig. 1, left panel, dashed line, the expected concentration of a Ca^{2+} ion experienced by a nearby tentative mobile buffer is plotted. In the same figure, right panel, dashed line, the calculated probability of a nearby Ca^{2+} ion to bind to the same mobile buffer, during a time step of $\Delta t = 45$ ns, with $D_c = 10^5$ nm^{2}ms^{-1}, $D_b = D_c/2$ and $k^+ = 30\mu$Ms^{-1}, is plotted.

Validity study of bi-molecular binding probability

The model of the bi-molecular binding probability requires that a single receptor registers only one binding event per time step. In the continuous model, this could be controlled by keeping the expected number of binding events during a time step, $\langle N_B \rangle = c(t)k^+\Delta t$, much smaller than one. The corresponding probability of getting two or more binding events per time step is then small. Using the Poisson probability distribution, this

equals 1 minus the sum of the probabilities of 0 and one binding per time step:

$$P_{>1} = 1 - \left(\mathrm{e}^{-\langle N_B \rangle} + \langle N_B \rangle \, \mathrm{e}^{-\langle N_B \rangle} \right). \tag{27}$$

Using typical large values for the physical parameters, $\left[\mathrm{Ca}^{2+}\right] \simeq 1$ mM and $k^+ = 100$ $\mu\mathrm{M}^{-1}s^{-1}$ and a small value for the time step $\Delta t = 1.25 \times 10^{-4}$ ms, we obtained a small expected number of bindings per time step $\langle N_B \rangle = 1.25 \times 10^{-2}$ and a very small value for the probability of two or more binding events, $P_{>1} \simeq 8 \times 10^{-5}$.

A similar analysis for the bi-molecular binding model was not straightforward. The expected number of binding events during a time step for a single ligand, $\langle N_B \rangle = \bar{c}_E k^+ \Delta t$, depends on the stochastic ΔS-variable, and we must ensure that the probability for more than one nearby ligand to bind to the receptor is small. The latter probability depends on the local density of ligands nearby the receptor and is also a stochastic entity.

Depending on the parameters, $\langle N_B \rangle$ can well exceed 1, which increases the probability of registering two or more binding events from a single diffusive ligand. To study this probability with arbitrary parameters, we expressed the expected number of binding events per time step, $\langle N_B \rangle$ using dimensionless units. We let the expected displacement of a single ligand in one spatial direction, $\sigma = \sqrt{2D\Delta t}$, define the length scale $\Delta S = \sigma \Delta S^*$. The expected number of binding events per time step in dimensionless units is then

$$\langle N_B \rangle = k^{+*} \left[1 - \Gamma_{inc} \left(\tfrac{\Delta S^{*2}}{2}, \tfrac{1}{2} \right) \right] / \Delta S^*, \tag{28}$$

where

$$k^{+*} = k^+ / \left(4\pi D \sigma N a \right) \tag{29}$$

and represents the dimensionless version of k^+. Note that Δt is redundant because it follows D and σ. Using this in Eq. 27, we obtained the probability of getting two or more binding events from a single diffusive ligand nearby a receptor. This quantity is plotted for different values of k^{+*} and ΔS^* in the left panel of Fig. 3. The probability is sensitive to ligands that are very close to the receptor and to large values of k^{+*}.

In an infinite medium with a constant concentration, the probability that a ligand will be r dimensionless units away from a receptor is $P(r) = 2\pi\sigma^3 \, c \, N a \, r^2 \Delta r$, where c is the concentration and Δr a small distance chosen to ensure that $P(r) \ll 1$. The probability of not getting a binding event from a distance r equals the probability that a ligand will not be at that distance plus the probability that a ligand will be there times the probability of not binding from that distance. Keeping k^{+*} and c constant we get $P_r^0 = 1 - P(r) + P_{NB}(r) P(r)$, where $P_{NB} = \mathrm{e}^{-\langle N_B \rangle}$, and $\langle N_B \rangle$ is distance-dependent; see Eq. 28. We chose a cutoff distance of $r = 5$ that defines our domain and computed the probability of not registering any binding events from this volume, $P^0 = \prod_i P_{r_i}^0$, where $r_i = i\Delta r$. The probability of getting one binding from a distance r is $P_r^1 = P_1(r) P(r)$, where $P_r^1 = \langle N_B \rangle \, \mathrm{e}^{-\langle N_B \rangle}$. The probability of registering only one binding event from the distance r and not from any other distances equals $P^0 \times P_r^1 / P_r^0$. Finally, the probability of registering only one binding event from the whole domain is the sum of all these probabilities:

$$P^1 = P^0 \sum_i P_{r_i}^1 / P_{r_i}^0. \tag{30}$$

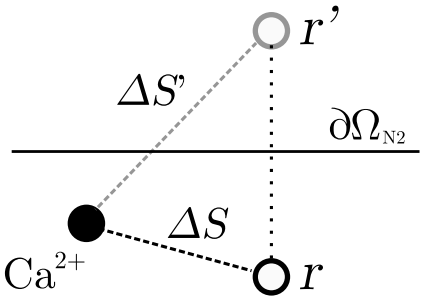

Figure 4: The figure illustrates how the reflection of a receptor near a membrane is modelled. $\partial\Omega_{\mathrm{N2}}$ is the reflecting boundary of the membrane, r and r' are the position of the receptor at its actual position and at its mirrored position. ΔS and ΔS' is the distance between the Ca^{2+} ion and the actual position of the receptor and the position of the mirrored one.

The probability of registering two or more binding events from the whole domain is then $P_{>1} = 1 - (P^0 + P^1)$. This quantity is plotted for different values of c and k^{+*} in the centre panel of Fig.3. Because it is not straight forward to interpret a dimensionless $\left[\mathrm{Ca}^{2+}\right]$, we chose to plot this variable with physical values. To do this we had to choose physical values for D and σ for the figure. These parameters were set to $\sigma = 5$ nm and $D = 10^5$ nm^2 ms^{-1} and yielded the result shown in the plot. A smaller σ, i.e., a smaller time step, will result in the curves shifting downwards. We see that the probability of registering more than one binding event per time step is quite large for high concentrations; more than 1 mM for the largest values of k^{+*}. In this particular case, the solid and dashed line represents an on rate of, respectively, 3800 and 380 $\mu\mathrm{M}^{-1}s^{-1}$, which are quite large values.

We were able to define the probability of registering a binding event from our test domain during a time step as $P_B^{RW} = 1 - P^0$ and compare this with the continuous equivalence from Eq. 10, for convenience here named P_B^C. Using the same values for the parameters as above, we computed the absolute value of the relative difference between these two models, $\left|P_B^{RW} - P_B^C\right| / P_B^C$. The result is shown in the right panel of Fig. 3. We see that the difference is very small and is more or less constant for different values of c. The downward bend seen for the largest values of k^{+*} represents the difference between the two models in a parameter range in which both models produce erroneous probabilities and should, therefore, be ignored. These results indicate clearly the similarities in registered binding events between the two models for a large parameter range.

Reflecting boundaries

The reflecting property of a membrane increases the expected concentration of a nearby Ca^{2+} ion. A receptor at or close to the membrane will therefore experience a higher concentration from a single Ca^{2+} ion and hence a larger probability of binding. The increase was included by mirroring the location of a receptor close to a membrane, to the opposite side, as illustrated in Fig. 4. The probability of binding was then calculated for this mirrored position and added to the initial probability,

$$P'_B = 1 - \left[1 - P_B(\Delta s)\right]\left[1 - P_B(\Delta s')\right] \simeq P_B(\Delta s) + P_B(\Delta s') \tag{31}$$

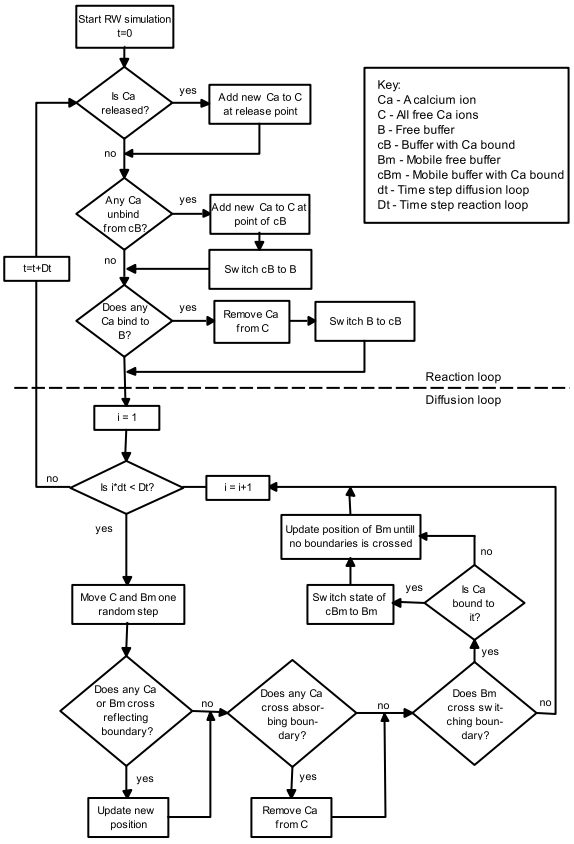

Figure 5: The figure illustrates a time step in the RW algorithm. The upper part, above the dashed line, shows the reaction loop and the lower part shows the diffusion loop. The reaction loop is simulated with a coarser time step, Dt = 125 ns, than the diffusion loop, dt = 5 ns.

Here, ΔS is the distance between the Ca^{2+} ion and the actual position of the receptor and ΔS' is the distance between the ion and the mirrored receptor. The approximation in Eq. 31 holds for probabilities much smaller than 1. If the receptor is situated at the membrane, we have $\Delta S = \Delta S$'. For simplicity, we mirrored all buffers in the upper part of the cleft to the opposite side of the SR membrane and all buffers in the lower part of the cleft to the opposite side of the TT membrane.

Monte Carlo simulation of binding

To speed up the Monte Carlo simulations of the reaction, we precomputed the probability of unbinding and binding of a single Ca^{2+} ion for each type of receptor included in the simulation. The unbinding probability for each buffer type was very small, which allowed us to assume that only one Ca^{2+} ion could unbind during a full time step. With this assumption, we only had to sample one uniform random number per time step for the unbinding reactions. This number was compared to a lumped unbinding probability that is given by

$$P_{UB}^{l} = 1 - (1 - P_{UB})^{N}, \tag{32}$$

where P_{UB} is given by Eq. 12 and N is the number of buffer molecules that have a Ca^{2+} ion bound to it.

The probabilities of binding were precomputed with respect to ΔS and a look-up table was used during the simulation. To speed up this process even more, only Ca^{2+} ions within a certain maximal distance to the receptor were considered. This distance was chosen so that the probability of binding at this distance equalled 10^{-6}. The actual Monte Carlo sampling was performed as follows: *i*) traversing the empty receptors in a random order each time step, *ii*) for each empty receptor, calculating the probability of binding for all Ca^{2+} ions within the maximal distance, *iii*) distributing these probabilities in a cumulative distribution, $0 < C_{p1} < C_{p2} \ldots < C_{pN} < 1$, where N is the number of Ca^{2+} ions within the maximal distance and C_{pi} is the cumulative binding probability of the ith Ca^{2+} ion, and finally, *iv*) drawing a uniformly distributed random number between 0 and 1. No Ca^{2+} ion was bound if the random number was larger than C_{pN}. If the random number was in between $C_{p(i-1)}$ and C_{pi}, the ith Ca^{2+} ion was bound to the receptor. By choosing a small enough time step, Δt, we ensured that both the single binding probability and the sum of all binding probabilities always was much smaller than 1. This minimized the error made in assuming that only one Ca^{2+} ion could bind to one receptor during a time step.

Random Walk algorithm

A full step in our RW algorithm is presented schematically in Fig. 5. First, any Ca^{2+} that is scheduled to enter the cleft at the present time step, is added to the variable that keeps track of all Ca^{2+} ions. After that, we check whether any Ca^{2+} ions were bound to mobile or stationary buffers or to the included RyRs, using the precomputed binding probabilities from Eq. 24. Then, we update the mobile buffers and the Ca^{2+} ions with new positions, using the Monte Carlo method presented above. The first procedure (the reaction loop) operated on a larger timescale than the second (the diffusion loop). A single step in the reaction loop took much longer and the accuracy was not so sensitive to the time step, which allowed us to simulate this procedure at a larger time scale. The sampling of new displacement in the diffusion loop was cheap, but the escape rate of the Ca^{2+} ions leaving the cleft by the absorbing boundary $\partial\Omega_{\mathrm{D}}$, was underestimated [41]. This error was time-step dependent and was therefore minimized by using smaller time steps in this loop.

3 Methods

All simulations, plots, and statistical tests were done using Matlab [42] on a GNU/Linux laptop, with 1 GB Ram and a 2.1 GHz Pentium M processor.

3.1 Morphology and boundaries

Following Ref. [21] we modelled the dyadic cleft as a disk (see Fig. 6), with h = 15 nm and R = 100 nm. The diffusion constant of Ca^{2+} was set to $D_c = 10^5$ nm^2 ms^{-1} [29]. The single LCC current amplitude was chosen to be $\bar{i}_{LCC} = 0.3$ pA [43], and was released

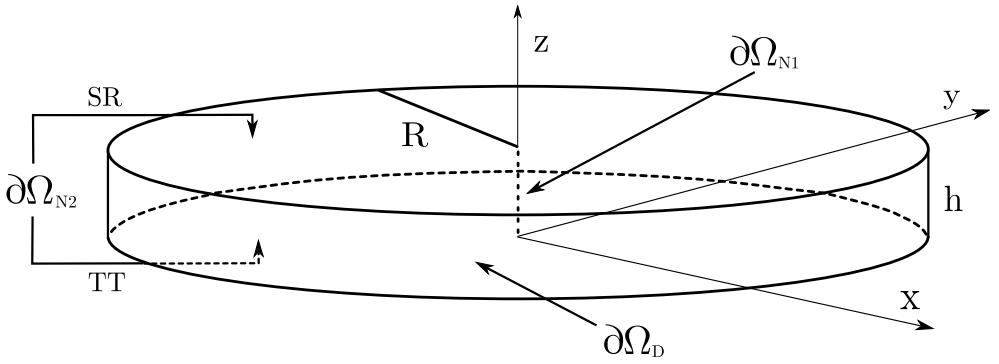

Figure 6: The figure shows the geometry of the disk that we used to model the dyadic cleft. The LCC ion source is included in the centre of the disk as a line source.

in the centre of the disk along the dashed line in Fig. 6. In one of the simulations, we included both mobile and stationary endogenous buffers, using rates and concentrations parameters from a previous study [44]; see Table 1. The diffusion constant of the mobile buffer, calmoduline, was set to $D_m = 0.1 \times D_c$ [21]. Several open LCCs were modelled by multiplying the source amplitude by the number of open channels. The binding rate for the RyRs was set to 5 $\mu\mathrm{M}^{-1}\mathrm{s}^{-1}$, which corresponds to binding rates previously used in models for both RyR and LCC [36, 45]. The TT and SR membranes were modelled as reflective, no-flux, boundaries, $\partial\Omega_{\mathrm{N2}}$ in Fig. 6. The cytosole was included in the model either as a zero concentration boundary, when a LCC Ca^{2+} source was used, or as a constant level corresponding to diastolic $\left[Ca^{2+}\right]$ of 0.1 μM; see $\partial\Omega_{\mathrm{D}}$ in Fig. 6.

3.2 Simulation setups and binding event registrations

As mentioned in the Introduction, we considered the event of a single Ca^{2+} ion binding to a receptor to be the stochastic event that determines the functional properties of the dyadic cleft. We tested how well the continuous model fits the equivalent binding events registered from the RW model. We used four tentative RyRs, positioned from the centre of the cleft to the rim, to test whether the radial position of single receptors had any effect on the event registrations. We performed three different set of simulations, in which binding events were registered under different physiological conditions. These conditions were as follows: *i*) steady-state $\left[Ca^{2+}\right]$ response due to one open LCC, *ii*) uniform $\left[Ca^{2+}\right]$ due to passive diffusion from cytosole, using very low diastolic $\left[Ca^{2+}\right]$ = 0.1 μM, and *iii*) transient $\left[Ca^{2+}\right]$ response from three different LCCs, which alternated between closed and open during the simulations. The statistical results from these three sets of simulations are presented in Figs. 8-10.

Each set of simulations had different deterministic Ca^{2+} influxes, corresponding to each physiological situation, and was run 100 times. Stochastic binding events from four different RyRs were registered. The RyRs were located along the same axis at radial distances of 10, 30, 50, and 70 nm.

Table 1: Ca^{2+} buffer parameters

Ca^{2+} buffer	k^+ $[\mu M^{-1}s^{-1}]$	k^- $[s^{-1}]$	B^T $[\mu M]$
Calmoduline	100	38	24
SL membrane	115	1000	1124

One open LCC, steady-state $[Ca^{2+}]$

In the first set of RW simulations, we registered the binding events from the steady-state response of a single open LCC in the cleft. The Ca^{2+} influx in these simulations consisted of one open LCC situated at the centre of the cleft. Initially, the cleft had zero Ca^{2+} ions, so registration was started after 0.2 ms, after the steady-state was achieved, and the runs were stopped after 30 ms. In these runs, we were only interested in the binding events during the steady-state $[Ca^{2+}]$ in the cleft, so we excluded both stationary and mobile buffers from the simulations, thereby achieving a significant gain in speed. The mobile buffer actually lowers the steady-state $[Ca^{2+}]$. Therefore, it could be argued that it should have been included in these simulations [21]. However, neither its inclusion nor exclusion would influence the results of the comparison study, which was the main focus. The steady-state solution of $[Ca^{2+}]$ from the continuous model, which was used in the comparison study (see below) is presented in the inset of Fig. 8 A.

Diastolic steady-state $[Ca^{2+}]$

In the second set of RW simulations, we tested the effect on the binding events when $[Ca^{2+}]$ was extremely low. Instead of Ca^{2+} influx through a channel, we had passive Ca^{2+} influx from the cytosole. The value of the $[Ca^{2+}]$ that we used corresponded to a diastolic concentration of 0.1 μM. In these simulations, we did not include any buffers, because the Ca^{2+} response was stationary. Due to the small number of Ca^{2+} ions in the cleft, about 0.02 on average, each run had to be long (30 s) to produce reliable statistics for the tests.

Transient $[Ca^{2+}]$

In the third and last set of RW simulations, we studied binding events that were registered during a transient response in the cleft. Both stationary and mobile buffers were included in these simulations. The Ca^{2+} influx came through three LCCs that alternated between open and closed; see inset of Fig. 10 A for the resulting LCC current. Each run lasted for 22 ms.

3.3 Comparison methods

Two different hypotheses about the statistical outcome of the binding events were formed for each RyR and for each set of simulations: *i*) the mean number of events during a simulation run are the same for both models, and *ii*) the inter-event intervals

(IEIs) of the registered binding events are the same for both models. Each of these hypotheses was tested for each RyR and for each set of simulations.

To perform the tests, we needed the solution of the continuous concentrations at each RyR. In the first set of simulations, Ca^{2+} entered the cleft from one single LCC and no buffers were present. Setting B_m^T and B_s^T to zero in Eq. 8-4, the steady-state solution could be solved analytically with respect to r; see the inset of Fig. 8 A. In the second case, in which Ca^{2+} entered the cleft passively through the cytosole, we fixed the concentration at the same level as for the cytosole, 0.1 μM for all RyRs. In the third case, we needed the $\left[Ca^{2+}\right]$ at every time step, c, for each RyR. We simulated the full system in Eq. 8-4 with the same input current as was used in the RW simulations. The $\left[Ca^{2+}\right]$ for the ith RyR and nth time step, c_n^i, was registered.

Test of mean number of events

Using the central limit theorem, we compared the mean number of binding events from each RyR against the expected number of binding events from the continuous model, with a one-sample Student's t-test. The continuous solution of $\left[Ca^{2+}\right]$ was used to compute the expected number of binding events, μ, of a whole run for each RyR. We calculated a 95 % confidence interval for the expected mean from the data collected from the RW simulations, together with the corresponding p-values for the Student's t-test. The expected number of binding events during a run of length T simulated with a homogeneous Poisson with rate λ^i is given by

$$\mu_{SS}^i = \lambda^i T = k^+ c^i T, \tag{33}$$

where c is the $\left[Ca^{2+}\right]$ at the ith receptor and k^+ the macroscopic binding rate [38]. In the last simulation setup, where the $\left[Ca^{2+}\right]$ varied, we had to integrate the rate function to get the expected number of binding events, which is given by

$$\mu_T^i = \int_0^T \lambda(t)\, dt = k^+ \int_0^T c(t)^i\, dt \simeq k^+ \Delta t \sum_{n=1}^{N} c_n^i. \tag{34}$$

Here, c_n^i is the value of the $\left[Ca^{2+}\right]$ in the nth time step and Δt the length of each step.

Test of same inter event intervals

IEIs were calculated from the binding event data from each RyR in of RW simulations. All IEIs from one RyR collected during one set of simulations were combined to form one distribution. The equivalent expected distributions from the continuous model were computed for each RyR, for all three simulation setups. The goodness-of-fit of the expected distributions was tested against the registered IEI distributions collected from the RW simulations, using a Kolmogorov-Smirnov (KS) test [46].

In the first two simulation setups, the $\left[Ca^{2+}\right]$ at each RyR was fixed and the resulting binding rates for each RyR were constant, forming homogeneous Poisson processes. The IEIs from an homogeneous Poisson process are distributed exponentially with the same rate as the Poisson process itself [38]. The expected IEI distribution for the ith RyR is given by

$$IEI^i(t) = \lambda^i \exp\left(-\lambda^i t\right) = k^+ c^i \exp\left(-k^+ c^i t\right). \tag{35}$$

These were used to compute the p-values of the KS tests; see Table 2. In the third simulation setup, the $\left[Ca^{2+}\right]$ at each RyR was not fixed yielding inhomogeneous Poisson processes. The resulting IEI distribution from such a process does not follow an exponential distribution.

A useful method for evaluating models of point processes in neural spike train data analysis, the Time-rescaling theorem ,was introduced by Brown et al. [47]. They used this theorem to transform registered event times from an inhomogeneous Poisson process to represent realizations of a homogeneous Poisson processes with unit rate. Given a serie of time events $0 < t_1 < t_2 <, \ldots, < t_n < T$ that realizes an inhomogeneous Poisson process with rate $\lambda(t) > 0$ for all $t \in (0, T]$, the transformed realization of a homogeneous Poisson process with unit rate is

$$\Lambda^i(t_k) = \int_0^{t_k} \lambda^i(t)dt = k^+ \int_0^{t_k} c^i(t)dt \simeq k^+ \Delta t \sum_{n=1}^{N} c_n^i, \tag{36}$$

for $k = 1, \ldots, n$. The IEIs of this process are $\tau_k = \Lambda(t_k) - \Lambda(t_{k-1})$ and they are exponentially distributed with unit rate. We used the rate from the continuous model to transform the IEIs registered from the RW model. These were then used in a goodness-of-fit test of an exponential function with unit rate.

Bonferroni procedure

We performed three different sets of RW simulations, collected binding events from four different RyRs, and performed two different statistical tests for each receptor. This left us with a total of 24 statistical hypotheses. For every test, the H_0 hypothesis was that the continuous model either predicted the mean number of binding events or fitted the IEI distributions with an appropriate exponential function. The overall hypothesis of how well the continuous model fitted the sampled binding event data from the full RW model had to be determined on the basis of these tests. The number of binding events during a run was not independent of the IEI distributions. If an IEI distribution is known to follow an exponential distribution, the expected number of events follows directly from the rate of this distribution, thus reducing the number of independent tests to 12. Given that we were doing 12 independent tests, each at $\alpha = 5\%$, there was a probability $P = 1 - 0.95^{12} = 0.46$, of getting at least one false rejection. The α level for each subtest was therefore adjusted such that our main hypothesis was tested at the 5 % level by using the conservative but simple Bonferroni procedure [46]. The new α level for each subtest was acquired by dividing the total α level by the number of subtests. This gave us an α level of 0.42 % for each subtest.

4 Results

4.1 Random Walk vs Continuous solutions

To confirm that the solution from the continuous model coincided with the mean concentrations from the RW model, we did one run with the continuous model and

Table 2: Binding event statistics

RyR positions	Student's t-test μ	95 % CI	p-values	KS-test p-values
One open LCC, steady-state $[Ca^{2+}]$				
10 nm	56.8	(54.3, 57.3)	0.22	0.17
30 nm	29.8	(28.4, 30.8)	0.74	*0.042
50 nm	17.1	(15.6, 17.2)	0.059	0.56
70 nm	8.79	(8.29, 9.41)	0.83	0.060
Diastolic steady-state $[Ca^{2+}]$				
10 nm	15.0	(14.0, 15.5)	0.51	0.10
30 nm	15.0	(14.1, 15.4)	0.49	0.54
50 nm	15.0	(14.0, 15.5)	0.48	0.055
70 nm	15.0	(13.8, 15.3)	0.25	0.56
Transient $[Ca^{2+}]$				
10 nm	68.3	(66.5, 70.1)	0.96	0.31
30 nm	35.6	(33.7, 36.1)	0.27	0.39
50 nm	20.4	(19.2, 21.0)	0.52	0.64
70 nm	10.4	(9.75, 10.8)	0.52	0.087

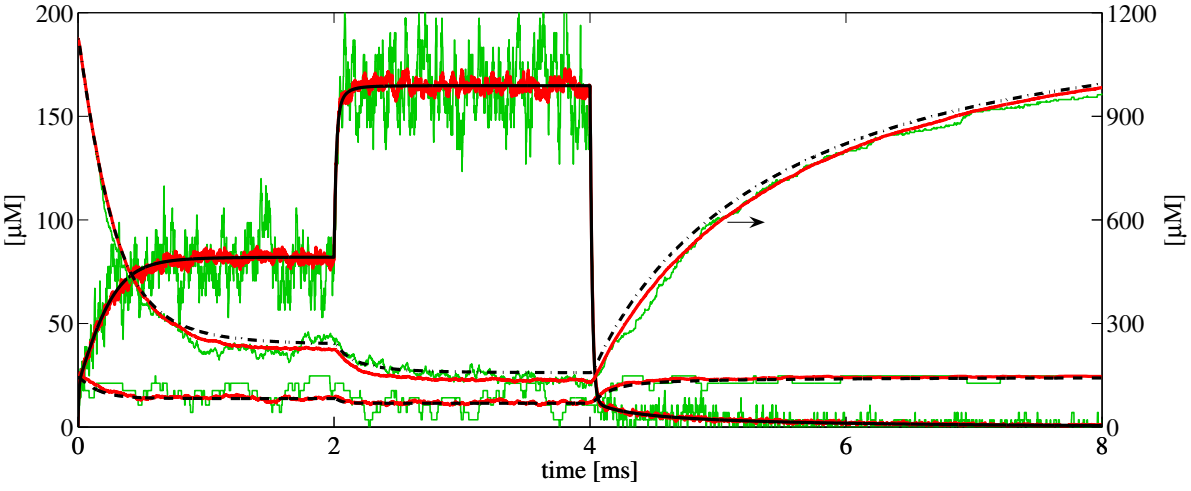

Figure 7: The figure presents simulation results from the continuous model (black lines) and from the Random Walk (RW) model (colored lines). The results represent the average concentrations from the whole cleft. The same simulation setup was used for the two models, including buffers from Table 1. One LCC is open from the start. After 2 ms one more opens. Then, after 4 ms, both close. The black lines are the results from one simulation of the continuous model. Each line, solid, dashed, and dash-dotted, represents the concentration of, Ca^{2+}, mobile buffer and stationary buffer, respectively. The right y-axis shows the scale for the stationary buffer. The coloured lines are the mean concentrations from 40 runs of the RW model (red lines), and the concentrations from a single RW simulation (green lines).

40 runs of the RW model, using the same parameters. The result is presented in Fig. 7. The black lines are the concentration in the cleft given by the continuous model of, respectively, Ca^{2+}, (solid line) mobile buffer, (dashed line) and stationary buffer (dash-dotted line). The coloured lines, partly covered by the black lines, are *i*) the concentration results from a single RW simulation (green lines), and *ii*) the average results from 40 RW runs (red lines). Note that the scale for the stationary buffer traces is given in the right y-axis. One LCC was opened at t=0, to act as a Ca^{2+} source in the cleft. After about 1 ms, the steady-state, in which most of the stationary buffers were bound to Ca^{2+}, was achieved. After 2 ms, a second LCC was opened. This time, the steady-state occurred more quickly, due to the fact that less stationary buffer was available. We see that the $\left[Ca^{2+}\right]$ in the single RW run fluctuates a great deal in the steady-state period, but the mean concentration does not. After 4 ms, both LCCs were turned off and the Ca^{2+} left the cleft quickly. Some Ca^{2+} remained, due to the unbinding of Ca^{2+} from the stationary buffer.

The result confirms what others have pointed out, that the continuous solution coincides with the mean result from several RW simulations [1–3]. We did see a difference between the mean concentration of the stationary buffer registered from the RW runs, and the corresponding concentration from the continuous solution. This error was introduced in the RW model, because we did not account for the absorbing boundary when calculating the probabilities that Ca^{2+} ions and the stationary buffer molecules near the rim would bind. By placing the RyRs well inside the cleft, the outermost being 30 nm from the rim, we avoided this error when binding probabilities for the receptors were calculated.

It is interesting to note that the large Ca^{2+} flux to the buffers, primarily to the stationary buffer, fluctuates significantly less than the out-flux of Ca^{2+} ions from the cleft. This is an effect of the low binding rate compared to the exit rate. The latter is approximately equal to the influx from the LCC during the steady-state, not including the small out-flux through the mobile buffer. The influx when two channels were open, between 2 and 4 ms, was approximately $J_{LCC} \simeq 1870$ ions per ms, and the binding rate to the stationary buffer during the same steady-state was $J_{SB} = c_{SS} \times k^+ \simeq 20$ ions per ms. This means that the out-flux is 100 times larger than the flux to the buffers.

4.2 Statistics of single binding events

As seen in Table 2, where the results of the Student's t-tests and the KS-tests are presented, the predicted distributions of binding events from the continuous model fit the corresponding distributions of registered binding events from the RW model. p-values and 95 % CI are included for the t-tests and the p-values are included for the KS-tests. We found only one significant difference at the 5 % level and none at our Bonferonni adjusted 0.4 % level. Statistics of the binding event data are also presented graphically in Fig. 8-10. These figures also visually support the results from the statistical tests presented in Table 2.

All three figures present the data in the same manner. In panel A, the number of binding events is presented in one box-plot for each RyR, together with a 95 % CI of the true mean (red horizontal lines) and the expected number of binding events predicted

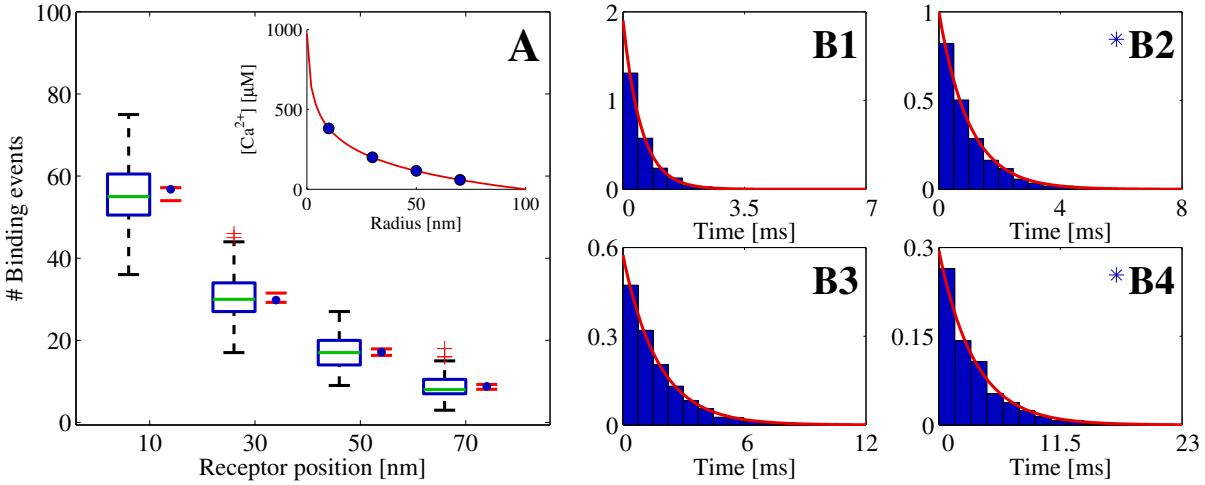

Figure 8: The figures present statistical data for binding events registered from Random Walk simulations with one open LCC, which acted as the Ca^{2+} source, situated in the centre of the cleft. The binding events are registered at four different RyRs, positioned at 10, 30, 50, and 70 nm from the centre of the cleft. Binding events are collected from 100 simulation runs. The registration started when the $[Ca^{2+}]$ had reached the steady-state. The total time simulated was 30 ms. The figure in A shows a box-plot of the number of binding events from the runs at each receptor, together with a 95 % confidence interval for the true means (red horizontal lines). The blue filled circles represent the expected number of binding events predicted by the continuous model. These values were computed on the basis of the fixed $[Ca^{2+}]$ at each receptor; see inset. In the box-plot, the green line represents the median of the data and the blue horizontal lines the limit of the upper and lower quartiles. The whiskers represent the rest of the data up to a maximum length of 1.5 times the size of the two centre quartiles. The green plus signs are outliers. The figures in B1-B4 show the inter-event intervals (IEIs) from all runs presented in scaled histogram plots, corresponding to the receptor at positions 10, 30, 50, and 70 nm from the centre of the cleft. The heights of the bars are scaled so the total area of a whole histogram equals 1. The red lines show the probability distribution of the IEI from an homogeneous Poisson distribution with a rate based on the steady-state value of the $[Ca^{2+}]$ at the receptor. The blue star indicates a significant difference, at 5 % level, between the collected IEIs and the corresponding exponential function using a Kolmogorov-Smirnov test.

by the continuous model (blue filled circles). The distributions of IEI, for each RyR, are presented in scaled histograms in the small figures of B1-B4, in each of the three figures. The heights of the bars are scaled so that the total area of the histograms equals 1. This scaling enabled us to compare the distributions of IEIs with the expected distributions from the continuous model (red lines). Fig. 8 shows the results from the first set of simulations, where the Ca^{2+} source was one LCC that was open constantly. The inset in Fig. 8 A, shows the steady-state $[Ca^{2+}]$ in the cleft from the continuous model, where the concentration at each RyR is marked by filled blue circles. Fig. 9 presents the results from the the second set of simulations, where the Ca^{2+} source was a passive influx from cytosole, which resulted in a $[Ca^{2+}]$ in the cleft that corresponds to a diastolic value of 0.1 μM. The last figure, Fig. 10 presents the results from the last set of simulations. Here, the Ca^{2+} source was three LCCs, which alternated between open and closed in the same manner during all simulations. The inset of Fig. 10 A shows the varying $[Ca^{2+}]$ from the continuous model, at the RyR positioned at 70 nm from the centre (red line), together with the shifting LCC current.

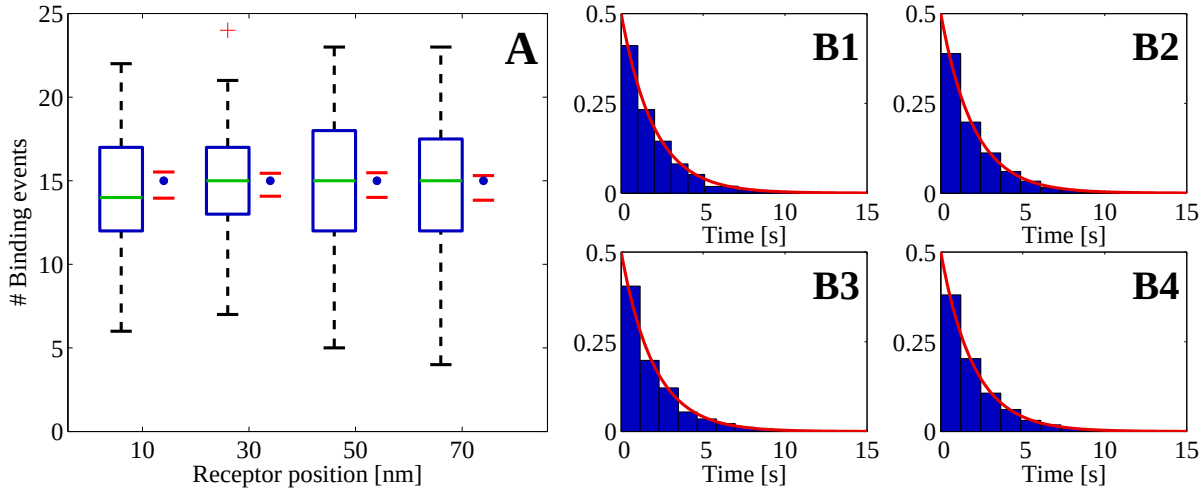

Figure 9: The figures present statistical data for binding events that are registered from Random Walk simulations. The Ca^{2+} source was passive diffusion from the cytosole during diastole, i.e., the resulting $[Ca^{2+}]$ was in average 0.1 μM. The binding events are registered at four different RyRs, positioned at 10, 30, 50, and 70 nm from the centre of the cleft. The binding events were collected from 100 simulation runs. The total time simulated was 20 s. The figure in A shows a box-plot of the number of binding events from the runs at each receptor, together with a 95 % confidence interval for the true means (red horizontal lines). The blue filled circles represent the expected number of binding events predicted by the continuous model. These values were computed on the basis of the fixed $[Ca^{2+}]$ at each receptor. For an explanation of the box-plot, see the legend of Fig. 8. The figures in B1-B4 show the inter-event intervals from all runs presented in scaled histogram plots, corresponding to the receptor at positions 10, 30, 50, and 70 nm from the centre of the cleft. For an explanation of the histogram see the legend of Fig. 8.

We observe that the number of binding events and the expected IEI distributions depend on the radial positions of the RyRs, for the first and third set of simulations, both of which are driven by a LCC current. This is not surprising, because the $[Ca^{2+}]$ are higher the closer they are to the channel. Perhaps more interesting, the RyRs in the cleft actually discriminate the $[Ca^{2+}]$ from a single Ca^{2+} source. This is important for accounting for when the cleft is treated as a single compartment with the same lumped average $[Ca^{2+}]$ [15]. There is also no over- or under- registration of binding events on a certain RyR within each set of simulations. This means that the continuous model reproduces the binding events from the RW model independently of the radial position of the RyRs.

4.3 Mean binding rate registered at a single receptor

Our goodness-of-fit tests revealed that there are no significant differences between the registration of stochastic binding events in the two models. This is not an average result, but a result that holds on the level of single runs and at the level of IEI. To acquire a better understanding of how this could be true, we examined what we called a lumped binding rate, $\bar{\lambda}^L(t)$, registered by a single RyR positioned 10 nm from the centre during a run with one constantly open LCC.

Each Ca^{2+} ion within a maximum distance of the receptor contributes, to a small

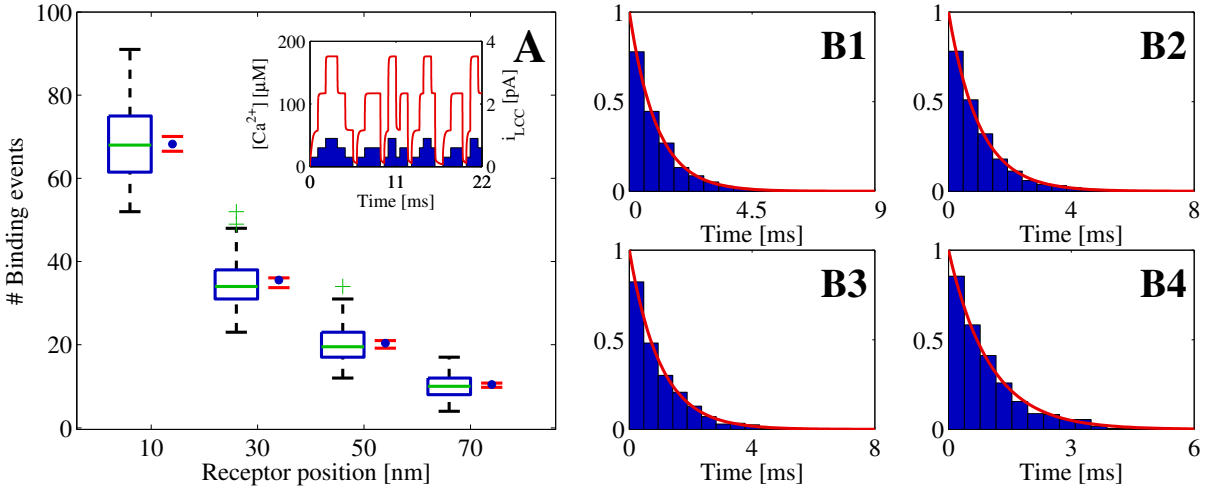

Figure 10: The figures present statistical data for binding events registered from Random Walk simulations. The Ca^{2+} source is zero to three open LCCs, situated in the centre of the cleft; see inset of A. The binding events are registered at four different RyRs, positioned at 10, 30, 50, and 70 nm from the centre of the cleft. The binding events were collected from 100 simulation runs. The total time simulated was 16 ms. The figure in A shows a box-plot of the number of binding events from the runs at each receptor, together with a 95 % confidence interval for the true means (red horizontal lines). The blue filled circles represent the expected number of binding events predicted by the varying $\left[Ca^{2+}\right]$ from the continuous model at each receptor. See the inset for the $\left[Ca^{2+}\right]$ at the RyR at 70 nm. No significant differences, at 5 % level, were detected. For an explanation of the box-plot, see the legend of Fig. 8. The figures in B1-B4 show the transformed inter-event intervals from all runs presented in scaled histogram plots, corresponding to the receptor at positions 10, 30, 50, and 70 nm from the centre of the cleft. For an explanation of the histogram, see the legend of Fig. 8.

extent, to the probability that a binding event will occur. This allows us to formulate the overall probability that a binding event will occur as a sum of small probabilities, where each is of the form $P_B^i = 1 - \mathrm{e}^{-\bar{\lambda}^i \Delta t}$; see Eq. 24. Again, given small binding probabilities, this formulation can be approximated with $P_B^i \simeq \bar{\lambda}^i \Delta t$. The resulting lumped binding probability is then $P_B^L = \Delta t \sum_i \bar{\lambda}^i = \Delta t \bar{\lambda}^L$, where $\bar{\lambda}^L$ represents the lumped binding rate.

During one simulation, we registered $\bar{\lambda}^L$ at each time step. These values are plotted against time in Fig. 11 A. The right y-axis gives the corresponding binding probabilities. The stochastic and discrete nature of the rates may be seen clearly in these chaotic data. The rate varies from time step to time step, as shown in the enlargement of the figure for $t = [0, 0.01]$ ms, shown in Fig. 11 B. The mean rate registered for the whole run was $\bar{\lambda}^L = 1.90$ ms^{-1}. In 80 % of the time steps, the rate was smaller than this value, and in 11 % of the time steps, the rate equalled zero. In only 4.1 % of the time steps was the rate larger than 10 ms^{-1} and the maximal registered rate for this run was 414 ms^{-1}. These rates seem large but the resulting binding probabilities, $P_B^L = \bar{\lambda}^L \Delta t$, were, as seen in the right y-axis, all $\ll 1$. We used the same size of time step as earlier, $\Delta t = 1.25 \times 10^{-4}$ ms. The binding probability that corresponded with the mean rate for the whole run was 2.4×10^{-4}. To be able to take the average of the binding rates over several time steps, it has to make sense to take the sum of several binding rates. This measure is justified by the small binding probabilities that each receptor experiences

every time step; see Fig. 11 A and B. The crucial issue was how the average binding rate fluctuates on a larger time scale, i.e., do the large variations in binding rates in each time step average out at a larger time scale and if so, how small can this time scale be?

The averaged binding rate did not vary much from run to run. The mean averaged rate from 100 runs was $[1.904 \pm 0.019]$ ms^{-1}. This value did not differ significantly from the constant rate from the continuous model, $\lambda_c = 1.91$ ms^{-1}, p-value $= 0.74$. This result corresponds to the failure of detecting a significant difference between the average number of binding events that was registered in the RW simulations and the number given by the continuous model (see the results of the the Student's t-tests in Table 2). The variations in the binding rate at the time scale of a whole simulation run thus averaged out and were statistically indistinguishable from the continuous constant rate.

On a smaller time scale, we would expect the averaged rate to fluctuate more. For example, the mean rate for the interval shown in Fig. 11 B, i.e., $t = [0, 0.01]$, was 2.70 ms^{-1}. This is greater than the average rate for the whole run, which was 1.90 ms^{-1}. However, the fluctuation at this time scale does not tell us much, because the expected number of binding events with this rate at this time scale is 0.027. In order to investigate the effect on the actual binding events, we have to take the average on a larger time scale. A proper scale would be the mean IEI registered in the simulation runs. This was found to be 0.52 ms; see Fig. 8 B1. We filtered the registered rate with a Gaussian filter, which act as a weighted mean over a certain time window defined by the width of the filter, σ [48]. This width was set to half the size of the mean IEI, 0.26 ms. The result is presented in Fig. 11 C, together with the constant rate from the continuous model. The filtered rate is a continuous function of time and does not vary nearly as much as the unfiltered rate in Fig. 11 A. The maximal value of the filtered signal was 2.1 ms^{-1}, the minimal was 1.7 ms^{-1}, and the standard deviation from the mean, which of course was the same as the unfiltered rate, was 0.1 ms^{-1}. This small variation explains why the IEIs of the registered binding events from the RW model were statistically indistinguishable from those of the continuous model.

4.4 Parameter sensitivity

To check the dependency of some of the parameters we have used, we made five runs in which we altered the diffusion constant, D_c, together with the maximal input current from one open LCC, $\bar{i}_{LCC}$, in the same manner as Tanskanen et al. [32] did. We scaled the D_c and $\bar{i}_{LCC}$ by factors of $[5, 2, 1, 0.5, 0.1]$ and ran 100 runs of the steady-state condition, in which one LCC was open. The spatial resolution for the registration of binding events was set to $\sigma = 5$ nm for every run. We compared the number of registered binding events with the expected number from the continuous model. The number for the latter was constant in all runs, because the concentrations at the receptors were the same under the scaling. The result is shown in Fig. 12 A. The figure shows a box-plot of the number of binding events registered at the receptor 30 nm from the centre of the cleft vs the scale on the x-axis. There are no significant differences for scale $= [5, 2, 1, 0.5]$, but for scale $= 0.1$, there is. To investigate the dependency of the parameters further, we also altered σ. We used $[5, 2, 1, 0.5]$ for σ and also did 100 runs for each different value.

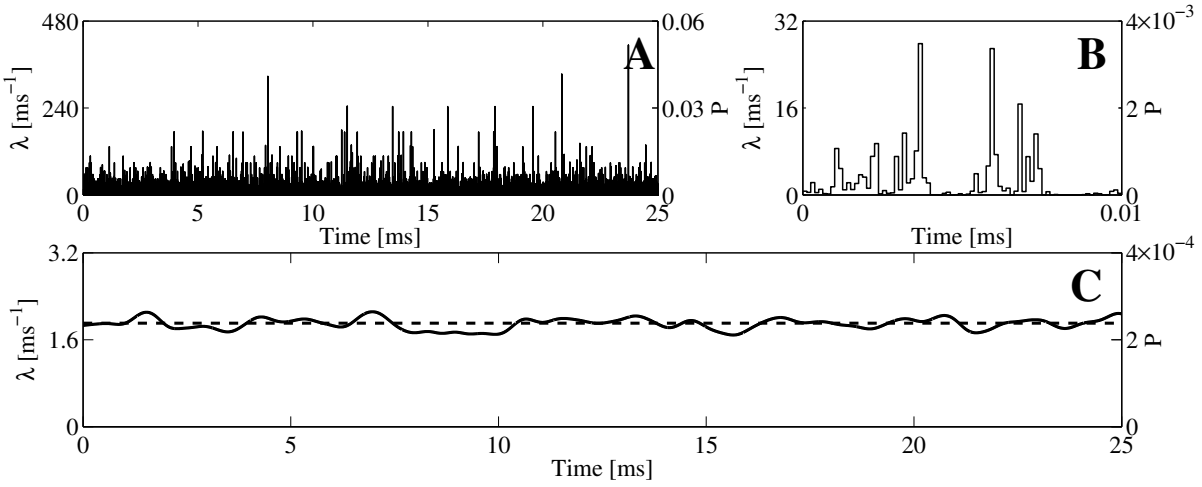

Figure 11: The figures A and B present the lumped binding rates for each time step, registered from one RyR during a single Random Walk simulation. In the simulation, one constantly open LCC channel was used and the RyR was positioned 10 nm from the centre of the cleft. The figure in B shows an enlargement of A for $t = [0, 0.01]$ ms. The mean binding rate fluctuates a lot for each time step. The figure in C shows a filtered version of the binding rate. A Gaussian kernel with $\sigma = 0.26$ ms, corresponding to the scale of the registered IEIs, was chosen for the filtering. In all figures, A- C, the corresponding binding probabilities are given by the right y-axis. For the ith time step, this quantity is computed by, $P_i = 1 - \mathrm{e}^{-\lambda_i \Delta t} \simeq \lambda_i \Delta t$.

The result is presented in a similar box plot in Fig. 12 B. Note that the leftmost data points in this figure are identical to the rightmost data points from the previous figure. From the figure, we see that the number of registered binding events falls steadily. This illustrates that the binding event registration depends, not only on physical parameters, but also on the spatial resolution of the RW method. This observation coincide with the parameters used in the dimensionless on rate Eq. 29.

One large difference between the continuous model and the RW model is that in the RW model a binding event actually leads to a removal of an ion from the cleft, in contrast to the continuous model where nothing happens. To test if this difference is crucial for the registered difference between the two models as seen in Fig. 12 B, we performed the same simulations, but without registering any binding events. Instead we registered the mean binding rate from each run and compared this with the rate predicted from the continuous model. In Fig. 12 C, the red lines represent 95 % confidence intervals of the true mean binding rate from the 100 runs. The rate predicted from the continuous model is represented by the blue filled circles. We cannot differentiate statistically between the collected mean binding rates and those of the continuous model. We also collected the mean binding rates from the simulations we did in B, in which ions were removed from the solution after they were bound. The 95 % confidence interval of the true mean for these binding rates is represented by the blue horizontal lines. Here, we see that the binding rates follow the number of registered binding events from B, and not the predicted rate from the continuous model. These results illustrate why the RW model starts to differ from the continuous model for low values of the diffusion constant together with small values of the spatial resolution.

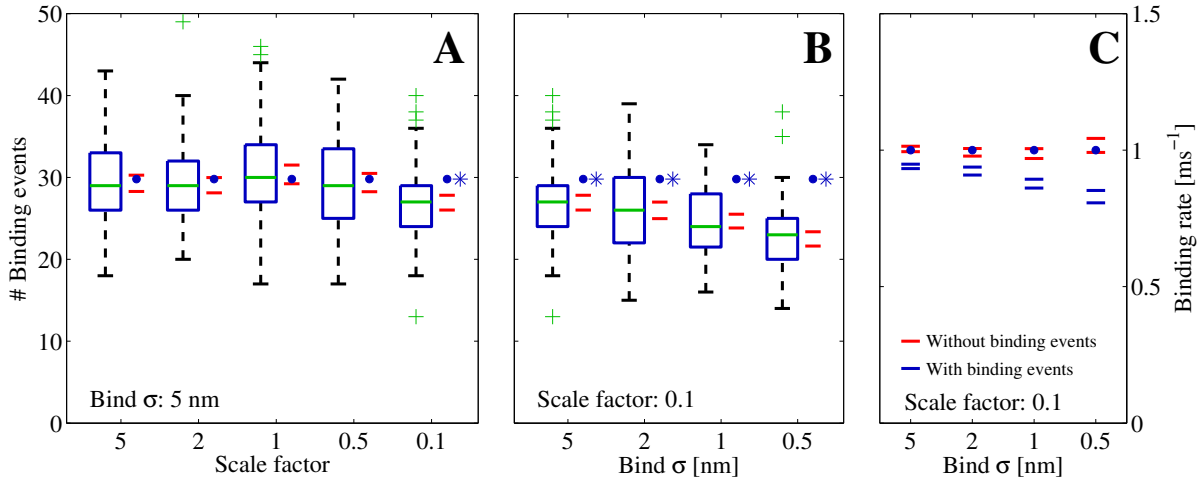

Figure 12: Figures A and B present the number of registered binding events from 100 runs each, where we altered different parameters. The data were collected from a receptor 30 nm from the centre and are represented by the box plots together with a 95 % confidence interval for the true means (red horizontal lines). The blue filled circles represent the expected number of binding events that are predicted by the continuous model. In A we scaled the number of Ca^{2+} ions that enter the cleft, i.e., $\bar{i}_{LCC}$, together with the diffusion constant D, with a factor represented by the x-axis. The spatial resolution was constant for these simulations, $\sigma = 5$ nm. The blue star denotes a statistical difference between the continuous model and the RW model for scale = 0.1. In B, we kept the scale constant at 0.1, but altered the spatial resolution (see the x-axis). Here, the difference between the RW model and the continuous model increased as the mean value of the collected binding events declined with the spatial resolution. In C, we ran the simulation 100 times. We collected the mean binding rates for each run, the receptor were exposed to. The data from each set of 100 runs are presented as 95 % confidence intervals for the true means. The blue horizontal lines represent the binding rates collected from runs in which we registered binding events, as in B. The red horizontal lines represent binding rates collected from runs in which we did not register binding events, only the rate. In these runs we could not differentiate statistically between the registered binding rates and the rates predicted from the continuous model.

As discussed above, the difference between the two models is parameter sensitive. This sensitivity can be expressed by the dimensionless on rate, k^{+*}, from Eq. 29. This value depends on the diffusion constant, D, the macroscopic on rate, k^+ and the spatial resolution, σ. For the simulations for which we registered a difference between the RW model and the continuous model, i.e., for scale = 0.1 in Fig. 12 A, $k^{+*} = 0.013$. This value indicates an upper limit for when the two models start to diverge. The spatial resolution is, in a sense, a free parameter. One could, in theory, make it as small as one likes, thus forcing a difference between the two models. Alternatively, one could make it large to smooth out a potential difference. In practice, the value of this parameter is determined by the level of spatial detail that is required in the simulation.

5 Discussion

We have compared a RW model and a continuous model of Ca^{2+} diffusion in the dyadic cleft, using the distributions of stochastic events of single Ca^{2+} ions binding to single

receptors as the measurement. We showed that for a large range of physiologically relevant parameters, there are no significant differences between the continuous model and the RW model with respect to these binding events. This is a somewhat unexpected result, considering the small number of ions included in the discrete model of $\left[Ca^{2+}\right]$ and the inherent variation in their position. In one set of simulations, the average number of Ca^{2+} ions in the cleft is 0.02, corresponding to a diastolic $\left[Ca^{2+}\right]$ of 0.1 μM. Thus, most of the time, there are no Ca^{2+} ions in the cleft. In spite of this, the corresponding constant binding rate from the continuous model can reproduce the binding events registered in the RW model.

5.1 New method for computing bi-molecular binding probabilities

We present a method for bi-molecular binding probabilities that is, to the best of our knowledge, novel. The proposed model is based on a macroscopic rate law that we use in our RW simulations. The model is analytical and gives the binding rate between two molecules exactly. To obtain this result, it is necessary only to ensure that the probability that more than one binding event per time step will be registered is small. The method is used to calculate the probability that a diffusive ligand will bind to a receptor, which can be stationary or mobile. The binding rate depends only on the on rate, k^+, the diffusion constant(s), $D_c\,(D_m)$, the size of the time step, Δt, and the distance between the two molecules, ΔS. The only parameter not known before a simulation is ΔS, and our knowledge of the other parameters allows us to precompute the binding probabilities with respect to ΔS. The method also lets us use larger time steps for the computationally expensive reaction process. We also investigated thoroughly the physical parameters for which the model is applicable.

5.2 Comparison method from hazard analysis and neuroscience

RW methods and continuous methods are models of diffusion at two different levels. They have been compared before, but here we used a quantitative goodness-of-fit measurement in the comparison study. The statistical method that we used was originally developed for the evaluation of point process models, e.g., errors in industrial processes, so-called hazard analysis [49]. The method has also recently been used in neuroscience for evaluating models in the analysis of data for neural spike trains [47]. The method is straightforward to use and could be employed in similar studies where discrete and stochastic models are compared.

5.3 Stochastic Random Walk vs deterministic continuous modelling of $\left[Ca^{2+}\right]$

A number of recent publications claim that when the number of participating particles in a volume falls, a deterministic description of concentration is invalid or does not make sense, and fully stochastic methods have to be employed [2, 6, 10, 12]. Our conclusion refines these statements.

The continuous model predicts the average number of particles involved in a process. For processes that involve a small number of particles, RW simulations show that the variation in the number of particles can be of the same magnitude or larger than this average, in a single simulation [1–3, 7]. This is a strong argument against using a continuous description of $\left[Ca^{2+}\right]$ in small volumes such as the dyadic cleft, but only if the precise position of a certain diffusive ligand is important for the physiological process. We show that this is not the case for ligands with sufficiently large diffusion constants. The important receptors in the cleft that register the Ca^{2+} signal do not switch states according to whether there are Ca^{2+} ions close to them or not, but rather according to whether there are any Ca^{2+} ions bound to them or not. These events set the right time scale for the discreteness and stochasticity of the signalling in the cleft. In our study, we showed that these events can be simulated perfectly well by a continuous model of $\left[Ca^{2+}\right]$, for a given range of model parameters. The binding events occur on a larger time scale, hiding the huge variations in the single binding rates connected to each diffusing Ca^{2+} ion in the RW simulations, as illustrated in Fig. 11 A-C. A and B show the strongly fluctuating binding rates. C shows the same rate but filtered through a Gaussian filter, with σ equalling half the mean IEI, the time scale for the binding events. Here we see that the fluctuations on the scale of IEIs are small and follow the constant rate of the continuous model. In this way, the receptor acts as an integrator of the fluctuations in the binding rates. We also show that the radial positions of the receptors are important for determining the rate of binding events at each receptor. This is important to bear in mind when, as in some models, the dyadic cleft is treated as one compartment with the same lumped $\left[Ca^{2+}\right]$ [15]. The concentration may reach a steady-state level quickly, but not all receptors sense the same $\left[Ca^{2+}\right]$ inside the cleft.

Tanskanen et al. [32] present results where their RW model shows a different result for the ECC gain, when the diffusion constant of Ca^{2+} and the influx of Ca^{2+} ions in the cleft are varied with the same amount. This difference is most probably caused by a different number of Ca^{2+} ions binding to the RyRs in the different runs. If the same had been done in a simulation in which the Ca^{2+} diffusion was modelled deterministically, a significant difference would not have been noticed, because the $\left[Ca^{2+}\right]$ at the RyR would have been the same, or more precisely, would have varied with the same mean, in each run. The authors claim that this is a "subtle but potentially significant difference in predicted macroscopic behaviour arising from the underlying stochastic simulation of Ca^{2+} motion in the dyad." We scaled the parameters in the same way as they did and we also recognized a difference, but only for the smallest value of the scaling, i.e., scale = 0.1; see Fig. 12 A. In addition, we changed the spatial resolution of the RW simulation and found that the number of binding events also depends on this parameter; see Fig. 12 B. Finally, we showed that the difference between the models depends on the fact that an ion is removed from the solution after it is bound; see Fig. 12 C. The difference become significant for large values of the dimensionless k^{+*} parameter (see Eq. 29), i.e., small values of D and σ, and large values of k^{+}. When k^{+*} is too large, a single ion's contribution to the total binding rate becomes significant and the removal of the ion after a binding event will thus alter the total rate. We found that when $k^{+*} > 0.013$, the two models registered different numbers of binding events. This is probably a conservative measure, because in our simulations we did not close a receptors

for registration after an ion was bound. This made the effect of removing an ion from the vicinity of an unbound receptor larger than it would have been if the receptor had been in a bound state. For example, when $k^{+*} = 0.026$ for the binding of Ca^{2+} ions to the stationary buffer in the transient simulation, we did not register any difference between the two models. It is important to bear in mind that the on rate k^+ for the RyRs is difficult to measure, and thus is often a free parameter. This makes the actual difference between the two models more fuzzy in real modelling, because one probably could fit the two models' macroscopic behaviour to the same data, just by using slightly different parameters.

There are limitations in the continuous model that relate to the representation of more details. Such details could, for example, be the electrostatic interaction between single molecules [50], diffusion limitations due to excluded volumes [51], or diffusion in environments with large tortuosity and with possible molecule traps [52]. However, the introduction of these extra details must be accompanied by an argument for the necessity of their inclusion. The study by Nicholson et al. [52] actually incorporates the micro-level effects into an effective diffusion constant. The authors thereby sanction the use of a macroscopic model of a micro-level phenomenon.

5.4 Limitations in our model of the dyadic cleft and Ca^{2+} dynamics

Our study of the dyadic cleft is limited, because it only examined the distribution of binding events and not the result of this event, i.e., the whole physiological signalling pathway of the Ca^{2+} induced Ca^{2+} release. However, these extra dynamics have nothing to do with diffusion. Thus, their inclusion would only introduce redundant information into our comparison study. We did include the dramatic event of a channel opening and closing during the simulation; see Fig. 10.

Our physiological model of the cleft does not incorporate all present knowledge about the cleft, e.g., the electrostatic effect on diffusion due to the charged phospholipids in the membrane [53, 54], or the obstructing effect that the large feet of the RyRs obviously have in the cleft [55]. However, the aim of the study was not to present a state-of-the-art model of the dyadic cleft, but rather to use the cleft as a well-studied model system for our comparison study between the RW model and the continuous model. The effects of these extra details can, however, be included in both models, again only introducing redundant information. The electrostatic effect of the membrane is probably the easiest to include in the continuous model, as Soeller and Cannell [21] have done in their study of Ca^{2+} diffusion in the cleft. Our cleft model is also one dimensional. Others have simulated the Ca^{2+} dynamics in the cleft using both two and three dimensions [12, 21, 31]. We could have expanded our study to both two and three dimensions and added the geometric effects of the large feet of the RyRs, but our intention was not to present the most accurate model of the cleft. The dimension we included in our study was in the radial direction, because it is in this direction that the gradient in $\left[Ca^{2+}\right]$ is largest when a channel is open.

Neither did we include the effect of crowding [56, 57] in the small and fuzzy cleft space [58]. However, a Ca^{2+} ion is much smaller than the other diffusing macromolecules that

are supposed to be in the cleft [59]. A single Ca^{2+} ion can thus probably utilize most of the volume, making the excluded volume argument regarding crowded environments [51] less forceful for Ca^{2+}.

The binding of single Ca^{2+} ions to the RyRs are not reflected in the solution of the continuous model. Each RyR should introduce a small Ca^{2+} sink to the nearby environment when an external Ca^{2+} source is turned on, and introduce a small source when the external Ca^{2+} source is turned off. Due to the large diffusion constant to Ca^{2+}, and the low affinity of the RyR, this sink is very small compared to the out-flux of Ca^{2+} ions from the cleft. We performed RW simulations in which a Ca^{2+} ion was removed from the solution when it was registered as bound to a RyR, and the same simulation where the Ca^{2+} ion was not removed. We could not distinguish between the results. This sink is also only present during a transient face of a $\left[Ca^{2+}\right]$. During the steady state, the bind flux is balanced by the unbind flux from the receptors.

6 Conclusion

The discrete and stochastic Ca^{2+} signalling in the physiological important dyadic cleft can be modelled accurately using a deterministic model of $\left[Ca^{2+}\right]$ together with a discrete and stochastic receptor model, for a certain range of parameters. Our study is the first to use the discrete binding event of single Ca^{2+} ions as a direct quantitative measure in a comparison study between a RW model and a continuous model of $\left[Ca^{2+}\right]$ in a small signalling micro domain. We also contribute a model of bi-molecular binding probabilities that can be used in RW simulations. This model is, to the best of our knowledge, novel. The model is analytical; hence, the results do not depend on the size of the time step. The study as a whole contributes both to the development of intracellular reaction-diffusion simulators [6], and to the fundamental understanding of what the models actually represent [2].

Bibliography

1. Franks, K. M. and Sejnowski, T. J. 2002. Complexity of calcium signaling in synaptic spines. Bioessays 24:1130–1144.

2. Slepchenko, B. M., Schaff, J. C., Carson, J. H., and Loew, L. M. 2002. Computational cell biology: spatiotemporal simulation of cellular events. Annu. Rev. Biophys. Biomol. Struct. 31:423–441.

3. Turner, T. E., Schnell, S., and Burrage, K. 2004. Stochastic approaches for modelling in vivo reactions. Comput. Biol. Chem. 28:165–178.

4. Bhalla, U. S. 2004. Signaling in small subcellular volumes. i. stochastic and diffusion effects on individual pathways. Biophys. J. 87:733–744.

5. Takahashi, K., Arjunan, S. N. V., and Tomita, M. 2005. Space in systems biology of signaling pathways–towards intracellular molecular crowding in silico. FEBS Lett. 579:1783–1788.

6. Lemerle, C., Ventura, B. D., and Serrano, L. 2005. Space as the final frontier in stochastic simulations of biological systems. FEBS Lett. 579:1789–1794.

7. Nelson, P. 2003. Biological Physics: Energy, Information, Life W. H. Freeman.

8. Rao, C. V., Wolf, D. M., and Arkin, A. P. 2002. Control, exploitation and tolerance of intracellular noise. Nature 420:231–237.

9. Stiles, J. R., Helden, D. V., Bartol, T. M., Salpeter, E. E., and Salpeter, M. M. 1996. Miniature endplate current rise times less than 100 microseconds from improved dual recordings can be modeled with passive acetylcholine diffusion from a synaptic vesicle. Proc. Natl. Acad. Sci. U. S. A. 93:5747–5752.

10. Stiles, J. R. and Bartol, T. M. 2001. Monte carlo methods for simulating realistic synaptic microphysiology using mcell in E. D. Schutter, editor, Computational Neuroscience: Realistic Modeling for Experimentalists pages 87–127 CRC Press.

11. Coggan, J. S., Bartol, T. M., Esquenazi, E., Stiles, J. R., Lamont, S., Martone, M. E., Berg, D. K., Ellisman, M. H., and Sejnowski, T. J. 2005. Evidence for ectopic neurotransmission at a neuronal synapse. Science 309:446–451.

12. Koh, X., Srinivasan, B., Ching, H. S., and Levchenko, A. 2006. A 3D Monte Carlo analysis of the role of dyadic space geometry in spark generation. Biophys. J. 90:1999–2014.

13. Stern, M. D., Song, L. S., Cheng, H., Sham, J. S., Yang, H. T., Boheler, K. R., and Ríos, E. 1999. Local control models of cardiac excitation-contraction coupling. a possible role for allosteric interactions between ryanodine receptors. J. Gen. Physiol. 113:469–489.

14. Greenstein, J. L. and Winslow, R. L. 2002. An integrative model of the cardiac ventricular myocyte incorporating local control of Ca^{2+} release. Biophys. J. 83:2918–2945.

15. Hinch, R., Greenstein, J. L., Tanskanen, A. J., Xu, L., and Winslow, R. L. 2004. A simplified local control model of calcium-induced calcium release in cardiac ventricular myocytes. Biophys. J. 87:3723–3736.

16. Means, S., Smith, A. J., Shepherd, J., Shadid, J., Fowler, J., Wojcikiewicz, R. J. H., Mazel, T., Smith, G. D., and Wilson, B. S. 2006. Reaction diffusion modeling of calcium dynamics with realistic er geometry. Biophys. J. 91:537–557.

17. Fabiato, A. 1983. Calcium-induced release of calcium from the cardiac sarcoplasmic reticulum. Am. J. Physiol. 245:C1–14.

18. Stern, M. D. 1992. Theory of excitation-contraction coupling in cardiac muscle. Biophys. J. 63:497–517.

19. Fawcett, D. W. and McNutt, N. S. 1969. The ultrastructure of the cat myocardium. i. ventricular papillary muscle. J. Cell Biol. 42:1–45.

20. Franzini-Armstrong, C., Protasi, F., and Ramesh, V. 1999. Shape, size, and distribution of Ca^{2+} release units and couplons in skeletal and cardiac muscles. Biophys. J. 77:1528–1539.

21. Soeller, C. and Cannell, M. B. 1997. Numerical simulation of local calcium movements during l-type calcium channel gating in the cardiac diad. Biophys. J. 73:97–111.

22. Balke, C. W. and Wier, W. G. 1991. Ryanodine does not affect calcium current in guinea pig ventricular myocytes in which Ca^{2+} is buffered. Circ. Res. 68:897–902.

23. Beuckelmann, D. J. and Wier, W. G. 1988. Mechanism of release of calcium from sarcoplasmic reticulum of guinea-pig cardiac cells. J. Physiol. 405:233–255.

24. Stern, M. D. and Cheng, H. 2004. Putting out the fire: what terminates calcium-induced calcium release in cardiac muscle? Cell Calcium 35:591–601.

25. Lukyanenko, V., Wiesner, T. F., and Gyorke, S. 1998. Termination of Ca^{2+} release during Ca^{2+} sparks in rat ventricular myocytes. J. Physiol. 507 (Pt 3):667–677.

26. Sham, J. S., Song, L. S., Chen, Y., Deng, L. H., Stern, M. D., Lakatta, E. G., and Cheng, H. 1998. Termination of Ca^{2+} release by a local inactivation of ryanodine receptors in cardiac myocytes. Proc. Natl. Acad. Sci. U. S. A. 95:15096–15101.

27. Bers, D. M. and Guo, T. 2005. Calcium signaling in cardiac ventricular myocytes. Ann. N. Y. Acad. Sci. 1047:86–98.

28. Peskoff, A., Post, J. A., and Langer, G. A. 1992. Sarcolemmal calcium binding sites in heart: II. mathematical model for diffusion of calcium released from the sarcoplasmic reticulum into the diadic region. J. Membr. Biol. 129:59–69.

29. Langer, G. A. and Peskoff, A. 1996. Calcium concentration and movement in the diadic cleft space of the cardiac ventricular cell. Biophys. J. 70:1169–1182.

30. Hinch, R., Greenstein, J. L., and Winslow, R. L. 2005. Multi-scale models of local control of calcium induced calcium release. Prog. Biophys. Mol. Biol. 90:136–150.

31. Lines, G. T., Sande, J. B., Louch, W. E., Mørk, H. K., Grøttum, P., and Sejersted, O. M. 2006. Contribution of the Na^+/Ca^{2+} exchanger to rapid Ca^{2+} release in cardiomyocytes. Biophys. J. 91:779–792.

32. Tanskanen, A. J., Greenstein, J. L., Chen, A., Sun, S. X., and Winslow, R. L. 2007. Protein geometry and placement in the cardiac dyad influence macroscopic properties of calcium-induced calcium release. Biophys. J. 92:3379–3396.

33. Crank, J. 1979. Mathematics of Diffusion Oxford University Press 2nd edition.

34. Smith, G. D., Dai, L., Miura, R. M., and Sherman, A. 2001. Asymptotic analysis of buffered calcium diffusion near a point source SIAM Journal on Applied Mathematics 61:1816–1838.

35. Langtangen, H. P. 2003. Computational Partial Differential Equations - Numerical Methods and Diffpack Programming Springer-Verlag 2nd edition.

36. Saftenku, E., Williams, A. J., and Sitsapesan, R. 2001. Markovian models of low and high activity levels of cardiac ryanodine receptors. Biophys. J. 80:2727–2741.

37. Zahradník, I., Györke, S., and Zahradníková, A. 2005. Calcium activation of ryanodine receptor channels–reconciling RyR gating models with tetrameric channel structure. J. Gen. Physiol. 126:515–527.

38. Taylor, H. E. and Karlin, S. 1998. An Introduction to Stochastic Modeling Academic Press 3rd edition.

39. Frey, E. and Kroy, K. 2005. Brownian motion: a paradigm of soft matter and biological physics. Annalen der Physik 14:20–50.

40. Miller, I. and Miller, M. 1999. John E. Freund's Mathematical Statistics Prentice Hall 6th edition.

41. Redner, S. 2001. A Guide to First-Passage Processes Cambridge University Press.

42. MATLAB (The MathWorks, Natick, MA).

43. Wang, S. Q., Song, L. S., Lakatta, E. G., and Cheng, H. 2001. Ca^{2+} signalling between single L-type Ca^{2+} channels and ryanodine receptors in heart cells. Nature 410:592–596.

44. Smith, G. D., Keizer, J. E., Stern, M. D., Lederer, W. J., and Cheng, H. 1998. A simple numerical model of calcium spark formation and detection in cardiac myocytes. Biophys. J. 75:15–32.

45. Johnson, J. D., Snyder, C., Walsh, M., and Flynn, M. 1996. Effects of myosin light chain kinase and peptides on Ca^{2+} exchange with the n- and c-terminal Ca^{2+} binding sites of calmodulin. J. Biol. Chem. 271:761–767.

46. Lehmann, E. and Romano, J. P. 2005. Testing Statistical Hypotheses Springer-Verlag New York Inc 3rd edition.

47. Brown, E. N., Barbieri, R., Ventura, V., Kass, R. E., and Frank, L. M. 2002. The time-rescaling theorem and its application to neural spike train data analysis. Neural Comput. 14:325–346.

48. Dayan, P. and Abbott, L. F. 2001. Theoretical Neuroscience: Computational and Mathematical Modeling of Neural Systems The MIT Press.

49. Karr, A. F. 1991. Point Processes and Their Statistical Inference Probability, Pure and Applied, a Series of Textbooks and Reference Books Marcel Dekker, Inc.

50. Gabdoulline, R. R. and Wade, R. C. 2002. Biomolecular diffusional association. Curr. Opin. Struct. Biol. 12:204–213.

51. Minton, A. P. 2001. The influence of macromolecular crowding and macromolecular confinement on biochemical reactions in physiological media. J. Biol. Chem. 276:10577–10580.

52. Nicholson, C., Chen, K. C., Hrabetová, S., and Tao, L. 2000. Diffusion of molecules in brain extracellular space: theory and experiment. Prog. Brain. Res. 125:129–154.

53. McLaughlin, S. G., Szabo, G., and Eisenman, G. 1971. Divalent ions and the surface potential of charged phospholipid membranes. J. Gen. Physiol. 58:667–687.

54. Langner, M., Cafiso, D., Marcelja, S., and McLaughlin, S. 1990. Electrostatics of phosphoinositide bilayer membranes. theoretical and experimental results. Biophys. J. 57:335–349.

55. Wagenknecht, T. and Radermacher, M. 1997. Ryanodine receptors: structure and macromolecular interactions. Curr. Opin. Struct. Biol. 7:258–265.

56. Ellis, R. J. 2001. Macromolecular crowding: obvious but underappreciated. Trends Biochem. Sci. 26:597–604.

57. Schnell, S. and Turner, T. E. 2004. Reaction kinetics in intracellular environments with macromolecular crowding: simulations and rate laws. Prog. Biophys. Mol. Biol. 85:235–260.

58. Lederer, W. J., Niggli, E., and Hadley, R. W. 1990. Sodium-calcium exchange in excitable cells: fuzzy space. Science 248:283.

59. Wriggers, W., Mehler, E., Pitici, F., Weinstein, H., and Schulten, K. 1998. Structure and dynamics of calmodulin in solution. Biophys. J. 74:1622–1639.

Paper II:
A coupled stochastic and deterministic model of Ca^{2+} dynamics in the dyadic cleft

A coupled stochastic and deterministic model of Ca^{2+} dynamics in the dyadic cleft

J. Hake[1]

[1] Center for Biomedical Computing, Simula Research Laboratory,
P. O. Box 134, N-1325 Lysaker, Norway

1 Introduction

From the time we are children, we are told that we should drink milk because it is an important source of calcium (Ca^{2+}), and that Ca^{2+} is vital for a strong bone structure. What we do not hear as frequently, is that Ca^{2+} is one of the most important cellular messengers in the human body [1]. In particular, Ca^{2+} controls cell death, neural signaling, secretion of different chemical substances to the body, and the focus of this chapter: the contraction of cells in the heart.

In this chapter, we will present a computational model that can be used to model Ca^{2+} dynamics in a small sub-cellular domain called the dyadic cleft. The model includes Ca^{2+} diffusion, which is described by an advection-diffusion partial differential equation, and discrete channel dynamics, which is described by stochastic Markov models. Numerical methods implemented in `PyDOLFIN` solving the partial differential equation will also be presented. In the last section, we describe a time stepping scheme that is used to solve the stochastic and deterministic models. We will also present a solver framework, `diffsim`, that implements the time stepping scheme together with the numerical methods solving the computational model described above.

2 Biological background

In a healthy heart, every heart beat originates in the sinusoidal node, where pacemaker cells trigger an electric signal. This signal is a difference in electric potential between the interior and exterior of the heart cells. These two domains are separated by the cell membrane. The difference in the electric potential between these domains is called the membrane potential. The membrane potential propagates through the whole heart using active conductances at the cell membrane. The actively propagating membrane potential is called an action potential. When an action potential arrives at a heart cell, it triggers the L-type Ca^{2+} channels (LCCs). These channels bring Ca^{2+} into the cell. Some of the Ca^{2+} diffuse over a small cleft, called the dyadic cleft, and cause further Ca^{2+} release from an intracellular Ca^{2+} storage, the sarcoplasmic reticulum (SR), through a channel called the ryanodine receptor (RyR). The Ca^{2+} ions then diffuse to the main intracellular domain of the cell, the cytosole, in which the contractile proteins are situated. The Ca^{2+} ions attach to these proteins and trigger contraction.

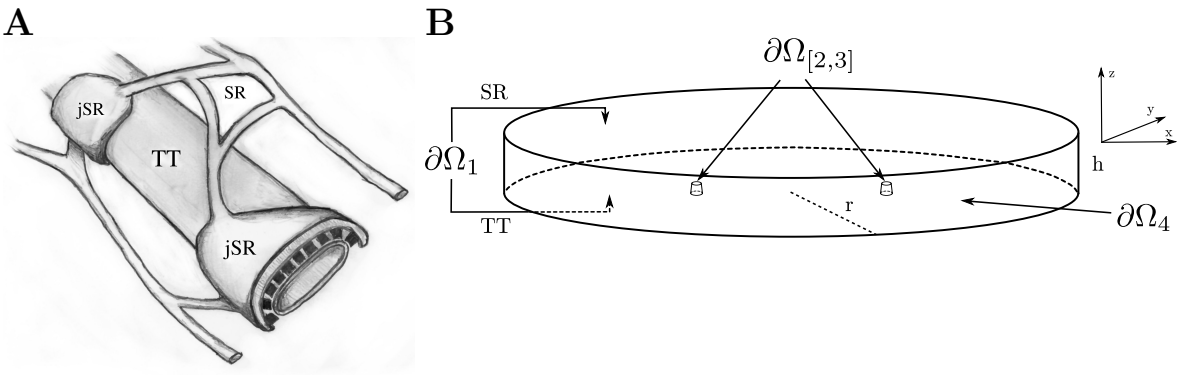

Figure 1: **A**: A diagram showing the relationship between the TT, the SR, and the jSR. The volume between the flat jSR and the TT is the dyadic cleft. The black structures in the cleft are Ryanodine receptors, which are large channel proteins. **B**: The geometry used for the dyadic cleft. The top of the disk is the cell membrane of the SR or jSR. The bottom is the cell membrane of the TT, and the circumference of the disk is the interface to the cytosole. The elevations in the TT membrane models two ions channels.

The strength of the contraction is controlled by the strength of the Ca^{2+} concentration ($[Ca^{2+}]$) in cytosole. The contraction is succeeded by a period of relaxation, which is caused by the extraction of Ca^{2+} from the intracellular space by various proteins.

This chain of events is labelled the Excitation Contraction (EC) coupling [2]. Several severe heart diseases can be related to impaired EC coupling. By broadening the knowledge of the coupling, it may be possible to develop better treatments for such diseases. Although the big picture of EC coupling is straightforward to grasp, it involves the nonlinear action of hundreds of different protein species. Computational methods have emerged as a natural complement to experimental studies to better understand the intriguing coupling. In this chapter, we focus on the initial phase of the EC coupling, the stage where Ca^{2+} flows into the cell and triggers further Ca^{2+} release.

3 Mathematical models

In this section we describe the computational model for the early phase of the EC coupling. We first present the morphology of the cleft, and how we model this in our study. Then we describe the mathematical equation for the diffusion of Ca^{2+} inside the cleft together with the boundary fluxes. Finally, we discuss the stochastic models that govern the discrete channel dynamics of the LCCs and RyRs.

Morphology

The dyadic cleft is the volume between a structure called the t-tubule (TT) and the SR. The TT is a network of pipe-like invaginations of the cell membrane that perforate the heart cell [3]. In Fig. 1 **A**, a sketch of a small part of a single TT together with a piece of SR is presented. Here we see that the junctional SR (jSR) is wrapped around the TT. The small volume between these two structures is the dyadic cleft. The space is not well defined as it is crowded with channel proteins, and its size also varies. In computational

studies, it is commonly approximated as a disk or a rectangular slab [4–7]. In this study a disk with height, $h = 12$ nm and radius, $r = 50$ nm has been used for the domain Ω, see Fig. 1 **B**. The diffusion constant of Ca^{2+} is set to $\sigma = 10^5$ nm^2 ms^{-1} [8].

Ca^{2+} Diffusion

Electro-Diffusion

We will use Fick's second law to model the diffusion of Ca^{2+} in the dyadic cleft. Close to the cell membrane, the ions are affected by an electric potential. The potential is caused by negative charges on the membrane [9, 10]. The potential attenuates fast as it is screened by the ions in the intracellular solution. We will describe the electric potential using the Gouy-Chapman method [11]. This theory introduces an advection term to the standard diffusion equation, which makes the resulting equation harder to solve. To simplify the presentation we will use a non-dimensional electric potential ψ, which is the electric potential scaled by a factor of e/kT. Here e is the electron charge, k is Boltzmann's constant and T is the temperature. We will also use a non-dimensional electric field which is given by:

$$E = -\nabla\psi. \tag{1}$$

The Ca^{2+} flux in a solution in the presence of an electric field is governed by the Nernst-Planck equation,

$$J = -\sigma\left(\nabla c - 2\,cE\right), \tag{2}$$

where $c = c(x,t)$ is the $\left[Ca^{2+}\right]$ ($x \in \Omega$ and $t \in$[0,T]), σ the diffusion constant, $E = E(x)$ the non-dimensional electric field and 2 is the valence of Ca^{2+}. Assuming conservation of mass, we arrive at the advection-diffusion equation,

$$\dot{c} = \sigma\left(\Delta c - \nabla\cdot\left(2\,cE\right)\right). \tag{3}$$

Here $\dot{c}$ is the time derivative of c.

The strength of ψ is defined by the amount of charge at the cell membrane and by the combined screening effect of all the ions in the dyadic cleft. In addition to Ca^{2+}, the intracellular solution also contains K^+, Na^+, Cl^-, and Mg^{2+}. Following the previous approach by Langner et al. [10] and Soeller and Cannell [5], these other ions will be treated as being in steady state. The cell membrane is assumed to be planar and effectively infinite. This assumption allows us to use an approximation of the electric potential in the solution,

$$\psi(z) = \psi_0\,\mathrm{e}^{-\kappa z}. \tag{4}$$

Here ψ_0 is the non-dimensional potential at the membrane, κ the inverse Debye length and z the distance from the cell membrane. We will use $\psi_0 = -2.2$ and $\kappa = 1$ nm.

Boundary fluxes

The boundary, $\partial\Omega$, is divided into 4 disjoint boundaries, $\partial\Omega_k$, for $k = 1,\ldots,4$, see Fig. 1 **B**. To each boundary we associate a flux, $J_{|\partial\Omega_k} = J_k$. The SR and TT membranes are

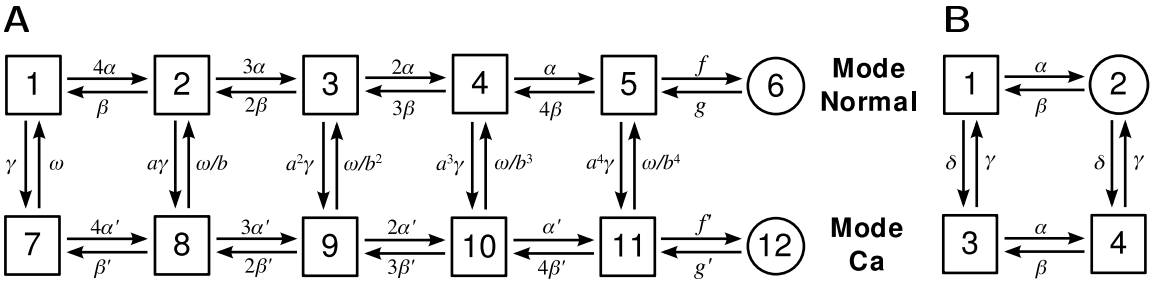

Figure 2: **A**: State diagram of the discrete LCC Markov model from Jafri et al. [13]. Each channel can be in one of the 12 states. The transitions between the states are controlled by propensities. The α, and β are voltage dependent, γ is $\left[Ca^{2+}\right]$ dependent and f, a, b, and ω are constant, see Jafri et al. [13] for further details. The channels operate in two modes: *Mode normal*, represented by the states in the upper row, and *Mode Ca*, represented the states in the lower row. In state 6 and 12 the channel is open, but state 12 is rarely entered as $f' \ll f$, effectively making *Mode Ca* an inactivated mode. **B**: State diagram of an RyR from Stern et al. [14]. The α and γ propensities are Ca^{2+} dependent, representing the activation and inactivation dependency of the cytosolic $\left[Ca^{2+}\right]$. The β and δ propensities are constant.

impermeable for ions, effectively making $\partial\Omega_1$, in Fig. 1 **B**, a no-flux boundary, giving us,

$$J_1 = 0. \tag{5}$$

We include 2 LCCs in our model. The Ca^{2+} flows into the cleft at the $\partial\Omega_{[2,3]}$ boundaries, see Fig. 1 **B**. Ca^{2+} entering these channels then diffuse to the RyRs triggering Ca^{2+} release from the SR. This additional Ca^{2+} flux will not be included in the simulations. However, the stochastic dynamics of the opening of the channel will be included. Further detailes are presented in Section 3 below. The Ca^{2+} that enters the dyadic cleft diffuses into the main compartment of cytosole, introducing a third flux. This flux is included in the model at the $\partial\Omega_3$ boundary.

The LCC is a stochastic channel that takes the state of either open or closed. When the channel is open, Ca^{2+} flows into the cleft. The dynamic that describe the stochastic behaviour is presented in Section 3 below. The current amplitude of an open LCC channel is modelled to -0.1 pA [12]. The LCC flux is then,

$$J_{[2,3]} = \begin{cases} 0 & : \text{ closed channel} \\ -\frac{i}{2FA}, & : \text{ open channel} \end{cases} \tag{6}$$

where i is the amplitude, 2 the valence of Ca^{2+}, F Faraday's constant and A the area of the channel. Note that an inward current is by convention negative.

The flux to the cytosole is modeled as a concentration dependent flux,

$$J_4 = -\sigma\frac{c - c_0}{\Delta s}, \tag{7}$$

where c is the concentration in the cleft at the boundary, c_0 the concentration in the cytosole, and Δs is an approximation of the distance to the center of the cytosole. In our model we have used $\Delta s = 50$ nm.

Stochastic models of single channels

Discrete and stochastic Markov chain models are used to describe single channel dynamics. Such models are described by a certain number of discrete states. Each channel can be in either one of these states. A transition between two states is a stochastic event. The frequency of these events are determined by the propensity functions associated with each transition. These functions, which may vary with time, characterize the probability per unit time that the corresponding transition event occurs. Each Markov model defines its own propensity functions.

L-type Ca^{2+} channel

The LCC opens when an action potential arrives at the cell. The channel inactivates when single Ca^{2+} ions bind to binding sites on the intracellular side of the channel. An LCC is composed of a complex of four transmembrane subunits. Each of these can be permissive or non-permissive. For the whole channel to be open, all four subunits need to be permissive and the channel then has to undergo a last conformational change to an opened state [15]. In this chapter we are going to use a Markov model of the LCC that incorporates a voltage dependent activation together with a Ca^{2+} dependent inactivation [13, 16]. The state diagram of this model is presented in Fig. 2 **A**. It consists of 12 states, where state 6 and 12 are the only conducting states, hence defineing the open states. The transition propensities are defined by a set of functions and constants, which are all described in Greenstein and Winslow [16].

Ryanodine Receptors

RyRs are Ca^{2+} specific channels that are gathered in clusters at the SR membrane in the dyadic cleft. These clusters can consist of several hundreds of RyRs [17, 18]. They open by single Ca^{2+} ions attaching to the receptors at the cytosolic side. We will use a modified version of a phenomenological RyR model that mimics the physiological functions of the channel [14]. The model consists of four states where only one is conducting, state 2, see Fig. 2 **B**. The α and γ propensities are Ca^{2+} dependent, representing the activation and inactivation dependency of cytosolic $\left[Ca^{2+}\right]$. The β and δ propensities are constants. For specific values for the propensities, see Stern et al. [14].

4 Numerical methods for the continuous system

In this section, we will describe the numerical methods used to solve the continuous part of the computational model of the Ca^{2+} dynamics in the dyadic cleft. We will provide `PyDOLFIN` code for each part of the presentation. The first part of the section describes the discretization of the continuous problem using a finite element method. The second part describes a method to stabilize the discretization. In this part, we also conduct a parameter study to find the optimal stabilization parameters.

```
from numpy import *
from dolfin import *

mesh = Mesh('cleft_mesh.xml.gz')

Vs = FunctionSpace(mesh, "CG", 1)
Vv = VectorFunctionSpace(mesh, "CG", 1)

v = TestFunction(Vs)
u = TrialFunction(Vs)

# Defining the electric field-function
a = Function(Vv,["0.0","0.0","phi_0*valence*kappa*sigma*exp(-kappa*x[2])"],
             {"phi_0":-2.2,"valence":2,"kappa":1,"sigma":1.e5})

# Assembly of the K, M and A matrices
K = assemble(inner(grad(u),grad(v))*dx)
M = assemble(u*v*dx)
E = assemble(-u*inner(a,grad(v))*dx)

# Collecting face markers from a file, and skip the 0 one
sub_domains = MeshFunction("uint",mesh,"cleft_mesh_face_markers.xml.gz")
unique_sub_domains = list(set(sub_domains.values()))
unique_sub_domains.remove(0)

# Assemble matrices and source vectors from exterior facets domains
domain = MeshFunction("uint",mesh,2)
F = {};f = {};tmp = K.copy(); tmp.zero()
for k in unique_sub_domains:
    domain.values()[:] = (sub_domains.values() != k)
    F[k] = assemble(u*v*ds, exterior_facet_domains = domain, \
                    tensor = tmp.copy(), reset_tensor = False)
    f[k] = assemble(v*ds, exterior_facet_domains = domain)
```

Figure 3: Python code for the assembly of the matrices and vectors from Eq. (14)-(15).

Discretization

The continuous problem is defined by Eqs. (3 -7) together with an initial condition. Given a bounded domain $\Omega \subset \mathbb{R}^3$ with the boundary, $\partial\Omega$, we want to find $c = c(x,t) \in \mathbb{R}_+$, for $x \in \Omega$ and $t \in [0,T]$, such that:

$$\begin{cases} \dot{c} &= \sigma\Delta c - \nabla\cdot(ca) & \text{in } \Omega \\ \sigma\partial_n c - ca\cdot n &= J_k & \text{on } \partial\Omega_k,\ k = 1,\ldots,4, \end{cases} \tag{8}$$

and $c(\cdot,0) = c_0(x)$. Here $a = a(x) = 2\sigma E(x)$ and J_k is the k^{th} flux at the k^{th} boundary $\partial\Omega_k$, where $\bigcup_{k=1}^4 \partial\Omega_k = \partial\Omega$, $\partial_n c = \nabla c \cdot n$, where n is the outward normal on the boundary. The J_k are given by Eqs. (5)- (7).

The continuous equations are discretized using a finite element method in space. Eq. (8) is multiplied with a proper test function v, and integrated over the spatial domain, thus obtaining:

$$\int_\Omega \dot{c}v\,dx = \int_\Omega (\sigma\Delta c - \nabla(ca))\,v\,dx. \tag{9}$$

Integration by parts, together with the boundary conditions in Eq. (8), yield:

$$\int_\Omega \dot{c}v\,dx = -\int_\Omega (\sigma\nabla c - ca)\cdot\nabla v\,dx + \sum_k \int_{\partial\Omega_k} J_k v\,ds_k. \tag{10}$$

```
# Defining the stabilization using local Peclet number
cppcode = """class Stab: public Function {
public:
  Function* field; uint _dim; double sigma;
  Stab(const FunctionSpace& V): Function(V)
    {field = 0; sigma=1.0e5;}
  void eval(double* v, const Data& data) const {
    if (!field)
      error("Attach a field function.");
    double field_norm = 0.0; double tau = 0.0;
    double h = data.cell().diameter();
    field->eval(v,data);
    for (uint i = 0;i < geometric_dimension(); ++i)
      field_norm += v[i]*v[i];
    field_norm = sqrt(field_norm);
    double PE = 0.5*field_norm * h/sigma;
    if (PE > DOLFIN_EPS)
      tau = 1/tanh(PE)-1/PE;
    for (uint i = 0;i < geometric_dimension(); ++i)
      v[i] *= 0.5*h*tau/field_norm;}};
"""
stab = Function(Vv,cppcode); stab.field = a

# Assemble the stabilization matrices
E_stab = assemble(div(a*u)*inner(stab,grad(v))*dx)
M_stab = assemble(u*inner(stab,grad(v))*dx)

# Adding them to the A and M matrices, weighted by the global tau
tau = 0.28; E.axpy(tau,E_stab); M.axpy(tau,M_stab)
```

Figure 4: Python code for the assembly of the SUPG term for the mass and advection matrices.

Consider a mesh $\mathcal{T} = \{K\}$ of simplicial elements K. Let V_h denote the space of piecewise linear polynomials, defined relative to the mesh $\mathcal{T}$. Using the backward Euler methods in time, we seek an approximation of c: $c_h \in V_h$ with nodal basis $\{\phi_i\}_{i=1}^N$. Eq. (10) can now be discretized as follows: Consider the n^{th} time step, then given c_h^n find $c_h^{n+1} \in V_h$ such that

$$\int_\Omega \frac{c_h^{n+1} - c_h^n}{\Delta t} v \, dx = -\int_\Omega \left(\sigma \nabla c_h^{n+1} - c_h^{n+1} a\right) \cdot \nabla v \, dx + \sum_k \int_{\partial\Omega} J_k v \, ds_k \quad \forall v \in V_h, \tag{11}$$

where Δt is the size of the time step. The trial function $c_h^n(x)$ is expressed as a weighted sum of basis functions,

$$c_h^n(x) = \sum_j^N C_j^n \phi_j(x). \tag{12}$$

where C_j^n are the coefficients. Due to the choice of V_h will the number of unknowns, N, coincide with the number of vertices of the mesh.

Taking test functions, $v = \phi_i$, $i \in \{1, \ldots, N\}$, gives the following algebraic system of equations in terms of the coefficients $\left\{c_i^{n+1}\right\}_{i=1}^N$.

$$\frac{1}{\Delta t} \boldsymbol{M} \left(C^{n+1} - C^n\right) = \left(-\boldsymbol{K} + \boldsymbol{E} + \sum_k \alpha^k \boldsymbol{F}^k\right) C_j^{n+1} + \sum_k c_0^k f^k. \tag{13}$$

Here $C^n \in \mathbb{R}^N$ is the vector of coefficients from the discrete solution $c_h^n(x)$, α^k and c_0^k are constant coefficients given by Eqs. (5) - (7) and

$$\begin{aligned} \boldsymbol{M}_{ij} &= \int_\Omega \phi_i \phi_j dx, & \boldsymbol{K}_{ij} &= \int_\Omega \nabla\phi_i \cdot \nabla\phi_j dx, \\ \boldsymbol{E}_{ij} &= \int_\Omega a\phi_i \cdot \nabla\phi_j dx, & \boldsymbol{F}^k_{ij} &= \int_{\partial\Omega_k} \phi_i \phi_j ds, \end{aligned} \tag{14}$$

are the entries in the $\boldsymbol{M}$, $\boldsymbol{K}$, $\boldsymbol{E}$ and $\boldsymbol{F}^k$ matrices. f^k are boundary source vectors corresponding to the k^{th} boundary. The vector elements are given by:

$$f^k_i = \int_{\partial\Omega_k} \phi_i ds. \tag{15}$$

The `PyDOLFIN` code for the assembly of the matrices and vectors in Eqs. (14)-(15) is presented in Fig. 3. Note that we define only one form for the different boundary mass matrices and boundary source vectors, `u*v*ds` and `v*ds` respectively. The `assemble` routine will assemble these forms over the 0^{th} sub-domain, see line 31 and 33 in Fig. 3. By passing sub domain specific `MeshFunction`s to the assemble routine we can assemble the correct boundary mass matrices and boundary source vectors. We collect the matrices and boundary source vectors. These are then added to form the linear system to be solved at each time step. If an LCC opens, we get contributions to the right-hand side from the source vectors. If an LCC closes, the same source vectors are removed from the right-hand side. When an LCC either opens or closes, a large flux is either added or removed from the system. To be able to resolve the sharp time gradients correctly, we need to take smaller time steps after such an event. The time step is then expanded by multiply it with a constant > 1.

The sparse linear system is solved using the `PETSc` linear algebra backend [19] in `PyDOLFIN` together with the Bi-CGSTAB iterative solver [20], and the BoomerAMG preconditioners from hypre [21]. In Fig. 5, a script is presented that solves the algebraic system from Eq. (13) together with a crude time stepping scheme for the opening and closing of the included LCC channel.

Stabilization

It turns out that the algebraic system in Eq. (13) can be numerically unstable for physiological relevant values of a. This is due to the transport term introduced by $\boldsymbol{E}_{ij}$ from Eq. (14). We have chosen to stabilize the system using the Streamline upwind Petrov-Galerkin (SUPG) method [22]. This method adds an upwind discontinuous contribution to the testfunction in the streamline direction Eq. (9),

$$v' = v + s, \text{ where } s = \tau \frac{h\tau_e}{2\|a\|} a \cdot \nabla v. \tag{16}$$

Here τ is a parameter we want to optimize (see later in this Section), $\|\cdot\|$ is the Euclidian norm in $\mathbb{R}^3$, $h = h(x)$ is the element size, and $\tau_e = \tau_e(x)$, is given by,

$$\tau_e = \coth(\text{PE}_\text{e}) - \frac{1}{\text{PE}_\text{e}}, \tag{17}$$

where $\mathrm{PE_e}$ is the element Péclet number:

$$\mathrm{PE_e} = \frac{\|a\|h}{2\sigma}. \tag{18}$$

When $\mathrm{PE_e}$ is larger than 1 the system become unstable, and oscillations is introduced.

In the 1D case, with a uniform mesh, the stabilization term defined by Eqs. (17) - (18), can give nodal exact solutions [22, 23]. Our choice of stabilization parameter is inpired by this. We have used the diameter of the sphere that circumscribes the local tetrahedron as h. This is what `DOLFIN` implements in the function `Cell.diameter()`. We recognize that other choices exist, which might give better stabilization [24]. Tezduyar and Park [25] use a length based on the size of the element in the direction of a.

The `PyDOLFIN` code that assembles the SUPG part of the problem is presented in Fig. 4. In the script, two matrices, `E_stab` and `M_stab` are assembled. Both matrices are added to the corresponding advection and mass matrices `E` and `M`, weighted by the global parameter `tau`.

A mesh with finer resolution close to the TT surface, at $z = 0$ nm, is used to resolve the steep gradient of the solution in this area. It is here the electric field is at its strongest, yielding an element Péclet number larger than 1. However the field attenuate fast: at $z = 3$ nm the field is down to 5% of the maximal amplitude, and at $z = 5$ nm, it is down to 0.7%.The mesh can thus be fairly coarse in the interior of the domain. The mesh generator `tetgen` is used to to produce meshes with the required resolution [26].

The global stabilization parameter τ, is problem dependent. To find an optimal τ, for a certain electric field and mesh, the system in Eq. (13) is solved to steady state, defined as T = 1.0 ms, using only homogeneous Neumann boundary conditions. An homogeneous concentration of $c_0 = 0.1$ μM is used as the initial condition. The numerical solution is then compared with the analytic solution of the problem. This solution is acquired by setting $J = 0$ in Eq. (2) and solving for the c, with the following result:

$$c(z) = c_b \, \mathrm{e}^{-2\psi(z)} \, . \tag{19}$$

Here ψ is given by Eq. (4), and c_b is the concentration in the bulk, i.e., where z is large. c_b was chosen such that the integral of the analytic solution was equal to $c_0 \times V$, where V is the volume of the domain.

The error of the numerical solution for different values of τ and for three different mesh resolutions are plotted in Fig. 6. The meshes are enumerated from 1-3. The error is computed using the $\mathrm{L}^2(\Omega)$ norm and is normalized by the $\mathrm{L}^2(\Omega)$ norm of the analytical solution,

$$\frac{\|c(T) - c_h^{n_T}\|_{L^2}}{\|c(T)\|_{L^2}}, \tag{20}$$

where n_T is the time step at $t = T$. As expected, we see that the mesh with the finest resolution produces the smallest error. The mesh resolutions are quantified by the number of vertices close to $z = 0$. In the legend of Fig. 6, the median of the z distance of all vertices and the total number of vertices in each mesh is presented. The three meshes were created such that the vertices closed to $z = 0$ were forced to be situated at some fixed distances from $z = 0$. Three numerical and one analytical solution for the three different meshes are plotted in Fig. 7- 9. The numerical solutions are from

```
# Model parameters
dt_min = 1.0e-10; dt = dt_min; t = 0; c0 = 0.1; tstop = 1.0
events = [0.2,tstop/2,tstop,tstop]; dt_expand = 2.0;
sigma = 1e5; ds = 50; area = pi; Faraday = 0.0965; amp = -0.1
t_channels = {1:[0.2,tstop/2], 2:[tstop/2,tstop]}

# Initialize the solution Function and the left and right hand side
u = Function(Vs); x = u.vector()
x[:] = c0#*exp(-a.valence*a.phi_0*exp(-a.kappa*mesh.coordinates()[:,-1]))
b = Vector(len(x)); A = K.copy();

solver = KrylovSolver("bicgstab","amg_hypre")
solver.parameters["relative_tolerance"] = 1e-10
solver.parameters["absolute_tolerance"] = 1e-7

plot(u, vmin=0, vmax=4000, interactive=True)
while t < tstop:
    # Initalize the left and right hand side
    A.assign(K); A *= sigma; A += E; b[:] = 0

    # Adding channel fluxes
    for c in [1,2]:
        if t >= t_channels[c][0] and t < t_channels[c][1]:
            b.axpy(-amp*1e9/(2*Faraday*area),f[c])

    # Adding cytosole flux at Omega 3
    A.axpy(sigma/ds,F[3]); b.axpy(c0*sigma/ds,f[3])

    # Applying the Backward Euler time discretization
    A *= dt; b *= dt; b += M*x; A += M

    solver.solve(A,x,b)
    t += dt; print "Ca Concentration solved for t:",t

    # Handle the next time step
    if t == events[0]:
        dt = dt_min; events.pop(0)
    elif t + dt*dt_expand > events[0]:
        dt = events[0] - t
    else:
        dt *= dt_expand

    plot(u, vmin=0, vmax=4000)

plot(u, vmin=0, vmax=4000, interactive=True)
```

Figure 5: Python code for solving the system in Eq. (13), using the assembled matrices from the two former code examples from Fig. 3- 4.

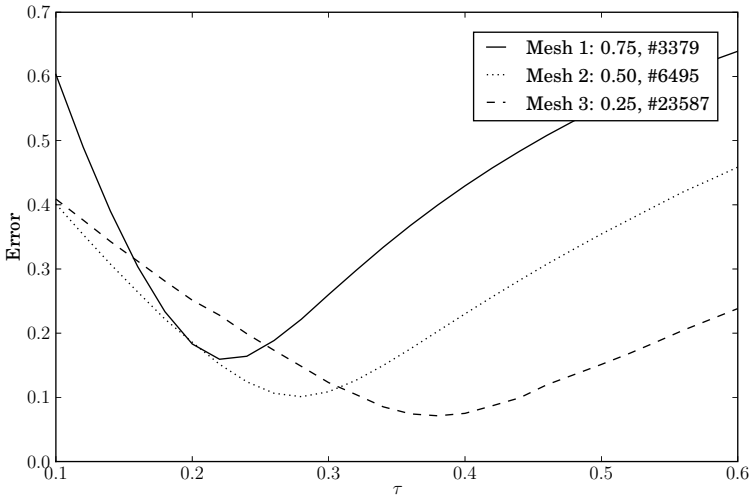

Figure 6: The figure shows a plot of the error versus the stabilization parameter τ for 3 different mesh resolutions. The mesh resolutions are given by the median of the z distance of all vertices and the total number of vertices in the mesh, see legend. We see that the minimal values of the error for the three meshes, occur at three different τ: 0.22, 0.28, and 0.38.

simulations using three different τ: 0.1, 0.6 and the L^2-optimal τ, see Fig. 6. The traces in the figures are from the discrete solution $c_h^{n_T}$, evaluated on the straight line between the spatial points p_0=(0,0,0) and p_1=(0,0,12).

In Fig. 7 the traces from mesh 1 is plotted. Here we see that the numerical solutions are quite poor for some of the τ. The solution with $\tau = 0.10$ is obviously not correct, as it produces negative concentrations. The solution with $\tau = 0.60$ seems more correct but it undershoots the analytic solution at $z = 0$ with ~ 1.7 μM. The solution with $\tau = 0.22$ is the L^2-optimal solution for mesh 1, and approximates the analytic solution at $z = 0$ well.

In Fig. 8 the traces from mesh 2 is presented in two plots. The left plot shows the traces for $z < 1.5$ nm, and the right shows the traces for $z > 10.5$ nm. In the left plot we see the same tendency as in Fig. 7, an overshoot of the solution with $\tau = 0.10$ and an undershoot of the solution with $\tau = 0.60$. The L^2-optimal solution, the one with $\tau = 0.28$, overshoots the analytic solution for the shown interval in the left plot, but undershoots for the rest of the trace.

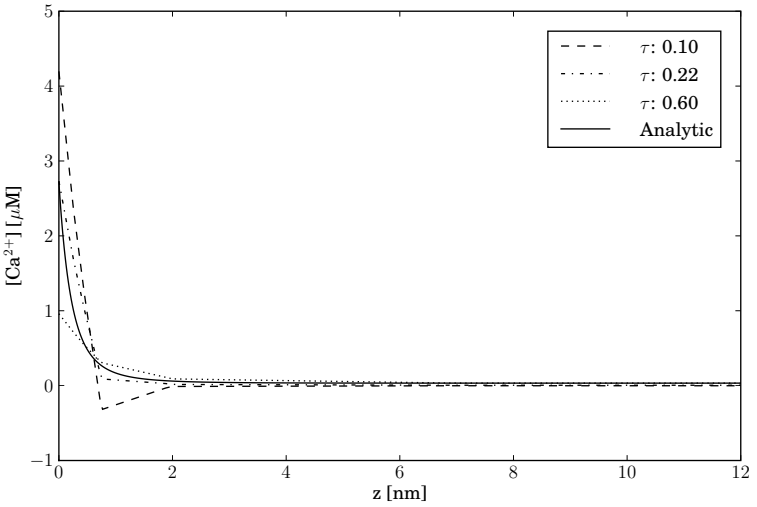

Figure 7: The figure shows the concentration traces of the numerical solutions from Mesh 1, see legend of Fig. 6, for three different τ together with the analytic solution. The solutions were picked from a line going between the points (0,0,0) and (0,0,12). We see that the solution with $\tau = 0.10$ oscillates. The solution with $\tau = 0.22$ was the solution with smallest global error for this mesh, see Fig 6, and the solution with $\tau = 0.60$ undershoots the analytic solution at $z = 0$nm with ~ 1.7 μM.

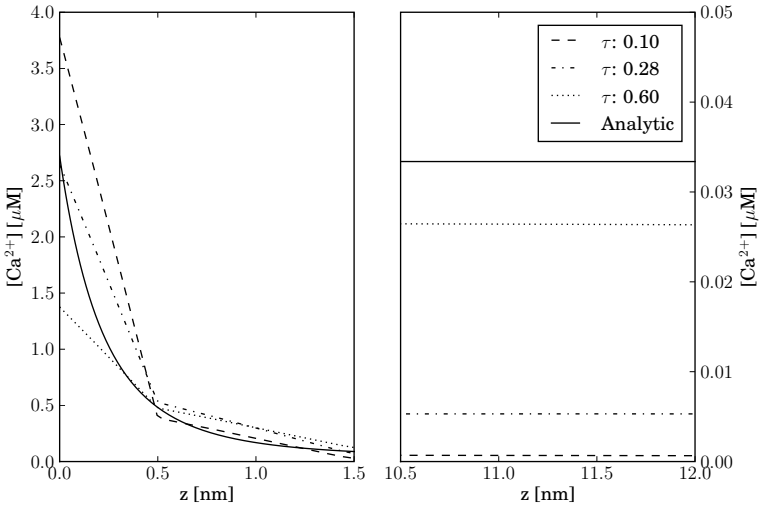

Figure 8: The figures show the concentration traces of the numerical solutions from Mesh 2, see legend of Fig. 6, for three different τ together with the analytic solution. The solution traces in the two panels are picked from a line going between the spatial points (0,0,0) and (0,0,1.5), for the left panel, and between spatial points (0,0,10.5) and (0,0,12), for the right panel. We see from both panels that the solution with $\tau = 0.10$ give the poorest solution. The solution with $\tau = 0.28$ was the solution with smallest global error for this mesh, see Fig 6, and this is reflected in the reasonable good fit seen in the left panel, especially at $z = 0$nm. The solution with $\tau = 0.60$ undershoots the analytic solution at $z = 0$ with ~ 1.2 μM. From the right panel we see that all numerical solutions undershoot at $z = 15$nm, and that the trace with $\tau = 0.60$ comes the closest to the analytic solution.

In the last figure, Fig. 9, traces from mesh 3 is presented. The results is also here presented in two plots, corresponding to the same z interval as in Fig. 8. We see that the solution with $\tau = 0.10$ is not good in either plots. In the left plot it clearly overshoots the analytic solution for most of the interval, and then stays at a lower level than the analytic solution for the rest of the interval. The solution with $\tau = 0.60$ is much better here than in the two previous plots. It undershoots the analytic solution at $z = 0$ but stays closer to it for the rest of the interval than the L^2-optimal solution. The L^2 norm penalize larger distances between two traces, i.e., weighting the error close to $z = 0$ more than the rest. The optimal solution measured in the Max norm is given when $\tau = 50$, result not shown.

These results tell us that it is difficult to obtain accurate numerical solution for the advection-diffusion problem presented in Eq. (8). Using a finer mesh close to $z = 0$ could help, but it will create a larger algebraic system. It is interesting to notice that the L^2 optimal solutions is better close to $z = 0$, than other solutions and the solution for the largest τ is better than other for $z > 2$ nm. For a modeller, these constraints are important to know about; the solution at $z = 0$ and $z = 12$ nm are the most important, as Ca^{2+} interact with other proteins at these points.

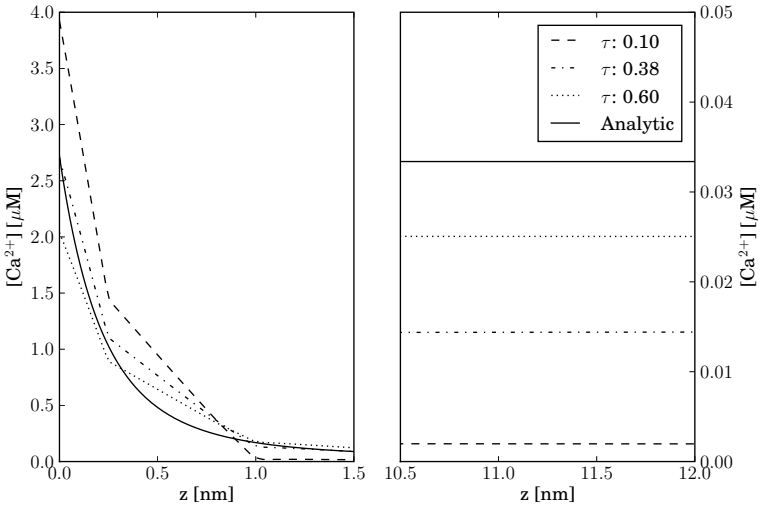

Figure 9: The figures shows the concentration traces of the numerical solutions from Mesh 3, see legend of Fig. 6, for three different τ together with the analytic solution. The traces in the two panels were picked from the same lines as the one in Fig. 8. Again we see from both panels that the solution with $\tau = 0.10$ give the poorest solution. The solution with $\tau = 0.38$ was the solution with smallest global error for this mesh, see Fig 6, and this is reflected in the good fit seen in the left panel, especially at $z = 0$nm. The solution with $\tau = 0.60$ undershoots the analytic solution at $z = 0$ with ~ 0.7 μM. From the right panel we see that all numerical solutions undershoot at $z = 15$nm, and the trace with $\tau = 0.60$ also here comes closest the analytic solution.

5 `diffsim` an event driven simulator

In the scripts in Fig. 3- 5, we show how a simple continuous solver can be built with `PyDOLFIN`. By preassembling the matrices from Eq. (14) a flexible system for adding and removing boundary fluxes corresponding to the state of the channels can be constructed. The script in Fig.5 uses fixed time points for the channel state transitions. At these time points we minimize Δt, so we can resolve the sharp time gradient. In between the channel transitions we expand Δt. This simplistic time stepping scheme is sufficient to solve the presented example. However it would be difficult to expand it to also incorporate the time stepping involved with the solution of stochastic Markov models, and other discrete variables. For such scenarios, an event driven simulator called `diffsim` has been developed. In the last subsections in this chapter, the algorithm underlying the time stepping scheme in `diffsim` will be presented. An example of how one can use `diffsim` to describe and solve a model of the Ca^{2+} dynamics in the dyadic cleft will also be demonstrated. The `diffsim` software can freely be downloaded from URL:`http://www.fenics.org/wiki/FEniCS_Apps`.

Stochastic system

The stochastic evolution of the Markov chain models presented in Section 3 is determined by a modified Gillespie method [27], which resembles the one presented in Rüdiger et al. [28]. Here we will not go into detail of the actual method, but rather explain the part of the method that has importance for the overall time stepping algorithm.

```
while not stop_sim:
    # The next event
    event = min(discrete_objects)
    dt = event.next_time()

    # Step the event and check result
    while not event.step():
        event = min(discrete_objects)
        dt = event.next_time()

    # Update the other discrete objects with dt
    for obj in discrete_objects:
        obj.update_time(dt)

    # Solve the continuous equation
    ca_field.solve(dt)
    ca_field.send()

    # Distribute the event
    event.send()
```

Figure 10: Python-like pseudo code for the time stepping algorithm used in our simulator

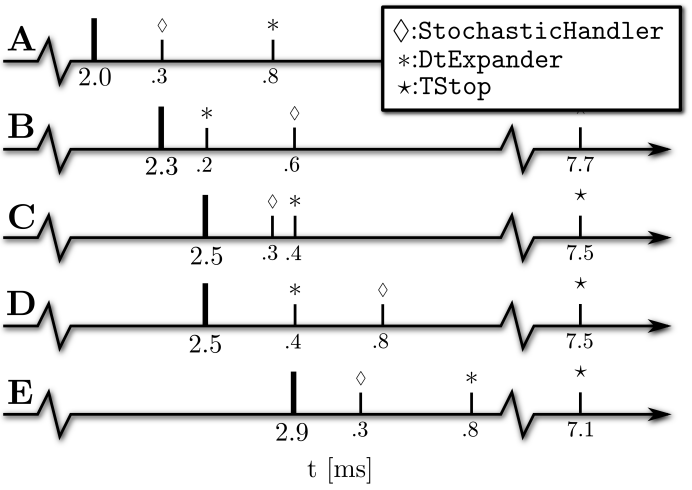

Figure 11: Diagram for the time stepping algorithm using 3 discrete objects: `DtExpander`, `StochasticHandler`, `TStop`. The values below the small ticks, corresponds to the time to the next event for each of the discrete objects. This time is measured from the last realized event, which is denoted by the thicker tick. In **A** we have realized a time event at t=2.0 ms. The next event to be realized is a stochastic transition, the one with smallest value below the ticks. In **B** this event is realized, and the `StochasticHandler` now show a new next event time. The event is a channel transition forcing the dt, controlled by the `DtExpander`, to be minimized. `DtExpander` now has the smallest next event time, and is realized in **C**. The channel transition that was realised in **B** raised the $\left[Ca^{2+}\right]$ in the cleft which in turn increase the Ca^{2+} dependent propensity functions in the included Markov models. The time to next event time of the `StochasticHandler` has therefore been updated, and moved forward in **C**. Also note that the `DtExpander` has expanded its next event time. In **D** the stochastic transition is realized and updated with a new next event time, but it is ignored as it is not a channel transition. The smallest time step is now the `DtExpander`, and this is realized in **E**. In this example we do not realize the `TStop` event as it is too far away.

The solution of the included stochastic Markov chain models is stored in a state vector, `S`. Each element in `S` corresponds to one Markov model and the value reflects which state each model is in. The transitions between these states are modelled stochastically and are computed using the modified Gillespie method. This method basically gives us which of the states in `S` changes to what state and when. It is not all such state transitions that are relevant for the continuous system. A transition between two closed states in the LCC model will not have any impact on the boundary fluxes, and can be ignored. Only transitions that either open or close a channel (channel transitions), will be recognized. The modified Gillespie method assumes that any continuous variables that a certain propensity function depends on, are constant during a time step. The error of this assumption is reduced by taking smaller time steps right after a channel transition, as the continuous field is indeed changing dramatically during this time period.

Time stepping algorithm

To simplify the presentation of the time stepping algorithm we only consider one continuous variable, this could for example be the Ca^{2+} field. The framework presented here can be expanded to also handle several continuous variables. We define a base class called `DiscreteObject`, which defines the interface for all discrete objects. A key function of a discrete object is to know when its *next event* is due at. The `DiscreteObject` that has the smallest next event time, gets to define the size of the next Δt. In `Python` this is easily done by making the `DiscreteObject`s sortable with respect to their next event time. All `DiscreteObject`s is then collected in a list, `discrete_objects` see Fig. 10. The `DiscreteObject` with the smallest next event time is then just `min(discrete_objects)`.

An event from a `DiscreteObject` that does not have an impact on the continuous solution will be ignored for example a Markov chain model transition that is not a channel transition. A transition needs to be realized before we can tell if it is a channel transition or not. This is done by *stepping* the `DiscreteObject`, i.e., calling the object's `step()` method. If the method returns `False`, it will not affect the Ca^{2+} field, and we enter the while loop, and a new `DiscreteObject` is picked, see Fig. 10. If the object returns `True` when stepped, we exit the loop and continue. Next, we have to update the other discrete objects with the chosen Δt, solve for the Ca^{2+} field, broadcast the solution and last but not least execute the discrete event that is scheduled to happen at Δt.

In Fig. 11 we show an example of a possible realization of this algorithm. The example starts at t=2ms at the top-most timeline represented by **A**, and it includes three different types of `DiscreteObjects`: `i`) `DtExpander`, `ii`) `StochasticHandler`, and `iii`) `TStop`. See the figure legend for more details.

`diffsim`: an example

`diffsim` is a versatile event driven simulator that incorporates the time stepping algorithm presented in the previous section together with the infrastructure to solve

```
from diffsim import *
from diffsim.dyadiccleft import *
from numpy import exp, fromfile

# Model parameters
c0_bulk = 0.1; D_Ca = 1.e5; Ds_cyt = 50; phi0 = -2.2; tau = 0.28
AP_offset = 0.1; dV = 0.5, ryr_scale = 100; end_sim_when_opend = True

# Setting boundary markers
LCC_markers = range(10,14); RyR_markers = range(100,104); Cyt_marker = 3

# Add a diffusion domain
domain = DiffusionDomain("Dyadic_cleft","cleft_mesh_with_RyR.xml.gz")
c0_vec = c0_bulk*exp(-VALENCE[Ca]*phi0*exp(-domain.mesh().coordinates()[:,-1]))

# Add the ligand with fluxes
ligand = DiffusiveLigand(domain.name(),Ca,c0_vec,D_Ca)
field  = StaticField("Bi_lipid_field",domain.name())
Ca_cyt = CytosolicStaticFieldFlux(field,Ca,Cyt_marker,c0_bulk,Ds_cyt)

# Adding channels with Markov models
for m in LCC_markers:
    LCCVoltageDepFlux(domain.name(), m, activator=LCCMarkovModel_Greenstein)
for m in RyR_markers:
    RyRMarkovModel_Stern("RyR_%d"%m, m, end_sim_when_opend)

# Adding a dynamic voltage clamp that drives the LCC Markov model
AP_time = fromfile('AP_time_steps.txt',sep='\n')
dvc = DynamicVoltageClamp(AP_time,fromfile('AP.txt',sep='\n'),AP_offset,dV)

# Get and set parameters
params = get_params()

params.io.save_data = True
params.Bi_lipid_field.tau = tau
params.time.tstop = AP_time[-1] + AP_offset
params.RyRMarkovChain_Stern.scale = ryr_scale

info(str(params))

# Run 10  simulations
data = run_sim(10,"Dyadic_cleft_with_4_RyR_scale")
mean_release_latency = mean([ run["tstop"] for run in data["time"]])
```

Figure 12: An example of how `diffsim` can be used to simulate the time to RyR release latency, from a small dyad who's domain is defined by the mesh in the file `cleft_mesh_with_RyR.xml.gz`.

models with one or more diffusional domains, defined by a computational mesh. Each such domain can have several diffusive ligands. Custom fluxes can easily be included through the framework. The sub module `dyadiccleft` implements some published Markov models that can be used to simulate the stochastic behaviour of a dyad and some convenient boundary fluxes. It also implements the field flux from the lipid bi-layer discussed in Section 3. In Fig. 12 a runnable script is presented, which simulates the time to release, also called the latency, for a dyad. The two Markov models that is presented in Section 3 are here used to model the stochastic dynamics of the RyRs and the LCCs. The simulation is driven by a so called dynamic voltage clamp. The data that defining the voltage clamp is read from a file using utilities from the `NumPy Python` packages.

6 Discussion

We have presented a computational model of the Ca^{2+} dynamics of the dyadic cleft in heart cells. It consists of a coupled stochastic and continuous system. We have showed how one can use `PyDOLFIN` to discretise and solve the continuous system using a finite element method. The continuous system is an advection-diffusion equation that produce unstable discretizations. We investigate how one can use the streamline upwind/Petrov-Galerkin method to stabilize the discretized system. We use three different meshes and find an L^2-optimal global stabilization parameters τ for each mesh.

We do not present a solver for the stochastic system. However we outline a time stepping scheme that can be used to couple the stochastic solver with the presented solver for the continuous system. A simulator `diffsim` is briefly introduced, which implements the presented time stepping scheme together with the presented solver for the continuous system.

Bibliography

1. Alberts, B., Bray, D., Lewis, J., Raff, M., Roberts, K., and Watson, J. 2002. Molecular Biology of the Cell Garland 4th edition.

2. Bers, D. M. 2001. Excitation-Contraction Coupling and Cardiac Contractile Force Kluwert Academic, Dordrecht, The Netherlands 2nd edition.

3. Soeller, C. and Cannell, M. B. 1999. Examination of the transverse tubular system in living cardiac rat myocytes by 2-photon microscopy and digital image-processing techniques. Circ. Res. 84:266–75.

4. Peskoff, A., Post, J. A., and Langer, G. A. 1992. Sarcolemmal calcium binding sites in heart: II. mathematical model for diffusion of calcium released from the sarcoplasmic reticulum into the diadic region. J. Membr. Biol. 129:59–69.

5. Soeller, C. and Cannell, M. B. 1997. Numerical simulation of local calcium movements during l-type calcium channel gating in the cardiac diad. Biophys. J. 73:97–111.

6. Koh, X., Srinivasan, B., Ching, H. S., and Levchenko, A. 2006. A 3D Monte Carlo analysis of the role of dyadic space geometry in spark generation. Biophys. J. 90:1999–2014.

7. Tanskanen, A. J., Greenstein, J. L., Chen, A., Sun, S. X., and Winslow, R. L. 2007. Protein geometry and placement in the cardiac dyad influence macroscopic properties of calcium-induced calcium release. Biophys. J. 92:3379–3396.

8. Langer, G. A. and Peskoff, A. 1996. Calcium concentration and movement in the diadic cleft space of the cardiac ventricular cell. Biophys. J. 70:1169–1182.

9. McLaughlin, S. G., Szabo, G., and Eisenman, G. 1971. Divalent ions and the surface potential of charged phospholipid membranes. J. Gen. Physiol. 58:667–687.

10. Langner, M., Cafiso, D., Marcelja, S., and McLaughlin, S. 1990. Electrostatics of phosphoinositide bilayer membranes. theoretical and experimental results. Biophys. J. 57:335–349.

11. Grahame, D. C. 1947. The electrical double layer and the theory of electrocapillarity. Chem Rev 41:441–501.

12. Guia, A., Stern, M. D., Lakatta, E. G., and Josephson, I. R. 2001. Ion concentration-dependence of rat cardiac unitary l-type calcium channel conductance. Biophys J 80:2742–2750.

13. Jafri, M. S., Rice, J. J., and Winslow, R. L. 1998. Cardiac Ca^{2+} dynamics: the roles of ryanodine receptor adaptation and sarcoplasmic reticulum load. Biophys. J. 74:1149–68.

14. Stern, M. D., Song, L. S., Cheng, H., Sham, J. S., Yang, H. T., Boheler, K. R., and Ríos, E. 1999. Local control models of cardiac excitation-contraction coupling. a possible role for allosteric interactions between ryanodine receptors. J. Gen. Physiol. 113:469–489.

15. Hille, B. 2001. Ion Channels of Excitable Membranes Sinauer, Sunderland, MA.

16. Greenstein, J. L. and Winslow, R. L. 2002. An integrative model of the cardiac ventricular myocyte incorporating local control of Ca^{2+} release. Biophys. J. 83:2918–2945.

17. Beuckelmann, D. J. and Wier, W. G. 1988. Mechanism of release of calcium from sarcoplasmic reticulum of guinea-pig cardiac cells. J. Physiol. 405:233–255.

18. Franzini-Armstrong, C., Protasi, F., and Ramesh, V. 1999. Shape, size, and distribution of Ca^{2+} release units and couplons in skeletal and cardiac muscles. Biophys. J. 77:1528–1539.

19. Balay, S., Buschelman, K., Gropp, W. D., Kaushik, D., Knepley, M. G., McInnes, L. C., Smith, B. F., and Zhang, H. 2001. PETSc Web page URL:`http://www.mcs.anl.gov/petsc`.

20. van der Vorst, H. A. 1992. Bi-CGSTAB: A fast and smoothly converging variant of bi-cg for the solution of nonsymmetric linear systems SIAM Journal on Scientific and Statistical Computing 13:631–644.

21. Falgout, R. D. and Yang, U. M. 2002. hypre: A library of high performance preconditioners in ICCS '02: Proceedings of the International Conference on Computational Science-Part III pages 632–641 Springer-Verlag, London, UK.

22. Brooks, A. N. and Hughes, T. J. R. 1982. Streamline upwind/petrov-galerkin formulations for convection dominated flows with particular emphasis on the incompressible navier-stokes equations Computer Methods in Applied Mechanics and Engineering 32:199–259.

23. Christie, I., Griffiths, D., Mitchell, A., and Zienkiewicz, O. 1976. Finite element methods for second order differential equations with significant first derivatives International Journal for Numerical Methods in Engineering 10:1389–1396.

24. John, V. and Knobloch, P. 2007. On spurious oscillations at layers diminishing (sold) methods for convection-diffusion equations: Part i - a review Computer Methods in Applied Mechanics and Engineering 196:2197 – 2215.

25. Tezduyar, T. and Park, Y. 1986. Discontinuity-capturing finite element formulations for nonlinear convection-diffusion-reaction equations. Comp. Methods Appl. Mech. Eng. 59:307–325.

26. Si, H. 2007. TetGen. a quality tetrahedral mesh generator and three-dimensional delaunay triangulator. URL:`http://tetgen.berlios.de`.

27. Gillespie, D. T. 1977. Exact stochastic simulation of coupled chemical reactions J. Phys. Chem. 81:2340–2361.

28. Rüdiger, S., Shuai, J. W., Huisinga, W., Nagaiah, C., Warnecke, G., Parker, I., and Falcke, M. 2007. Hybrid stochastic and deterministic simulations of calcium blips. Biophys. J. 93:1847–1857.

Paper III:
Mechanisms underlying delayed and dyssynchronous Ca^{2+} release in failing cardiomyocytes examined by computer modeling

Mechanisms underlying delayed and dyssynchronous Ca^{2+} release in failing cardiomyocytes examined by computer modeling

J. Hake[1], W. E. Louch[2,3], O. M. Sejersted[2,3], G. T. Lines[1,4]

[1] Center for Biomedical Computing, Simula Research Laboratory,
P. O. Box 134, N-1325 Lysaker, Norway

[2] Institute for Experimental Medical Research
Ullevaal University Hospital, Oslo, Norway

[3] Center for Heart Failure Research
University of Oslo, Oslo, Norway

[4] Department of Informatics, University of Oslo,
P. O. Box 1080 Blindern, N-0316 Oslo, Norway

Abstract:

Ca^{2+} induced Ca^{2+} release (CICR) in cardiomyocytes is controlled in the signalling micro domain of the dyadic cleft. During the action potential, the L-type Ca^{2+} channel (LCC) opens, allowing Ca^{2+} entry into the cleft. This Ca^{2+} then triggers further Ca^{2+} release from the sarcoplasmic reticulum, by activating the ryanodine receptors (RyRs). Large gradients of $\left[Ca^{2+}\right]$ are rapidly established in response to the open LCCs, which are highly dependent on locality and source strength. These gradients determine the time required for the RyRs to open after an action potential has arrived at a cardiomyocyte. Ca^{2+} release becomes delayed and dyssynchronous during heart failure. We used a detailed computational model of the dyadic cleft to investigate potential mechanisms contributing to the altered Ca release pattern. We found that alterations in action potential configuration alone slowed the average activation time by 2 ms and increased the dyssynchrony, here represented by the standard deviation in activation time. Heart-failure alters the structures that defines the dyadic cleft. We modelled potential perturbations to the dyadic cleft by increasing the height. A height increase of 3 nm slowed the average activation time by an additional 5 ms and further increased the dyssynchrony. We also employed our model to investigate whether a lone Na^+/Ca^{2+} exchanger (NCX) working in reverse mode could trigger CICR. The NCX was co-localized with a Na^+ channel, so that local elevations in $\left[Na^+\right]$ could be sensed by the channel. We found that Ca^{2+} from a single NCX could not trigger CICR.

1 Introduction

The process that links electric excitation of the cell membrane to contraction of a cardiomyocyte is known as the excitation-contraction coupling (ECC) [1]. Depolarization of the cell membrane during the action potential (AP) evokes a transient rise in cytosolic Ca^{2+}, the Ca^{2+} transient. The major part of this transient is derived from Ca^{2+} release from the sarcoplasmic reticulum (SR), via ryanodine receptors (RyR). The Ca^{2+} release is triggered by external Ca^{2+} entering mainly through the L-type Ca^{2+}-channel (LCC). The process is known as Ca^{2+}-induced Ca^{2+} release (CICR) [2]. CICR is locally controlled in the dyad where the RyRs face the LCCs only separated by the narrow ($\sim$ 12 nm) dyadic cleft. A dyad can be seen as a functional unit also called a couplon comprising hundreds of RyRs and tens of LCCs [3]. These are predominantly localized in the t-tubule (TT), which are invaginations of the surface membrane into the interior of the cardiomyocyte. A single Ca^{2+} release event in a couplon is called a Ca^{2+} spark, and the concerted appearance of thousands of sparks constitutes the Ca^{2+} transient [4]. The spatial synchrony of the Ca^{2+} sparks is assured by the regularly organized TT network. Disruptions in the TT structure can disturb ion homeostasis in the dyadic cleft, and thus lead to altered control of contractility. Louch et al. [5] observed a progressive reorganization of the TT during heart failure (HF). This resulted in a spatially dyssynchronous Ca^{2+} transient characterized by regions of delayed Ca^{2+} release. The delayed release regions occurred in areas of the cell that lacked TT network and therefore also LCCs. Thus, Ca^{2+} release in these regions was triggered only after diffusion of Ca^{2+} from neighboring dyads. The authors hypothesized that T-tubule disruption might also have contributed to an observed delay in Ca^{2+} release [5]. However, others have suggested that reduced Ca^{2+} release synchrony results from altered action potential configuration during HF [6].

Previously we have suggested that the Na^+/Ca^{2+} exchanger (NCX) can shorter latency and better synchrony [7]. The NCX is a bi-dircetional ion exchanger. The rate and direction of this current are controlled by the membrane potential, and the intra and extra-cellular concentrations of both Ca^{2+} and Na^+ [8]. In forward mode, the NCX transports Ca^{2+} out of the cell and Na^+ into the cell. This mode sets the Ca^{2+} content of SR, as it competes with the SR Ca^{2+} ATPase (SERCA) pump, in extracting Ca^{2+} from the cytosol. In a brief time window, when the AP reaches above the reversal potential of the NCX, the exchanger will work in reverse mode, letting Ca^{2+} in to the cell. This Ca^{2+} entry may contribute to CICR and to the overall Ca^{2+} transient [1, 7]. The significance of this contribution is currently under debate [9–11]. In a recent review Bers [12] states that the main trigger of CICR is the LCC. However, Bers describes three possible ways the NCX can modulate the process: *i*) The Na^+-channel (NaC) elevates sub-sarcolemma $\left[Na^+\right]$ which enhances reverse mode function of nearby NCXs. *ii*) During the early peak of an AP the NCX can immediately bring Ca^{2+} into the cleft before the slower LCCs open. *iii*) If the LCCs fails to open in a dyad, Ca from the NCX may eventually trigger Ca^{2+} release from the SR. Previously we have reported that when the reverse mode of the NCX is blocked by KB-R7943 [10], the latency of Ca^{2+} release is prolonged by 3.2 ms [7]. The latency wass defined as the time between onset of the stimulus current and the start of the Ca^{2+} transient. This result suggests that

the reverse mode of NCX does indeed have an effect on the timing of the CICR. In the same study we used a detailed computational model of the dyadic cleft to investigate under what conditions the reverse mode of the NCX could precede the Ca^{2+} current from the LCC. We conclude that a co-localization of the NaC, the NCX and the RyR, together with a crowded environment, modeled with slow diffusion, are necessary. This corresponds to the two first scenarios from Bers [12]. A fourth scenario is that the NCX may modify CICR in failing cardiomyocytes, where it is reported that the intracellular $\left[Na^+\right]$ is raised [1, 13–15]. The elevated $\left[Na^+\right]$ is thought to be attributed by three possible mechanisms: *i*) enhanced late NaC [16]; *ii*) decresed Na^+/K^+-pump [17]; *iii*) increased Na^+/H^+-exchanger [18], but it is still not entirely understood [19]. The raised intracellular $\left[Na^+\right]$ during heart failure is expected to enhance reverse mode NCX function, and increase its contribution to CICR.

In this study we develop a detailed 3 dimensional computational model of the dyad. With this model we quantify two potential contributions to the uniform slowing and increased dyssynchrony seen in HF cells: *i*) difference in AP shapes (SHAM and HF) and *ii*) a displaced TT with respect to SR, modeled as an increased height of the dyadic cleft. We will record the latency defined as the time between the onset of the triggering stimulus to the first release of an RyR as measure of the slowing, and the variation in latency as a measure of dyssynchrony.

We will revisit our previous study of the contribution of the NCX to the rapid triggering of CICR in both failing and healthy cardiomyocytes [7], now with a more detailed computational model of the ion dynamics in the dyad. In Lines et al. [7] we modeled the single channel conductances as a continuous variable, linearly dependent on the whole cell current. Here we will model local ion channels as discrete channels, which are either on or off. We hypothesize that this can create a larger ionic response in the cleft, once a channel is open. The dynamics of the LCC and RyR channels will be modeled by discrete and stochastic Markov chain models.

In a recent study Poláková et al. [20] found that the coupling fidelity, i.e., the probability that a single open LCC will trigger a release from the SR, is much lower than 1. This implies that the number of LCCs in a couplon must be high to preserve an overall high probability for release. They also show that the low individual coupling fidelity is also compensated by the reopening of single LCCs. This is new insight as the coupling fidelity has previously been assumed to be high [21–23]. We will modify an existing Markov model of the LCC kinetics [24], so it complies with the quantitative measurements of the LCC dynamics that Poláková et al. [20] present. To the best of our knowledge, this is the first computational study to include the new findings from Poláková et al. [20] in a computational model of the dyad.

2 Methods

In this study we conducted two different types of computational experiments. The first was a study of the latency and dyssynchrony of Ca^{2+} release, and the second a study of the potential contribution of the NCX to the Ca^{2+} influx prior to release from the RyRs. Because of computational limitations, we used slightly different model approaches in the two studies. In the latency study we used stochastic and discrete Markov models

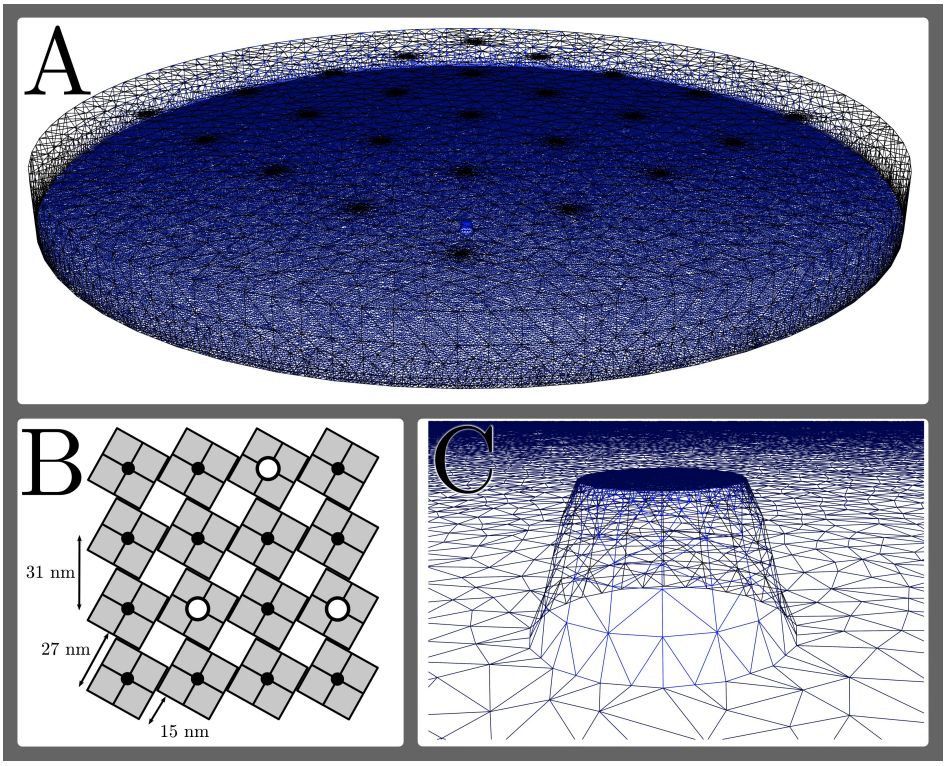

Figure 1: The figure shows a computational mesh we have used in the latency and dyssynchrony part of this study. Panel **A** shows the full mesh representing a dyad with a 110 nm radius. The RyRs are represented by 25 circular and distinct boundaries, with higher resolutions than the rest of the boundaries. The regularities of these channels are illustrated in panel **B**. A single LCC is positioned juxtapositional to one to the RyR. The actual boundary that represents the influx of the LCC is elevated 2 nm from the TT boundary, which is illustrated in panel **C**.

of both LCCs and RyRs. The electro-diffusion of the Ca^{2+} ions inside the cleft was described by a partial differential equation (PDE). The diffusional response from an open LCC was modeled using the quasi steady state solution of the PDE. The entire model was be driven by an external dynamic voltage clamp, using recorded APs from both SHAM and HF cardiomyocytes. In the second part of the study we did not include any stochastic modelling. However we did include two diffusional domains, Ca^{2+} and Na^{+}, which were coupled by the NCX. The model is non-linear due to the domain coupling. An open NaC was used to drive the model, and the Ca^{2+} response from a co-localized NCX was recorded.

Experimental methods

Animals were cared for in accordance with the Guide for the Care and Use of Laboratory Animals published by the US National Institutes of Health (NIH publication No. 85-23, revised 1996). Myocardial infarction was induced by left coronary artery ligation in 9 week-old female mice as previously described [5, 26]. Sham-operated animals (SHAM) were subjected to the same surgical procedure, but without ligation of the coronary artery. At 1 week following infarction, mice which had developed congestive heart

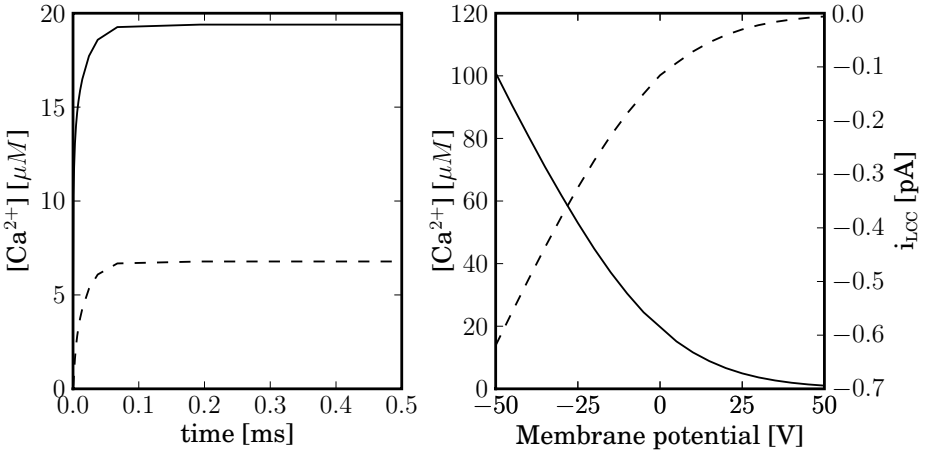

Figure 2: The figure shows the response from a single open LCC. The left panel shows the transient $[Ca^{2+}]$ at the juxtapositional RyR, (solid line) and at the next closest RyR (dashed line), which is 31 nm away. The membrane potential is held constant at 0 mV and the LCC opens at time = 0 ms. Steady state is reached after ~ 0.07 ms. The right panel shows the the steady state $[Ca^{2+}]$ response (solid line, left y-axis), from an open LCC channel for varying membrane potentials. The dashed line together with the right y-axis, shows the corresponding single channel amplitude. The current from a single channel was fitted so the amplitude equals -0.12 pA for a voltage step to 0 mV [25]. The single channel conductance is measured in the membrane potential range of [-50,-12.5] mV to 11 pS .

failure (HF) were selected by echocardiographic criteria for inclusion in the study [5, 26, 27]. Selected animals were then kept for an additional 9 weeks (a total of 10 weeks post-surgery) to allow development of chronic HF [27], and cardiocardiomyocytes were enzymatically isolated [5].

Cardiomyocytes loaded with Fluo-4 AM (20 μM for 30 min, Molecular Probes, Eugene, OR) were superfused with HEPES Tyrode solution containing (in mM): 140 NaCl, 1 CaCl2, 0.5 MgCl2, 5.0 HEPES, 5.5 glucose, 0.4 NaH2PO4 and 5.4 KCl (pH 7.4, 22°C). In some experiments, cells were field stimulated at 1 Hz (3 ms biphasic pulse, 50% above threshold) through a pair of platinum electrodes. In other experiments, cells were patch-clamped with 1-2 MΩ pipettes containing (in mM): 120 K-aspartate, 0.5 MgCl2, 6 NaCl, 0.06 EGTA, 10 HEPES, 10 glucose, 25 KCl and 4 K2-ATP (pH 7.2).

Ca^{2+}-dependent fluorescence was monitored using an LSM 510 confocal imaging system (Zeiss GmbH, Jena, Germany) in line-scan mode, as described previously [5]. A light-emitting diode was used to indicate the timing of the stimulus pulse. Line scan recordings were normalized to resting fluorescence values (F0) at each point along the line scan to obtain F/F0 images. Differences between populations were determined using Student's unpaired t-test. Statistical significance was defined as $P<0.05$.

Morphology

The dyadic cleft was modeled as a cylindrical disk, as has been done in other studies [28–30]. The height of the disk represents the distance between the SR and TT. In healthy cardiomyocytes this distance is ~ 12 nm [31]. The radius of the disk sets the size of the dyad. The number of included RyRs follows from the size of the radius,

as these large proteins are positioned in a highly regular 2D lattice grid [32], see Fig. 1 **B**. A cleft with a radius of 110 nm will have room for 25 RyRs, see Fig. 1 **A**, and a cleft with a radius of 220 nm will have room for 100 RyRs. The number of LCCs follows the number of RyRs. In this study we used a ratio of 1/5 between the number of LCCs and the number of RyRs. This is the same number as Tanskanen et al. [33] used in their model and it is similar to what is measured experimentally [34]. The assumption that the LCCs have low individual coupling fidelity demands a high number of LCCs in a dyad. This is to preserve an overall high probability of release [20]. We have chosen to include 20 LCCs in a dyad, which means a dyad with a radius of 220 nm. Unfortunately we are not able to simulate a transient process on such a large mesh since the computational effort is too large. This is mainly caused by two limiting factors: *i*) The large domain together with a demand of high resolution for the mesh close to the TT, creates a too large a computational mesh. *ii*) The numerically stiff process of the opening and closing of a single LCC, can be solved by taking small time steps. However it became to demanding to do this for 20 LCCs that needed to open and close several times each before a release was triggered. These limitations were resolved by using a quasi steady state approach to the simulated $\left[Ca^{2+}\right]$.

We used a dyad with a radius of 110 nm, seen in Fig. 1 **A**, with only a single LCC. This dyad was used to tabulate the steady state $\left[Ca^{2+}\right]$ at the closest and second closest RyR, for different membrane potentials, see Fig. 2. In the actual simulations we will only use the tabulated value for the nearest RyR, the one that is juxtapositional to the open LCC. This simplification can be justified by the large difference in amplitude between the two steady state responses. In Fig. 2 we see that the second closest RyR is exposted to a concentration that is $\sim 1/3$ of the closest RyR. The rate that controls the RyR opening, is of the fourth order, see as described below. This means that the propensity of the second closest RyR to open will be 1/81 of the propensity of the closest RyR. There can be at most 4 RyRs surrounding the juxtapositional one, reducing the effective difference in propensity to $\sim 1/20$. Therfore approximately in 1 out of 20 trials where a single LCC triggers release from an RyR, will the release come from one of the second closest RyR.

In the NCX study we limited the radius of the dyad to 50 nm. In this model we included a single NaC together with a single NCX. To be able to study the maximal effect of a higher local $\left[Na^{+}\right]$ from an open NaC, we co-localized the two membrane proteins, see Fig. 3. The distance between the two channel mouths is 3.5 nm. This distance is probably too small for real cardiomyocytes, as the size of the transmembrane proteins would make such a close co-localization impossible. However using such a small distance will get a theoretical maximal local $\left[Na^{+}\right]$. We also model the possible effect of protein crowding by lowering the height of the cleft to only 4 nm. This is a dramatically smaller cleft. Tanskanen et al. [33] use 13 nm instead of 15 to model the effect of the large proteins. However by choosing a relatively extreme value we could see if this way of modelling crowding could cause high enough local $\left[Na^{+}\right]$ to create a significant Ca^{2+} response from the NCX working in reverse mode.

We did not model the precise size and structure of the included channel proteins, as was done in the study by Tanskanen et al. [33]. However, in agreement with their study, we placed the channel pores from the included t-tubule channels 2 nm above the

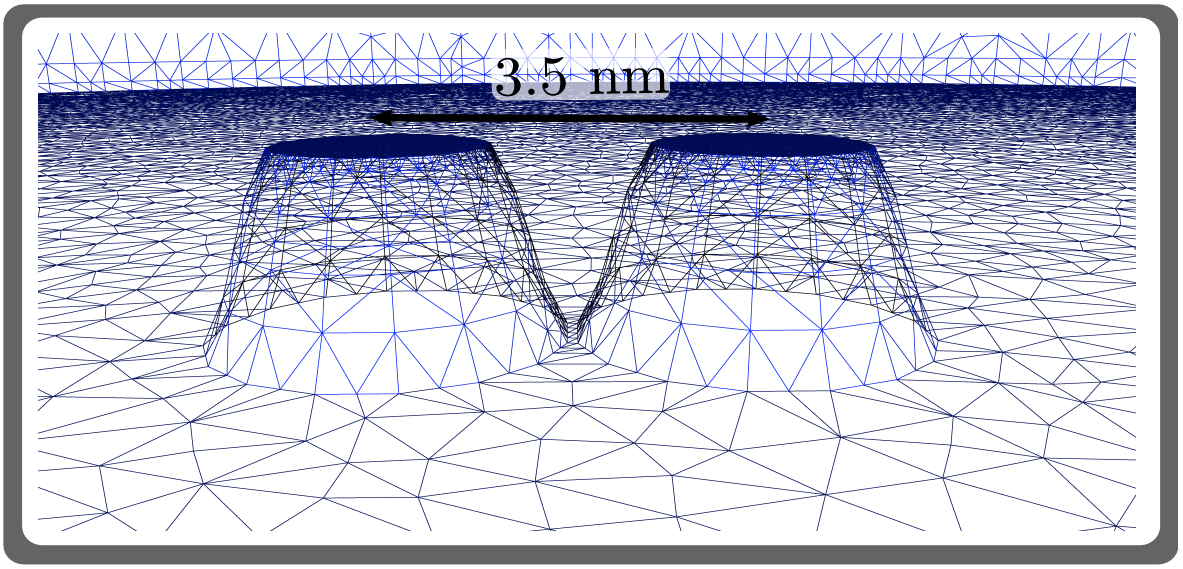

Figure 3: The figure shows how the co-localization of the Na channel and NCX is modeled. The distance between the two channel centers is 3.5 nm.

membrane. We used a radius of 1 nm for all channel pores. The strength of the channel fluxes depended on the model used to describe each flux. These models together with the parameters we have chosen to fit the fluxes to, are presented in the next subsection.

Continuous model

We will employ a continuous model for the ionic concentrations inside the cleft. Two previous computational models of the dyadic cleft computed the trajectories of each Ca^{2+} ion in the cleft individually [33, 35], using a Random walk model. Their motivation for doing so, was that there are too few Ca^{2+} ions inside the cleft, to justify a continuous approximation of the $\left[Ca^{2+}\right]$. This can be illustrated by a tentative dyad with a radius of 100 nm and a height of 12 nm. Here each μM of $\left[Ca^{2+}\right]$ correspond to an average 0.22 Ca^{2+} ion. During diastole, with a resting $\left[Ca^{2+}\right]$ of 0.1 μM, we will have in average 0.02 Ca^{2+} ions in this cleft. The steady state response from one open LCC, with an amplitude of $\sim$ 0.2 pA, is $\sim$ 50 μM (averaged for the whole cleft). This concentration corresponds to in average $\sim$ 12 Ca^{2+} ions. If we limit the volume of interest to a small space surrounding a single RyR, e.g., a half globe with a radius of 15 nm, and a apply a slightly higher $\left[Ca^{2+}\right]$ of 100 μM, we are down to an average of 0.1 Ca^{2+} ions. The small number of participating ions justify the questioning of the use of a continuous model for the $\left[Ca^{2+}\right]$. However in a recent study we show that it is not the average number of ions in the cleft that invalidates the use of a continuous model but rather the inflow rate of single Ca^{2+} compared to the binding rate to single receptors in the cleft [28]. In the case of the dyadic cleft, where the binding rates are indeed small compared to the inflow rates [28], even during diastole, we can use a continuous approximation of the $\left[Ca^{2+}\right]$, if we also use stochastic models for binding of single ions to receptors in the cleft.

The electro-diffusional process in the dyadic cleft is modeled by an advection-diffusion PDE. The electric field that drives the advection comes from the negatively charged phospholipid head-groups in the lipid bi-layer of the sarcolemma [36, 37]. Therefore in close proximity to the cell membrane, an electric double layer is produced in the intracellular solution [38, 39]. In this layer the electric potential is screened by the ions in the intracellular solution and attenuates rapidly. The negative potential attracts cations causing an elevated concentration of these ion species near the membrane and the anions are repelled. The charged head-groups of the membrane also serve as cation binding sites and thus acting as buffers for these ions [40, 41]. It has been shown that the Gouy-Chapman theory can be used to resolve the double layer [38], together with appropriate membrane association constants for the buffer [30, 40].

The ionic distributions, the amount of ions bound to the buffers and the electric potential are all coupled to each other. Bers et al. [40] developed an iterative scheme that solved the coupled system. They assumed that each of the three processes was in a steady state. With this assumption each process can be described as an explicit algebraic system. Soeller and Cannell [30] simplified the modelling of the double layer by assuming a monovalent 1-1 electrolyte consisting of [proteins] + $\left[\mathrm{Cl}^-\right] = \left[\mathrm{Na}^+\right] + \left[\mathrm{K}^+\right]$. The scheme can be divided into three stages: *i*) Calculating the intracellular potential based on the charge density from phospholipid head-groups. *ii*) Calculating the steady state ionic concentrations at the membrane based on the potential. *iii*) Letting the included ions species bind to the charged phospholipids based on the steady state concentration at the membrane, which in turn reduces the charge density. In the last stage the phospholipids are also titrated, based on the present $\left[\mathrm{H}^+\right]$, i.e., the pH of the solution, effectively reducing the charge density at the membrane [40]. See Appendix for a detailed presentation of the algorithm.

The scheme converges in a small number of iterations giving us the electric potential, Φ, described in dimensionless units as $\Phi = \Psi/\Psi_{\mathrm{T}}$, where Ψ and Ψ_{T} are given in Voltage. Ψ_{T} is a temperature dependent characteristic potential given by

$$\Psi_{\mathrm{T}} = k_{\mathrm{B}}T/e. \tag{1}$$

A single exponential can be used to approximate Φ:

$$\Phi = \Phi_0 \, \mathrm{e}^{x_2/\lambda_{\mathrm{D}}} \, . \tag{2}$$

Here Φ_0 is the potential at the membrane, where x_2 is zero, and λ_{D} is the Debye length. We chose to increase the amount of phospholipids to 563 nmol/mg compared to Soeller and Cannell [30] to attain the same value for $\Phi_0 = -2.2$ as they use. We chose to do this so the resulting advection-diffusion equation is comparable between the too studies. However the differences in the amount of phospholipids points to discrepancies in the underlying algorithms.

The Debye length is dependent on the ionic concentration, see Eq. 12, and quantifies the screening strength of the double layer. The smaller the Debye length is, the larger the screening strength. An intracellular environment with [proteins]+$\left[\mathrm{Cl}^-\right]$ +$\left[\mathrm{K}^+\right]$ +$\left[\mathrm{Na}^+\right]$ =310 mM gives a Debye length of 0.78 nm. However it is questionable whether the proteins, which carry most of the negative charges in the electrolyte, can move as

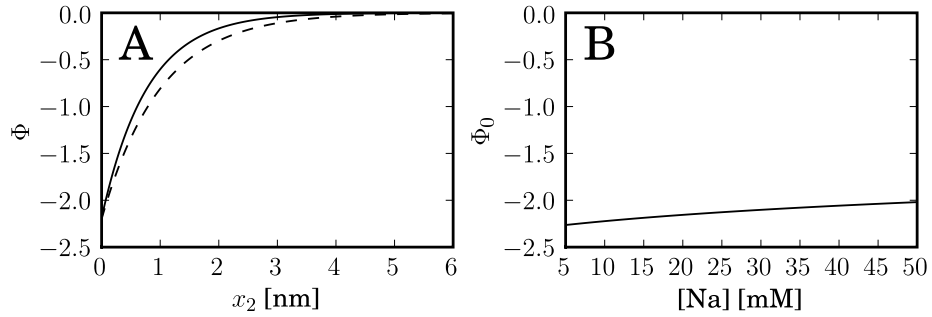

Figure 4: The figure shows the electric potential, Φ, from the charged phospholipids. In panel **A** Φ is plotted against the distance to the membrane, using the mono exponential representation of Φ from Eq. 2, using $\lambda_D = 1$ nm (solid line) and $\lambda_D = 0.78$ nm (dashed line). Panel **B** shows the electric potential at the membrane, Φ_0, as a variable of the intracellular bulk $\left[Na^+\right]$. We see that the variation in Φ_0 is small over a large range of Na^+ concentrations.

freely as Cl^-. We therefore assumed that the screening effect was lower, and we use λ_D = 1 nm.

Interestingly, two previous studies have also used 1 nm as the Debye length corresponding to a weaker monovalent 1-1 electrolyte of 190 mM [30, 33]. In Fig. 4 **A**, we show the electric potential Φ from Eq. 2 as a variable of height of the cleft, x_2. The solid line shows the potential using a Debye length of 0.78 nm and the dashed line the potential using a Debye length of 1 nm. Both use the mono exponential approximation of Φ.

Assuming that the curvature of the TT is much larger than the Debye length, and that the variation in the computed Φ_0 is small for the included ion species, we can use the one dimensional expression for Φ from Eq. 2 as a static expression for the whole cleft. The first assumption is reasonable. The second assumption has to be validated for the included ion species. Soeller and Cannell [30] show in their study that this is true for a large variation of $\left[Ca^{2+}\right]$. In the NCX simulations we included Na^+ in our model and we have to check that Φ_0 does not change substantially for larger values of $\left[Na^+\right]$. In Fig. 4 **B** Φ_0 is plotted for a range of different bulk $\left[Na^+\right]$. We see that the potential does not vary substantially.

We can now state the advection-diffusion equation that governs the movement of ions in the dyad:

$$\frac{\partial c_i}{\partial t} = D_i \left(\nabla^2 c_i + \nabla \left[c_i z_i \nabla \Phi \right] \right). \tag{3}$$

Here D_i and z_i are the diffusion constant and the valence of the i^{th} ion, respectively. In addition to the no-flux boundary condition, which is employed at all membrane boundaries, we include four different types of ion fluxes: *i)* the Na^+ and Ca^{2+} outflux to cytosol, *ii)* influx of Ca^{2+} from the LCC, *iii)* influx of Na^+ from the NaC and, *iv)* the bidirectional flux of both Na^+ and Ca^{2+} from the NCX. As we in this study focus on the release latency, defined as the time between onset of stimulus and the triggering of the first RyR, we do not include the flux from the actual RyRs. The cytosolic ion fluxes are treated as a concentration dependent boundary fluxes. The i^{th} ion flux to cytosol is given by: $J^i_{\text{cyt}} = -D_i \left(c_i - C^i_{\text{cyt}} \right) / \Delta S_{\text{cyt}}$, where c_i and C^i_{cyt} are the

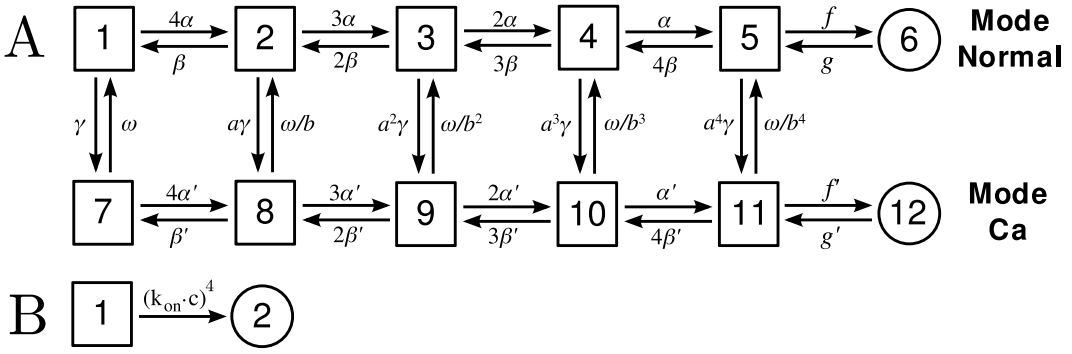

Figure 5: The figure shows the Markov model scheme used for the LCC model, **A** and the simplistic activation scheme used for the RyR model, **B**. The LCC scheme is the same as a previously presented model [24, 46]. We have fitted the $\alpha(V)$, $\beta(V)$, f and g rates to the experimental data presented in Poláková et al. [20]. We have also re-fitted the γ_0 parameter, so the overall γ rate during a steady state response from a single LCC, is the same as it is in the study of Greenstein and Winslow [24]. The k_{on} is fitted so the mean latency for the healthy dyad, cleft height of 12 nm, corresponds to the experimentally measured value of 5 ms, see Fig. 8

concentration at the boundary and in the cytosol respectively, and ΔS_{cyt} is the distance to where the concentration is assumed to be C^i_{cyt}. The LCC Ca^{2+} flux is governed by the Goldman-Hodgkin-Katz equation [42], which is linear in $\left[Ca^{2+}\right]$ and can therefore be treated similar to the cytosolic fluxes. The permeability of a single LCC is chosen so the amplitude of the current is -0.12 pA for a voltage step to 0 mV at room temperature [25]. We use an ordinary Nernst equilibrium potential to describe the NaC flux. The Nernst potential is updated each time step as the intracellular $\left[Na^{+}\right]$ increases. The single NaC conductance is chosen to be 25 pS [43]. The dynamics of the NCX flux is governed by the equation given in Shannon et al. [44], with a single current amplitude fitted to 0.2 fA for an intra- and extracellular $\left[Na^{+}\right]$ of 40 mM and 0 mM of extra- and 4 mM of intracellular $\left[Ca^{2+}\right]$, together with a membrane potential of 0mV and a temperature of 35°C [45].

The NCX flux and the LCC and RyR Markov models, see below, are dependent on the value of the concentration fields at their positions. These are communicated to each model, by averaging the value of the field at the channel mouth.

Discrete and stochastic models

We use discrete and stochastic Markov models to describe the channel dynamics of the LCCs and of the RyRs. The LCC model is a modified version of the 12 state model previously used by Greenstein and Winslow [24] and first described by Jafri et al. [46], see Fig. 5 **A**. The model represents 4 voltage activated subunits. Each subunit can be in a permissive or non permissive state. When all 4 subunits are in a permissive state the channel can undergo a voltage independent transition to a conducting state. Ca^{2+} inhibition is modeled as a $\left[Ca^{2+}\right]$ dependent transition to mode Ca^{2+}, see lower row in Fig. 5 **A**. We modify the voltage dependent α and β rates together with the voltage independent activation and deactivation rates, f and g, so the model fits the reported kinetics from Poláková et al. [20]. The presented rates are for 22 °C, as both our own

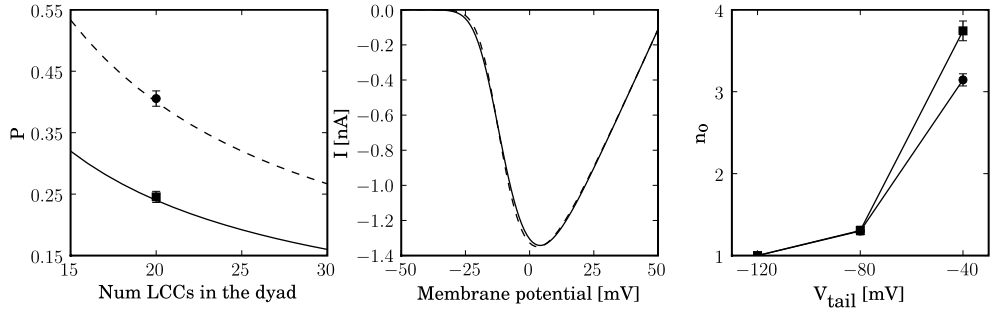

Figure 6: The figure shows the result of the fitted rates in the LCC Markov model. The left panel shows the single channel open probabilities after a step to 60 mV from a holding potential of -50 mV for 1.5 ms, solid line, and 5.0 ms dashed line, as it is estimated by Poláková et al. [20]. The open probabilities are plotted against the number of LCCs in a dyad. We fitted the LCC rates to correspond to the single channel open probabilities when there are 20 channels in the cleft. The recorded probabilities from our model, are represented by the square, (after 1.5 ms) and the circle (after 5.0 ms). The mid-panel shows the whole cell steady state current response after different voltage steps, from our fitted model (dashed line) and from Poláková et al. [20] (solid line). We used the steady state open probabilities from our model together with the driving force of: V-53.3 mV, to fit the curve. The right panel shows the mean number of LCC openings before deactivation after a step to three different potentials, -120 mV, -80 mV and -40 mV. The square and the circle represents the number of openings after an initial step to 60 mV during 1.5 and 5.0 ms respectively. This panel corresponds to the results presented in Fig. 3C in Poláková et al. [20], and they are fitted qualitatively.

experimental results are from this temperature together with the results from Poláková et al. [20].

The α rate is given by a sigmoidal rate function:

$$\alpha(V) = \frac{1.7}{1 + \mathrm{e}^{-\frac{V-13}{12}}}, \tag{4}$$

and the β rate is given by a single exponential:

$$\beta(V) = 0.35\,\mathrm{e}^{-\frac{V+40}{20}}\,. \tag{5}$$

Here V is the membrane potential. The voltage independent activation rate f was fitted to 1.5 ms^{-1} and the deactivation rate, g, was estimated directly by Poláková et al. [20] to 2.0 ms^{-1}. We used three experimental measures from Poláková et al. [20] to fit the α and β functions and the activation rate f: *i*) the single open probabilities after two steps to 60 mV lasting 1.5 ms and 5.0 ms respectively, *ii*) the steady state whole cell I-V response, and *iii*) the number of channel openings after a step to different tail potentials, succeeding an initial step to 60 mV.

Poláková et al. [20] estimate the number of open LCC in a dyad after a step to 60 mV that lasts for 1.5 ms and 5.0 ms, to 4.8 and 8.0 respectively. If we divide these numbers with the number of LCC in a single dyad we get an estimate of the open probabilities for a single channel, after the two steps. In the left panel of Fig. 6, these open probabilities are plotted as a function of the total number of LCCs in the dyad. The solid line show the probability after a 1.5 ms step and the dashed line the probability after a 5.0 ms

step. We fitted our rates to a total number of 20 LCCs in the cleft. We mimicked the conditions for which Poláková et al. [20] made their experimental results, and held the potential first at -50 mV, then we stepped the potential to 60 mV for 1.5 and 5.0 ms. This was done 100 times. We recorded the number of open channels and divided by the total number of channels in the cleft, 20, to get the single open channel probabilities. These are plotted in the left panel of Fig. 6, after 1.5 ms (square) and after 5.0 ms (circle). We also fitted the steady state whole cell I-V response of the model to the one from Poláková et al. [20]. This was done by first calculating the steady state open probability of the model, a sigmoidal curve, and weighting this with the same linear voltage dependency from Poláková et al. [20], see figure legend in Fig 3. in this study. The result from the fit is presented in the mid panel of Fig. 6. Here the I-V function from Poláková et al. [20] is represented by the solid line and the I-V relationship from our model is represented by the dashed line.

A key observation from Poláková et al. [20] is that an LCC reopens several times before the Ca^{2+} release. They quantified this by calculating the number of re-openings a single Ca^{2+} channel would undergo during a step to different tail potentials. We fitted our model qualitatively to these data too. We stepped our model to 50 mV during 1.5 ms and 5 ms, to open the channel. After this test step, we step the potential to a tail potential during 10 ms, and recorded the mean number of re-openings during this period. The result is presented in the right panel of Fig. 6 and should be qualitatively compared to the results presented in Fig. 3C in Poláková et al..

We employed a minimalistic Markov model scheme for the RyRs, which is presented in Fig. 5 **B**. The scheme follows a fourth order activation kinetics [20]. The k_{on} rate was fitted so the mean latency for a SHAM AP was 5 ms, see Fig. 8. For our specific geometry and diffusion model this number was 0.069 μMms^{-1}.

Numerical methods for the continuous model

We used a finite element method for the spatial discretization of the PDEs, and a backward Euler method in time. The non-linearities introduced by the NaC and the NCX were handled by using the value of the concentration field at the beginning of the times step. The size of the time step was determined by an adaptive time stepping scheme based on the max value of the relative time derivative of the included fields. We used the streamline upwind/Petrov-Galerkin stabilizing method [47], together with a fine mesh at the TT membrane, to stabilize the advection term in Eq. 3. The sparse linear system was assembled and solved using `PyDOLFIN` from the `FEniCS` project, (`http://www.fenics.org`), together with the `PETSc` linear algebra library [48].

Numerical methods for the discrete models

Some of the propensity functions in the Markov models we used depend on continuous variables. The LCCs depend on the membrane potential wave forms, see Fig. 7, and the RyRs will depend on the quasi steady state $\left[Ca^{2+}\right]$ response when the juxtapositional LCC is open. To be able to correctly evolve the stochastic system we therefore needed to solve the discrete system coupled to these variables. We developed a modified Gillespie

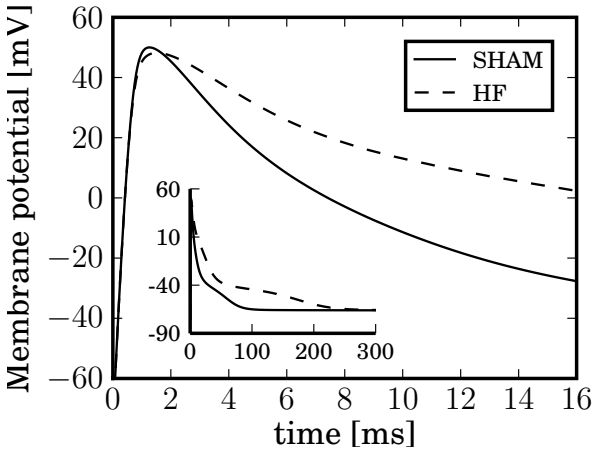

Figure 7: The figure shows representative action potentials registered from SHAM and HF cardiomyocytes. These wave forms are used to drive the dyadic model.

method [49] to accomplish this. It is similar to methods used by previous studies [50, 51].

The present values of the states in the included Markov models were kept in a state vector, $S = S(t)$. Let $N = N(S)$ be the number of possible transitions that can be undertaken from these states. The propensity function of the i^{th} transition is denoted by λ_i. The total propensity for the next transition, $\lambda = \lambda(S, t)$, is given by a sum over all $\lambda_i = \lambda_i(t)$,

$$\lambda = \sum_{i}^{N} \lambda_i. \tag{6}$$

The time for the next stochastic transition is exponentially distributed, if we assume that λ is constant. The time to the next stochastic transition, Δt_t, can then be realized by drawing one random number, r_1, from an uniform distribution on the unit interval and transform it according to:

$$\Delta t_t = -\ln(r_1)/\lambda. \tag{7}$$

The transition time is relative to the present time in the simulation. Given a transition, at time $t + \Delta t_t$, we then have to realize which of the N possible transitions actually takes place. This was done by drawing another random number, r_2, from the same distribution as above. The k^{th} transition take place if,

$$\sum_{j=0}^{k-1} \lambda_j \leq \lambda \cdot r_2 < \sum_{j=0}^{k} \lambda_j, \tag{8}$$

where $\lambda_0 = 0$, and $k = [1 \dots N]$.

The Gillespie method assumes constant propensity functions between the transitions. Most of the included propensity functions in the LCC and RyR models are not constant. The α function in the LCC model will for example rise fast during the upstroke of the AP. We can therefore not assume constant propensity functions between transitions and

we have to modify the method. We do this by first realizing a dimensionless time to the next transition, Δt_t^*, i.e., we set $\lambda = 1$ in Eq. 7. Δt_t^* relates to the actual transition time by,

$$\Delta t_t = \Delta t_t^* / \lambda. \tag{9}$$

We then choose a time step, $\Delta t < \Delta t_t$, during which we assume constant external variables, hence constant propensity functions. To minimize the error of assuming constant continuous variables during a time step we need to choose a small Δt when such variables change much. During an upstroke of the AP we therefore need to choose smaller Δt.

The continuous system is then updated using the chosen Δt. After this is done we update the dimensionless transition time according to,

$$\Delta t_t^* = \Delta t_t^* - \Delta t\, \lambda. \tag{10}$$

Whenever Δt_t, from Eq. 9, is smaller than the chosen Δt a transition occurs before the time step is over. We realize the transition and check whether the transition change the status of a channel. If it does we say that the transition is a *channel transition*. The continuous system is solved up to the transition time by setting $\Delta t = \Delta t_t$. Finally we realize the transition, changing the state of the continuous system. We then have to draw a new dimensionless transition time, Δt_t^* and start over again. If the transition was not a channel transition we can skip it, but we need to draw a new dimensionless transition time.

3 Results

Experimental results

We defined latency as the time delay between the stimulus and the onset of the Ca^{2+} transient [7]. In field-stimulation experiments on isolated cardiocardiomyocytes, line-scan images, Fig. 8**A**, and spatially-averaged Ca^{2+} transients Fig. 8**B** showed a longer latency in HF cells than in SHAM. Mean field stimulation data are presented in Fig. 8**C**, left panel. Line scan images also indicate that Ca^{2+} release was more dyssynchronous in HF than SHAM (Fig. 8**A**), which contributed to a slower rate of rise of the Ca^{2+} transient (Fig. 8**B**).

Computational results

We conducted two different types of simulations, one where we recorded the release latency for the dyad during different circumstances, and one where we quantified the reverse mode of an NCX while co-localizing it with a NaC. In the latency simulations we used stochastic models of both LCCs and RyRs. In the NCX simulations we only used a coupled continuous solver of both $\left[Ca^{2+}\right]$ and $\left[Na^{+}\right]$.

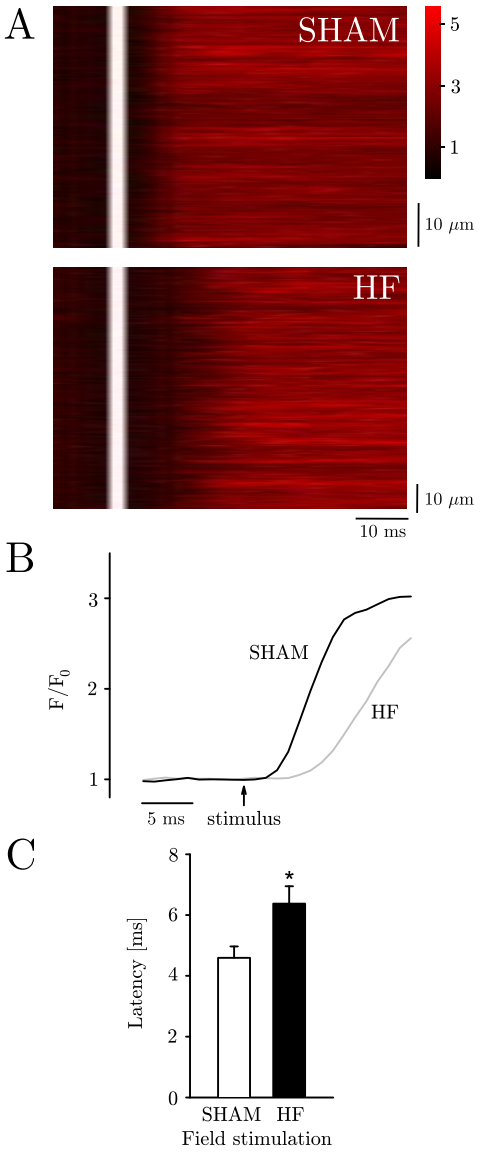

Figure 8: Ca^{2+} release latency was prolonged in HF cardiomyocytes. **A** Line-scan recordings of Ca^{2+} transients (normalized to resting fluorescence, F/F0) from field-stimulated cardiomyocytes. Stimulus timing is indicated by the vertical white line. **B** Spatially-averaged plots of the recordings in Panel **A**, on an expanded time scale. **C** Mean latency measurements in field-stimulated cells (nSHAM = 16, nHF = 16, * $P < 0.05$).

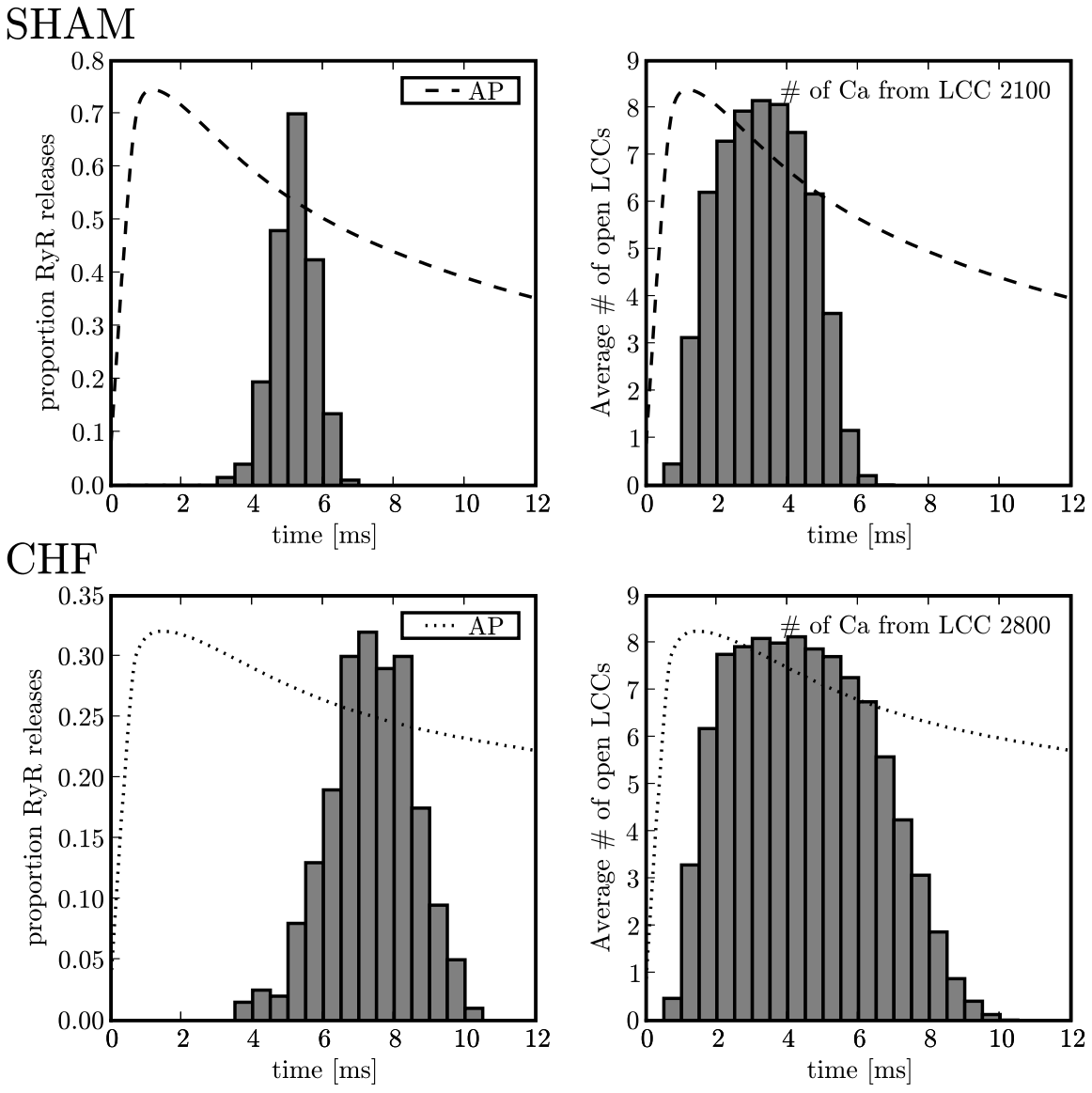

Figure 9: The left columns of this figure shows the distributions of latencies, defined as the time for opening of the first RyR. The latencies are collected from 400 simulations of the dyadic model and are distributed proportionally. The dashed line represents the SHAM AP (not to scale), which is used to drive the model. The left panel in the lower row shows the latencies from 400 simulations of the model, when it is driven by a HF AP (dotted line). See Fig. 7 for a quantitative representation of the AP wave forms. The mean latency is 5.2 ±0.6 ms for the SHAM AP, and 7.3 ±1.2ms for the HF AP. The right column of the figure shows the average number of LCC openings in the dyad during the same simulations as the latency recordings shown in the left column. A single bar is 0.5 ms wide and the height of the bar represents the average number of LCC openings during that time interval.

Latency and dyssynchrony study

In the latency study we used a dyad with 20 LCCs, each facing one RyR. We applied two different AP wave form to drive the simulations: one from a cardiomyocyte from a SHAM operated mouse, and one from a cardiomyocyte from a HF mouse, see Fig. 7. The system was simulated 400 times. The latency, defined as the time between the onset of the AP wave form and the first opening of an RyR, was registered for each simulation, and this also defined the end of each simulation. The left column of Fig. 9 presents the latency distributions for the two different APs; upper row SHAM AP, and lower row HF AP. The data is plotted together with not-to-scale representation of the AP wave forms. The height of the bars represents the proportion of simulations that had a release latency corresponding to the time interval of that bar.

The mean latency was 5.2 ±0.6 ms for the healthy SHAM AP, and was prolonged to 7.3 ±1.2 ms for the HF AP. Interestingly we observed a faster and sharper distribution of latencies from the healthy cardiomyocyte. The SHAM AP repolarized more rapidly, causing larger amplitude Ca^{2+} influx from any opened LCC as the driving force from the AP increased. A larger LCC amplitude produced a higher $\left[Ca^{2+}\right]$ response at the RyRs, see Fig. 2, which resulted in a faster and sharper latency distribution for the SHAM AP. It is noteworthy to point out that the increase in latency in HF and greater variability of latency values was only due to the AP shape, as no other parameters were altered.

The number of LCCs required to open in the dyad before a release is triggered is presented in the right column of Fig. 9. The height of the bars represents the average number of open LCCs during the time interval of each bar (0.5 ms). We observed that the number of open LCC is smaller in the simulations using the SHAM AP. The mean number of open LCCs before a release was 60 for the SHAM simulations and 110 for the HF simulations. Each LCC opening in the HF simulations causes a smaller Ca^{2+} response due to the higher membrane potential and more LCC openings are therefore needed to trigger a RyR opening. The average number of Ca^{2+} ions that entered the cell before a release is also higher for the HF simulations. This number was 2100 for the SHAM simulations and 2800 for the HF simulations. This is interesting because it indicates that more Ca^{2+} enteres the cell through the LCC before the LCC will be inactivated by the Ca^{2+} release from SR. This supports our recent observations that the Ca^{2+} current and Ca^{2+} transient amplitude are increased in the failing AP, results not shown. Despite these advantageous effects, our present results illustrate that the the failing AP also promotes greater latency and dyssynchrony of Ca^{2+} release.

We also examined the timing of Ca^{2+} release while altering the height of the dyad, modelling different grades of displacement of the TT during HF. In these simulations, only the HF AP was employed. We used dyads with 4 different heights: 15, 20, 30 and 40 nm. The latency distributions from these simulations are presented in Fig. 10. In 3 % of the simulations, where the height of the dyad was 40 nm, release did not occur. The mean release latencies from the four different dyads were: 12.3 ±2.3, 15.2 ±3.2, 19.8 ±4.2 and 23.4 ±4.9 ms. We see a progressive delay in release from the dyads with a larger cleft. The distribution of latency values was also broadened with increased dyad heights. Thus, the effects of broadening the dyadic cleft produce similar effects on Ca^{2+} release as prolonging the AP, namely an increase in release latency and decrease

in release synchrony.

NCX study

We investigated the potential contribution to CICR from an NCX positioned in the cleft. We co-localized the NCX with an open NaC, see Fig. 3. The NCX amplitude, the $\left[Ca^{2+}\right]$ and $\left[Na^{+}\right]$ response at the NCX for different membrane potentials, were recorded. The recordings were made with a normal cleft and a crowded cleft. The crowdedness was modeled by reducing the cleft height to 4 nm. In Fig. 11 left panel we see the amplitude of the NCX for a normal (solid line) and crowded cleft (dashed line). Note that for the presented voltages we only got reverse mode NCX, that is to say, ony positive current. We see that the differences are small. In the right panel we plot the $\left[Ca^{2+}\right]$ (left y-axis) and $\left[Na^{+}\right]$ (right y-axis) responses at the mouth of the NCX from the normal, (solid and dashed dotted lines) and crowded (dashed and dotted lines) cleft. We oberved that the $\left[Ca^{2+}\right]$ responses more or less followed the NCX current for both normal and crowded cleft, however slightly larger $\left[Ca^{2+}\right]$ response is registered for the crowded cleft. This corresponds to the larger $\left[Na^{+}\right]$ response at the NCX, shown in the right panel.

To investigate a potential contribution to the reverse mode during HF when the resting $\left[Na^{+}\right]$ is reported to be increased, we also conducted the same simulations with a slightly elevated $\left[Na^{+}\right]$ of 20 mM [15] compared to a healthy cardiomyocyte with a resting $\left[Na^{+}\right]$ of 15 mM. The results presented in Fig. 12 indicate increased reverse mode NCX current in HF compared to healthy cardiomyocyte.

The $\left[Ca^{2+}\right]$ responses at the NCX mouth as seen in Fig. 11-12 are too small to have any impact on the Ca^{2+} release from the RyR across the cleft. This can be seen by comparing the $\left[Ca^{2+}\right]$ at the RyR from an open LCC, see Fig. 2. Here the $\left[Ca^{2+}\right]$ response is $\sim 20\ \mu$M at the closest RyR, after a step to 0 mV. The maximal $\left[Ca^{2+}\right]$ an NCX experience is $\sim 3\mu$M. We see that for the reverse mode of the NCX to be high, it needs a high membrane potential. However a higher membrane potential causes a lower $\left[Na^{+}\right]$ response from the open NaC, which reduces the effect of a higher $\left[Na^{+}\right]$ from the co-localized NaC and NCX.

4 Discussion

In this study we have used a detailed computational model of the dyad to investigate the latency and dyssynchrony in a single dyad during heart failure. The latency was defined as the time between the onset of an AP and the first opening of an RyR. The dyssynchrony is the variation (standard deviation) of the latency. We have also used the model to investigate the possible contribution from the NCX working in reverse mode to the CICR.

Latency and dyssynchrony study

The latency distribution is delayed and broadened when we use a HF AP, 7.3 $\pm$1.2ms, compared to the SHAM AP, see lower left panel of Fig. 9. This is only due to the

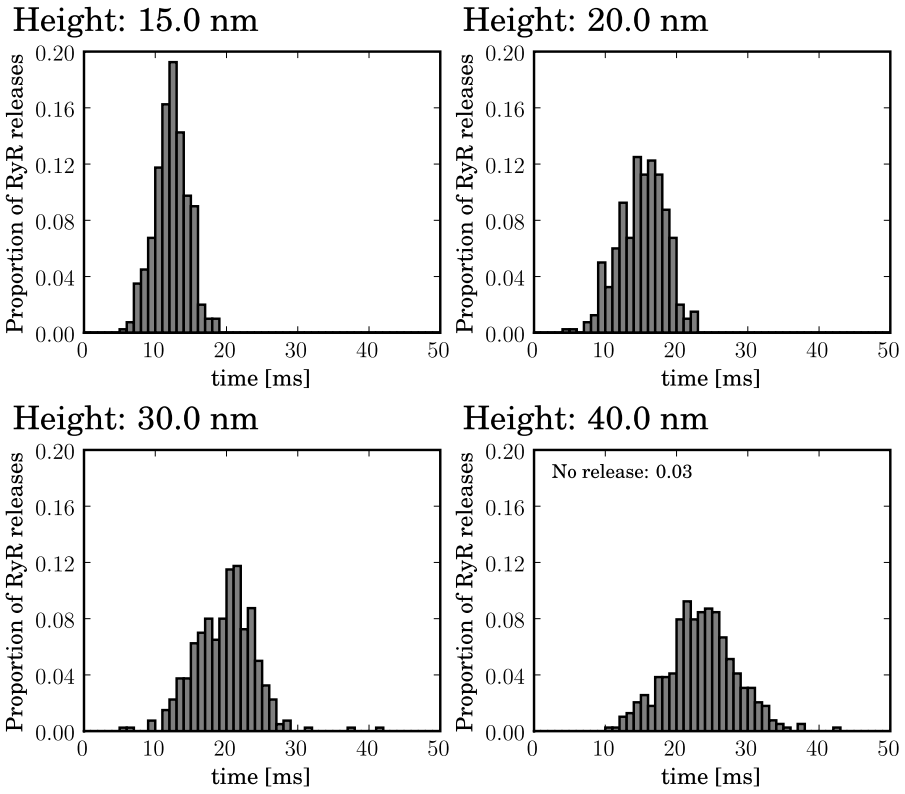

Figure 10: The figure shows the latency distributions from dyads where the TT has been moved away from the SR, modelling small and modest TT disruptions during HF. A healthy dyad in our model, has a cleft height of 12 nm. This figure shows the results from dyads with cleft heights of 15, 20, 30 and 40 nm with mean latency distributions of 12.3 ±2.3, 15.2 ±3.2, 19.8 ±4.2 and 23.4 ±4.9 ms respectively. A fraction of 0.03 of the simulations from the dyads with cleft height of 40 nm did not result in a release.

differences in AP wave form, see Fig. 7. The faster repolarization for the SHAM potential creates a larger driving force for the LCC current, hence a larger $\left[Ca^{2+}\right]$ response at the juxtapositional RyR, see right panel of Fig. 2. The longer latency for the HF AP can contribute to the delay in Ca^{2+} reported by Louch et al. [5]. But we also show that the number of Ca^{2+} ions that enters the cell from the LCC before the release from the RyR is larger for the HF AP, 2800, than for the SHAM AP, 2100. The LCCs inactivates with high cytosolic $\left[Ca^{2+}\right]$, which means that more Ca^{2+} ions enters the cell before the LCC starts to inactive. This together with the longer depolarized phase for a HF AP helps filling the cell and hence SR with more Ca^{2+}. These observations correspond to reported cellular measurments in the mouse model of HF [27], which have elevated Ca^{2+} content and larger Ca^{2+} influx during the HF AP.

We showed that small perturbations in the TT structure, here modeled by a larger cleft height, can also promote longer Ca^{2+} release latency and greater dyssynchrony. Even a small perturbation in cleft height from 12 nm to 15 nm give a significant longer latency, 13 ± 2.9ms compared to a normal cleft of 12 nm height, 7.3 ±1.2ms. Larger perturbations give longer latencies. Dyads with height of 30 and 40 nm produced large latencies, 22.3 ±4.7ms and 25.4 ±5.6ms, which indicates that these might be

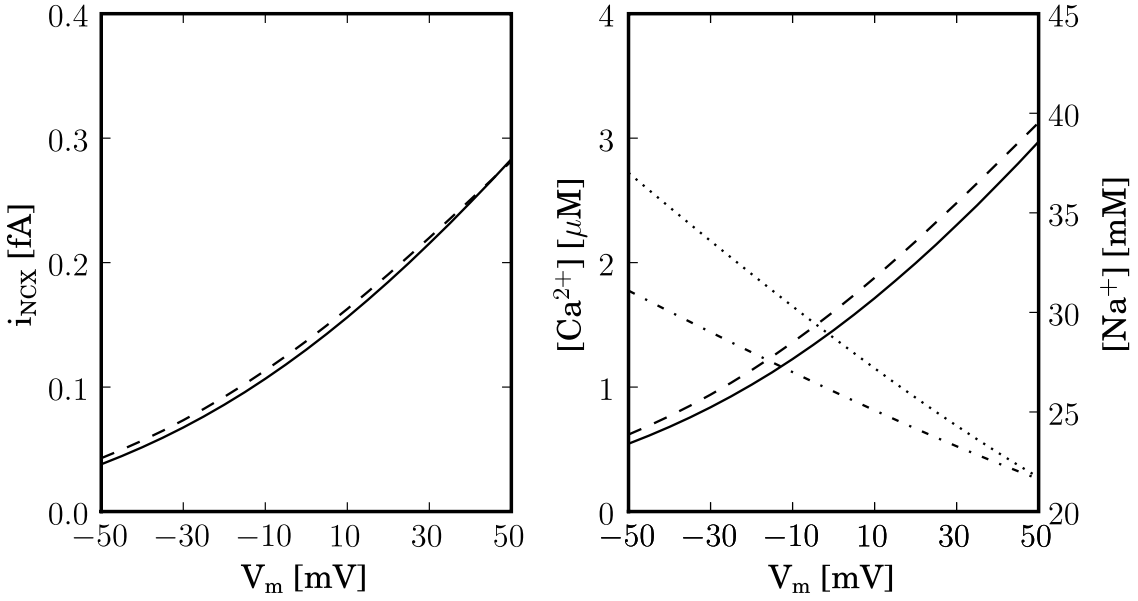

Figure 11: The figure shows the effect of co-localizing a Na^+ channel and an NCX inside the dyad with respect to the NCX current amplitude. The left panel shows the steady state NCX current for different membrane potentials, and for two different geometries, normal cleft (height = 12 nm, solid line) and crowded cleft (height = 4 nm, dashed line). Note that the NCX is only working in reverse mode, as the current is positive for the whole voltage range. The right panel shows the $[Na^+]$ and $[Ca^{2+}]$ response at the mouth of the exchanger. The solid and dashed line represents the $[Ca^{2+}]$ (left y-axis), for the normal and crowded cleft respectively. The dashed-dotted and dotted line represents the $[Na^+]$ (right y-axis), for the normal and crowded cleft respectively.

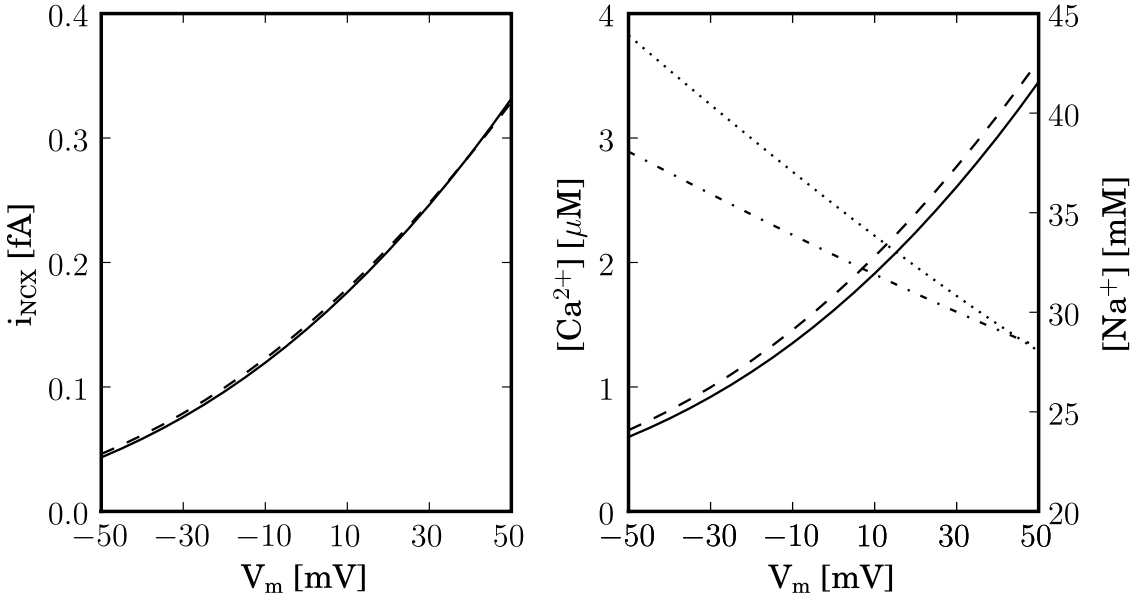

Figure 12: The figure shows the NCX response when the resting $[Na^+]$ is 20 mM [15]. Se Fig. 11 for a description of the traces.

dysfunctional, i.e., not able to trigger release locally. Most dyads has smaller latencies than 20 ms, see Fig. 8 **A** HF figure. This means that dyads with later latencies than this have to be triggered by Ca^{2+} diffusing from neighbouring dyads.

We show that a dyad containing 20 LCCs creates a reliable release unit, with a sharp latency distribution. The mean latency for a dyad using a SHAM AP is 5.2 ±0.6ms, see the upper left panel of Fig. 9. This latency is comparable with experimental results, see Fig. 8. The coupling fidelity is low for a single open LCC. We measured the coupling fidelity to 0.11, for a step in membrane potential to 10 mV. This is a bit less than reported by Tanskanen et al. [33], who operates with a coupling Fidelity of 0.15 after a step to 0 mV. Interestingly we get an earlier and more synchronous latency with our model, see Fig. 6A in their study. We think this is due to the higher number of LCCs we include in our dyad, 20, compared to the four LCCs included by Tanskanen et al. [33]. The synchronous distribution of the latencies indicates that the response from a single dyad is reliable in spite of the low coupling fidelity of an open LCC.

We recognize that the model for the RyR activation is minimalistic and does not reflect the present knowledge of the modelling of RyR activation [52]. However it includes the fourth order activation kinetics that we show are important for determining the number of RyRs a single LCC is able to activate. An extension of the model to also include modulation of RyR activation with luminal $\left[Ca^{2+}\right]$ and possible Mg^{2+} [53] is a natural continuation of the present study. We also recognize that our model does not include realistic geometries of the RyRs and LCCs in the cleft. This will alter the quasi steady state distribution of $\left[Ca^{2+}\right]$ after an open LCC, although probably not to the same extent as the electric field. However the inclusion of the geometry introduces the question of where the different Ca^{2+} receptors are situated on the proteins. This will change the $\left[Ca^{2+}\right]$ detected by for example the RyR and hence alter the activation kinetics [33]. The latency results of our study would probably not be altered by these natural extensions as the RyR activation propensity is a free parameter in our study, which is fit to correspond to measured mean latency for a healthy dyad. Another limitation of our study is that we do not include any sarcolemmal buffer in the model. The inclusion of buffers in the model would have slowed the establishment of the steady state $\left[Ca^{2+}\right]$ response at the juxtapositional RyR. This means that the quasi steady state assumption we have used in our study might not hold, and a more elaborated model would be needed.

NCX study

Using our model we have shown that Ca^{2+} coming into the dyad prior to an LCC through an NCX working in reverse mode cannot trigger Ca^{2+} release alone. We hypothesized that modelling the Na^+ flux as a single channel, instead of a proportion of the whole cell current [7], we would get a larger Ca^{2+} influx response from the NCX. However, we got the opposite result. In Fig. 11 we show that the $\left[Na^+\right]$ at the NCX is inversely proportional to the membrane potential. Hyperpolarized membrane potential gave a strong $\left[Na^+\right]$ response at the NCX, but a low NCX amplitude. At more depolarized membrane potentials there is a larger chance that the NaC will be open but the resulting $\left[Na^+\right]$ at a nearby NCX will be small. This means that we cannot get a large $\left[Na^+\right]$

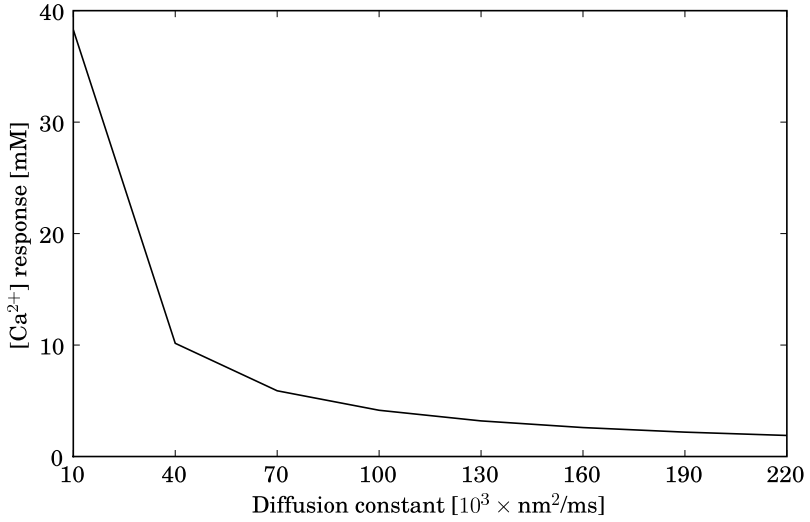

Figure 13: The figure shows the Ca^{2+} concentration at the mouth of an open RyR in the middle of a dyad with 220 nm radius for different values of the Ca^{2+} diffusion constant. We have used a fixed amplitude of the RyR current: 0.5 pA. This value is similar to what is reported from bi-layer experiments [54], but slightly lower than a value reported from an indirect measurement from a cardiomyocyte [55]. We see that for a low number of the diffusion constant: 10^4 nm^2 ms^{-1}, we get a Ca^{2+} response that is far above the typical concentration in SR: $\sim$ 2 mM [1]. For the value of the diffusion constant we have used: 2.2×10^5 nm^2 ms^{-1} we get a reasonable Ca^{2+} response in the range of the SR content.

response at the NCX together with a depolarized membrane potential. We also found that the crowdedness, modeled with a lower cleft, does not contribute significantly to the reverse mode of the NCX. Neither does an elevated resting $\left[Na^+\right]$ (modelling a raised $\left[Na^+\right]$ during HF) have any effect, see Fig. 12. It is noteworthy to point out that we only modeled the $\left[Na^+\right]$ at the NCX for a constantly open NaC. We could have modelled the dynamics using a discrete and stochastic Markov model. However, the $\left[Na^+\right]$ sensed by the nearby NCX could only be lower in such a model, than the $\left[Na^+\right]$ we registered with our model.

This results differ significantly from our previous study [7]. Here a computational model of the dyad was used to show that Ca^{2+} flux from reverse mode NCX could precede the LCC in triggering CICR. This discrepancy can be explained by several differences between the two models. We have already pointed out that Lines et al. [7] use a scaled whole cell current to represent the current from a single NaC. At high membrane potentials the open probability for the NaC was high, but the single channel current was low. The combination of high open probability and low single current amplitude will give a comparable high whole cell current, at depolarized membrane potentials. This is a whole cell phenomenon. The current is still small at single channel level, which is reflected in our model. Hilgemann [45] reports that the current amplitude from a single NCX is in the magnitude of 1.0 fA. We have used values from this study to constrain our NCX current, see above. The NCX current included in the model from Lines et al. [7] does not have a similar constrain. This is illustrated by the strength of the NCX current shown in Fig 6 in their study. Here the NCX current peak at $\sim$ 40 pA, which is almost 2 order of magnitude larger than the measured maximal NCX current.

Lines et al. [7] show that the diffusion constant of Na^+ has to be 10^3 nm^2 ms^{-1} or smaller, otherwise the reverse mode NCX cannot trigger CICR. This is a very small value. The diffusion constant of Na^+ is modelled as half that of Ca^{2+}. In Fig. 13 we show the potential effect of a low diffusion constant for Ca^{2+} in the cleft. Here we present the Ca^{2+} response at the mouth of an open RyR, where we have applied a constant current of 0.5 pA. This current corresponds to reported values of single RyR currents from bi-layer experiments [54]. For the low values of the diffusion constant we see that the $\left[Ca^{2+}\right]$ reach clearly un-physiological values. Note that our lowest value for the diffusion constant, is an order of magnitude higher than the cut off value of 10^3 nm^2 ms^{-1} reported by Lines et al. [7].

Our results indicate that Ca^{2+} influx from a single NCX working in reverse mode, cannot trigger CICR alone. This does not rule out the possibilities that Ca^{2+} influx from NCX can modulate the timing of the CICR, as recently discussed by Bers [12]. The experimental results from Lines et al. [7] also support this. Several more hypotheses must be tested to determine the modulatory role of NCX on CICR. Such hypotheses has recently been presented by others [11, 12]. We will briefly mention some of them here: *i*) Ca^{2+} influx from the reverse mode NCX can contribute to the Ca^{2+} content of SR and jSR, sensitising the RyR. *ii*) The Ca^{2+} level in the dyad can be pre-elevated by reverse mode NCX, reducing the time for the LCC to trigger release. *iii*) NCX situated in the dyad can reduce the amount of Ca^{2+} in the cleft after a release, reducing the time the LCCs are inactivated due to Ca^{2+} dependent inactivation. To be able to investigate these hypotheses we need to include RyR release together with a more detailed model of the RyRs in our model. We would probably also need to include a larger diffusional domain, so we could study the Ca^{2+} uptake to SR and jSR. A fourth hypothesis we would like to mention is the possible effects Sarcolemmal buffers could have on the local $\left[Na^+\right]$. Such buffers could possibly hold on to some of the Na^+ comming in through the NaC during a hyperpolarized membrane potential. The Na^+ could then be released during depolarized membrane potentials, when the NCX could utilize it to promote reverse mode.

Conclusion

We have presented a detailed model of the dyadic cleft. The model was used to examine mechanisms underlying the delayed and dyssynchronous activation of Ca^{2+} release from SR during heart failure. We observed that the AP alone can prolong Ca^{2+} release latency by 2 ms, and increase dyssynchrony by 0.5 ms. During heart failure small perturbations of the dyadic geometry, here modeled as an increase of the cleft height, cause a further increase in latency and dyssynchrony. A small increase in cleft height, from 12 nm to 15 nm increased the latency by 5 ms and the dyssynchrony (measured as the standard deviation of the latency) by 1 ms. Larger perturbations of the cleft (cleft with heights of 30 and 40 nm) might render the cleft dysfunctional, since the latest activation time measured in HF cardiomyocyte is smaller or in the same regime, ~ 20 ms, than the latency for these perturbed dyads.

We also co-localized a single NCX with an open NaC, and investigated whether elevated intracellular $\left[Na^+\right]$ could sufficiently promote NCX-mediated Ca^{2+} entry to

trigger Ca^{2+} release. When we applied a hyperpolarized membrane potential we observed a high $\left[Na^{+}\right]$ response $\sim$ 40 mM at the NCX, although NCX current was weak. During depolarized membrane potentials the NCX current is strong, but the $\left[Na^{+}\right]$ from the NaC is small. We also show that slow diffusion, $D\sim 10^4$ nm^2 ms^{-1}, cannot be used to model crowdedness. This has previously been introduced as a way for the dyad to hold on to a high $\left[Na^{+}\right]$ after an opening of the NaC. Such slow diffusion will create un-physiological high values of intracellular $\left[Ca^{2+}\right]$ from a release from SR.

In both of these two studies we used our model to resolve steep local ionic gradients in the dyadic cleft. We have shown that these gradients play a significant role in determine the dynamics of the dyad, and we beleive that models of the dyad needs to resolve these to properly model the dynamics of a single dyad.

5 Appendix

Guy-Chapman/sarcolemmal buffer algorithm

The algorithm used to calculate the static electric potential Φ from the included ions is explained previously in Bers et al. [40] and Soeller and Cannell [30]. However, we found it challenging to implement the algorithm as the explanation is spread over several papers together with the parameters that are used. Here we will lay out the algorithm we ended up using. Note that this is a presentation of the algorithm used to calculate the static potential, and not a full explanation of the model behind it. The reader is advised to look in the above mentioned references for this.

We will first define some useful length scales. First the *Bjerrum length* which defines the length for which the thermal energy equals the Coulombic energy between two unit charges:

$$l_{\mathrm{B}} = \frac{e^2}{4\pi\epsilon_s k_{\mathrm{B}} T}. \tag{11}$$

Second we have the *Debye-Hückel length* or just the *Debye length*, which defines the screening strength in a double layer for low electrostatic potentials. In a 1-1 monovalent electrolyte with strength $c_{1\text{-}1}$ this length is given by:

$$\lambda_{\mathrm{D}}(c_{1\text{-}1}) = \frac{1}{\sqrt{2c_{1\text{-}1} l_{\mathrm{B}} N_A}}. \tag{12}$$

To get this length in nm, we need to multiply what is inside the square root sign with 10^{24} going from l^{-1} to nm^{-3}. For an 1-1 monovalent electrolyte of strength $c_{1\text{-}1} = 155$ mM ($\left[K^{+}\right]$ =140 mM and $\left[Na^{+}\right]$ =15 mM), $\lambda_{\mathrm{D}} \simeq 0.78$ nm. The third length is the Guy-Chapman length:

$$\lambda_{\mathrm{GC}}(\sigma) = \frac{1}{2\pi|\sigma| l_{\mathrm{B}}}, \tag{13}$$

which defines the size of the counter ion layer that has an integrated charge (per nm^2) of $\frac{1}{2}|\sigma|$. The unit of σ is electron charges per nm^2. A $\sigma = 0.4e/\mathrm{nm}^2$ gives a $\lambda_{\mathrm{GC}} \simeq 0.57$ nm. Meaning that half of the surface charges is countered by a layer with counter ions

that is 0.5 nm thick. We are now ready to express the potential $\Phi(z)$ in the solution.

$$\Phi(x_2) = -\frac{2k_{\mathrm{B}}T}{e} \ln \frac{1+\gamma\, \mathrm{e}^{-x_2/\lambda_{\mathrm{D}}}}{1-\gamma\, \mathrm{e}^{-x_2/\lambda_{\mathrm{D}}}} / \Psi_{\mathrm{T}}, \tag{14}$$

where x_2 is the perpendicular distance from the charged surface into the solution and $\Psi_{\mathrm{T}} = k_{\mathrm{B}}T/e$ (the same as Eq. 1). γ is given by:

$$\gamma(\sigma, c_{1\text{-}1}) = -\frac{\lambda_{\mathrm{GC}}(\sigma)}{\lambda_{\mathrm{D}}(c_{1\text{-}1})} + \sqrt{\left(\frac{\lambda_{\mathrm{GC}}(\sigma)}{\lambda_{\mathrm{D}}(c_{1\text{-}1})}\right)^2 + 1}. \tag{15}$$

The expression for Φ can be approximated by a single exponential, $\Phi(x_2) = \Phi_0\, \mathrm{e}^{x_2/\lambda_{\mathrm{D}}}$, see Eq. 2, where Φ_0 is given by:

$$\Phi_0(\gamma) = -\frac{4k_{\mathrm{B}}T}{e} \operatorname{atanh}(\gamma). \tag{16}$$

The individual ion concentrations at the membrane can be calculated from the steady state solution of the Nernst-Planck equation. The i^{th} ion concentration at the membrane is given by:

$$C^i = C_b^i\, \mathrm{e}^{-z^i/\lambda_{\mathrm{D}}\Phi_0}, \tag{17}$$

where c_b^i and z^i is the bulk concentration and the valence of the i^{th} ion. The values for the bulk concentrations we have used for the included ions species is found in Table 1. The ions in the solution close to the membrane will bind to bindings sites at the charged phospholipid head-groups. This is done with a surface association constant Kd for each ion, see Table 1 values used here. The fraction of the available binding sites that a certain ion binds to is governed by:

$$CB^i = \frac{1}{z_i}\left(1 + \frac{\prod_j (1 + C^j/\mathrm{Kd}_j)}{C^i/\mathrm{Kd}_i}\right)^{-1}, \tag{18}$$

where the product is over all cat ions but the i^{th} ion. This equation compares to Eq. 4 in Bers et al. [40]. As the cat-ions bind to the phospholipids the charge density, σ will be reduced. Let PL denote the number of cat-ion binding sites, then is the reduction in charge density due to bound cat-ions:

$$\sigma_b = \mathrm{PL} \sum_i z_i CB^i. \tag{19}$$

The charge density is also reduced by titration of the amino groups of the phospholipids. The amino groups will become deprotonated at higher pH, increasing the surface charge. We will include the same number, type and fraction of phospholipids that Bers et al. [40] do: PS, PC, and PE. See Table 1 for the fractions and names. PC does not have a titratable amino group. The surface charges density available after titration is given by:

$$\sigma_t = \mathrm{PL}\left(\mathrm{PC} + \frac{\mathrm{PE} + \mathrm{PS}}{1 + C^H/\mathrm{K}_{\mathrm{NH}}}\right). \tag{20}$$

Finally we get the total available charge density, after titration and binding of cat-ions from:

$$\sigma = \sigma_t - \sigma_b = \mathrm{PL}\left(\mathrm{PC} + \frac{\mathrm{PE} + \mathrm{PS}}{1 + \mathrm{K_{NH}} C^H} - \sum_i z_i C B^i\right). \tag{21}$$

We are now able to solve for the potential Φ, which we want to use in the advection-diffusion Eq. 3, and to check that it stays approximately constant for a varying $\left[\mathrm{Na}^+\right]$. We choose to set the total amount of phospholipids to PL=563 nmol/mg, so we get the same initial $\Phi_0 = -2.2$ as Soeller and Cannell [30] do. This is ~ 1.5 times the value used in Soeller and Cannell [30]. We chose to do this so we would have comparable electric potentials in our studies. The initial surface charge density is then given by $\sigma_0 = PL \times \mathrm{conv}_\sigma$ =0.54 e/nm^2, see Table 1 for the value used for conv_σ.

We use the bulk ionic concentration, see Table 1 and σ_0 as an initial guess for σ, in Eq. 14. We then evaluate Φ_0, which is used in Eq. 17 to calculate the surface concentration of the ions. Finally these are used in Eq. 21 to calculate a new surface charge density, σ. This procedure is repeated until σ has converged and we have got the static potential Φ.

Table 1: Electric double layer parameters

T	Temperature	22°C
$\left[Ca^{2+}\right]_b^*$	Bulk $\left[Ca^{2+}\right]$	0.1 μM
$\left[Na^+\right]_b$	Bulk $\left[Na^+\right]$	15 mM
$\left[K^+\right]_b$	Bulk $\left[K^+\right]$	140 mM
$\left[Mg^+\right]_b^*$	Bulk $\left[Mg^{2+}\right]$	0.5 mM [40]
$\left[H^+\right]_b$	Bulk $\left[H^+\right]$	0.04 μM (pH 7.4) [40]
$\left[Cl^-\right]_b^{**}$	Bulk $\left[Cl^-\right]$	$\left[Na^+\right]$ +$\left[K^+\right]$
Kd_{Ca}	Ca^{2+} surface association constant	83 mM [30]
Kd_{Na}	Na^+ surface association constant	1600 mM [30]
Kd_K	K^+ surface association constant	3300 mM [30]
Kd_{Mg}	Mg^{2+} surface association constant	166 mM [30]
Kd_H	H^+ surface association constant	2.6 mM
K_{NH}	Deprotonation constant	1.25 $\times 10^{-3}$ mM [40]
PL	Surface concentration of phospholipids	563 nmol/mg
$conv_\sigma$	Conversion between nmol/mg to e/nm^2	9.6$\times 10^{-4}$ [40]
PS	Fraction of phosphatidylserine	0.2 [40]
PC	Fraction of phosphatidylcholine	0.4 [40]
PE	Fraction of phosphatidylethanolamine	0.4 [40]

* The divalent ions are only not included in the Guy-Chapman theory for the diffuse layer. They are only included as reducers of surface charges, while binding to the sarcolemma.

** The actual $\left[Cl^-\right]$ is much smaller, $\sim$ 10 mM, but the value used in the model also includes negatively charged proteins, and is chosen to approximate a monovalent 1-1 electrolyte.

Table 2: Advection diffusion model parameters

T	Temperature	22°C
$D_{Ca^{2+}}$	Diffusion constant of Ca^{2+}	2.2$\times 10^5$ nm^{2}ms^{-1}
D_{Na^+}	Diffusion constant of Na^+	$D_{Ca^{2+}}/2$
$\left[Ca^{2+}\right]_{cyt}$	Cytosolic $\left[Ca^{2+}\right]$	0.1 μM
$\left[Na^+\right]_{cyt}$	Cytosolic $\left[Na^+\right]$	15 mM
$\left[Na^+\right]_{cyt}$	Cytosolic $\left[Na^+\right]$ during heart failure	20 mM [15]
ΔS_{cyt}	Distance to cytosolic concentration	50 nm
k_{on}	On rate for an RyR subunit	0.069 μMms^{-1}

Table 3: Model constants

ϵ_0	Permittivity of free space	8.85e-21 $\frac{\mathrm{C}^2}{\mathrm{Jnm}}$
ϵ_r	Relative static permittivity	80 (water)
ϵ_s	Static permittivity	$\epsilon_0\epsilon_r$
N_A	Avogadro's constant	6.022×10^{20} #/mmole
k_B	Boltzmann's constant	1.38×10^{-23} J/°K

Bibliography

1. Bers, D. M. 2001. Excitation-Contraction Coupling and Cardiac Contractile Force Kluwert Academic, Dordrecht, The Netherlands 2nd edition.

2. Fabiato, A. 1983. Calcium-induced release of calcium from the cardiac sarcoplasmic reticulum. Am. J. Physiol. 245:C1–14.

3. Stern, M. D., Pizarro, G., and Ríos, E. 1997. Local control model of excitation-contraction coupling in skeletal muscle. J Gen Physiol 110:415–440.

4. Cheng, H., Lederer, W. J., and Cannell, M. B. 1993. Calcium sparks: elementary events underlying excitation-contraction coupling in heart muscle. Science 262:740–744.

5. Louch, W. E., Mørk, H. K., Sexton, J., Strømme, T. A., Laake, P., Sjaastad, I., and Sejersted, O. M. 2006. T-tubule disorganization and reduced synchrony of Ca^{2+} release in murine cardiomyocytes following myocardial infarction. J. Physiol. 574:519–533.

6. Harris, D. M., Mills, G. D., Chen, X., Kubo, H., Berretta, R. M., Votaw, V. S., Santana, L. F., and Houser, S. R. 2005. Alterations in early action potential repolarization causes localized failure of sarcoplasmic reticulum Ca^{2+} release. Circ. Res. 96:543–550.

7. Lines, G. T., Sande, J. B., Louch, W. E., Mørk, H. K., Grøttum, P., and Sejersted, O. M. 2006. Contribution of the Na^+/Ca^{2+} exchanger to rapid Ca^{2+} release in cardiomyocytes. Biophys. J. 91:779–792.

8. Blaustein, M. P. and Lederer, W. J. 1999. Sodium/calcium exchange: its physiological implications. Physiol. Rev. 79:763–854.

9. Goldhaber, J. I., Lamp, S. T., Walter, D. O., Garfinkel, A., Fukumoto, G. H., and Weiss, J. N. 1999. Local regulation of the threshold for calcium sparks in rat ventricular myocytes: role of sodium-calcium exchange. J. Physiol. 520 Pt 2:431–438.

10. Satoh, H., Ginsburg, K. S., Qing, K., Terada, H., Hayashi, H., and Bers, D. M. 2000. Kb-r7943 block of Ca^{2+} influx via Na^+/Ca^{2+} exchange does not alter twitches or glycoside inotropy but prevents Ca^{2+} overload in rat ventricular myocytes. Circulation 101:1441–1446.

11. Sher, A. A., Noble, P. J., Hinch, R., Gavaghan, D. J., and Noble, D. 2008. The role of the Na^+/Ca^{2+} exchangers in Ca^{2+} dynamics in ventricular myocytes. Prog Biophys Mol Biol 96:377–398.

12. Bers, D. M. 2008. Calcium cycling and signaling in cardiac myocytes. Annu Rev Physiol 70:23–49.

13. Pieske, B., Maier, L. S., Piacentino, V., Weisser, J., Hasenfuss, G., and Houser, S. 2002. Rate dependence of [Na^+]i and contractility in nonfailing and failing human myocardium. Circulation 106:447–453.

14. Baartscheer, A., Schumacher, C. A., van Borren, M. M. G. J., Belterman, C. N. W., Coronel, R., and Fiolet, J. W. T. 2003. Increased Na^+/H^+-exchange activity is the cause of increased [Na^+]i and underlies disturbed calcium handling in the rabbit pressure and volume overload heart failure model. Cardiovasc Res 57:1015–1024.

15. Pogwizd, S. M., Sipido, K. R., Verdonck, F., and Bers, D. M. 2003. Intracellular na in animal models of hypertrophy and heart failure: contractile function and arrhythmogenesis. Cardiovasc Res 57:887–896.

16. Maier, L. S. and Hasenfuss, G. 2006. Role of $[Na^+]_i$ and the emerging involvement of the late sodium current in the pathophysiology of cardiovascular disease Eur Heart J Suppl 8:A6–9.

17. Semb, S. O. and Sejersted, O. M. 1996. Fuzzy space and control of Na^+, K^+-pump rate in heart and skeletal muscle. Acta Physiol. Scand. 156:213–225.

18. Cingolani, H. E. and Ennis, I. L. 2007. Sodium-hydrogen exchanger, cardiac overload, and myocardial hypertrophy. Circulation 115:1090–1100.

19. Bers, D. M. 2006. Altered cardiac myocyte ca regulation in heart failure. Physiology (Bethesda) 21:380–387.

20. Poláková, E., Zahradníková, A., Pavelková, J., Zahradník, I., and Zahradníková, A. 2008. Local calcium release activation by dhpr calcium channel openings in rat cardiac myocytes. J Physiol 586:3839–3854.

21. Song, L. S., Wang, S. Q., Xiao, R. P., Spurgeon, H., Lakatta, E. G., and Cheng, H. 2001. β-adrenergic stimulation synchronizes intracellular Ca^{2+} release during excitation-contraction coupling in cardiac myocytes. Circ. Res. 88:794–801.

22. Altamirano, J. and Bers, D. M. 2007. Voltage dependence of cardiac excitation-contraction coupling: unitary Ca^{2+} current amplitude and open channel probability. Circ Res 101:590–597.

23. Bridge, J. H. B., Torres, N. S., and Sobie, E. A. 2008. New insights into the structure and function of couplons. J Physiol 586:3735.

24. Greenstein, J. L. and Winslow, R. L. 2002. An integrative model of the cardiac ventricular myocyte incorporating local control of Ca^{2+} release. Biophys. J. 83:2918–2945.

25. Guia, A., Stern, M. D., Lakatta, E. G., and Josephson, I. R. 2001. Ion concentration-dependence of rat cardiac unitary l-type calcium channel conductance. Biophys J 80:2742–2750.

26. Finsen, A. V., Christensen, G., and Sjaastad, I. 2005. Echocardiographic parameters discriminating myocardial infarction with pulmonary congestion from myocardial infarction without congestion in the mouse. J. Appl. Physiol. 98:680–9.

27. Mørk, H. K., Sjaastad, I., Sejersted, O. M., and Louch, W. E. 2009. Slowing of cardiomyocyte Ca^{2+} release and contraction during heart failure progression in postinfarction mice. Am J Physiol Heart Circ Physiol 296:H1069–H1079.

28. Hake, J. and Lines, G. T. 2008. Stochastic binding of Ca^{2+} ions in the dyadic cleft; continuous versus random walk description of diffusion. Biophys. J. 94:4184–4201.

29. Peskoff, A., Post, J. A., and Langer, G. A. 1992. Sarcolemmal calcium binding sites in heart: II. mathematical model for diffusion of calcium released from the sarcoplasmic reticulum into the diadic region. J. Membr. Biol. 129:59–69.

30. Soeller, C. and Cannell, M. B. 1997. Numerical simulation of local calcium movements during l-type calcium channel gating in the cardiac diad. Biophys. J. 73:97–111.

31. Franzini-Armstrong, C., Protasi, F., and Ramesh, V. 1999. Shape, size, and distribution of Ca^{2+} release units and couplons in skeletal and cardiac muscles. Biophys. J. 77:1528–1539.

32. Wagenknecht, T., Radermacher, M., Grassucci, R., Berkowitz, J., Xin, H. B., and Fleischer, S. 1997. Locations of calmodulin and fk506-binding protein on the three-dimensional architecture of the skeletal muscle ryanodine receptor. J. Biol. Chem. 272:32463–32471.

33. Tanskanen, A. J., Greenstein, J. L., Chen, A., Sun, S. X., and Winslow, R. L. 2007. Protein geometry and placement in the cardiac dyad influence macroscopic properties of calcium-induced calcium release. Biophys. J. 92:3379–3396.

34. Bers, D. M. and Stiffel, V. M. 1993. Ratio of ryanodine to dihydropyridine receptors in cardiac and skeletal muscle and implications for e-c coupling. Am J Physiol 264:C1587–C1593.

35. Koh, X., Srinivasan, B., Ching, H. S., and Levchenko, A. 2006. A 3D Monte Carlo analysis of the role of dyadic space geometry in spark generation. Biophys. J. 90:1999–2014.

36. McLaughlin, S. G., Szabo, G., and Eisenman, G. 1971. Divalent ions and the surface potential of charged phospholipid membranes. J. Gen. Physiol. 58:667–687.

37. Langner, M., Cafiso, D., Marcelja, S., and McLaughlin, S. 1990. Electrostatics of phosphoinositide bilayer membranes. theoretical and experimental results. Biophys. J. 57:335–349.

38. Grahame, D. C. 1947. The electrical double layer and the theory of electrocapillarity. Chem Rev 41:441–501.

39. Andelman, D. 1995. Electrostatic properties of membranes: the poisson-boltzmann theory in R. Lipowsky and E. Sackmann, editors, Structure and Dynamics of Membranes; Handbook of Biological Physics volume 1 pages 603–642 North Holland.

40. Bers, D. M., Philipson, K. D., and Peskoff, A. 1985. Calcium at the surface of cardiac plasma membrane vesicles: cation binding, surface charge screening, and Na-Ca exchange. J. Membr. Biol. 85:251–261.

41. Post, J. A. and Langer, G. A. 1992. Sarcolemmal calcium binding sites in heart: I. molecular origin in "gas-dissected" sarcolemma. J. Membr. Biol. 129:49–57.

42. Keener, J. and Sneyd, J. 1998. Mathematical Physiology Springer.

43. Patlak, J. B. 1988. Sodium channel subconductance levels measured with a new variance-mean analysis. J Gen Physiol 92:413–430.

44. Shannon, T. R., Wang, F., Puglisi, J., Weber, C., and Bers, D. M. 2004. A mathematical treatment of integrated ca dynamics within the ventricular myocyte. Biophys. J. 87:3351–3371.

45. Hilgemann, D. W. 1996. Unitary cardiac Na^+, Ca^{2+} exchange current magnitudes determined from channel-like noise and charge movements of ion transport. Biophys J 71:759–768.

46. Jafri, M. S., Rice, J. J., and Winslow, R. L. 1998. Cardiac Ca^{2+} dynamics: the roles of ryanodine receptor adaptation and sarcoplasmic reticulum load. Biophys. J. 74:1149–68.

47. Brooks, A. N. and Hughes, T. J. R. 1982. Streamline upwind/petrov-galerkin formulations for convection dominated flows with particular emphasis on the incompressible navier-stokes equations Computer Methods in Applied Mechanics and Engineering 32:199–259.

48. Balay, S., Buschelman, K., Eijkhout, V., Gropp, W. D., Kaushik, D., Knepley, M. G., McInnes, L. C., Smith, B. F., and Zhang, H. 2004. PETSc users manual Technical Report ANL-95/11 - Revision 2.1.5 Argonne National Laboratory.

49. Gillespie, D. T. 1977. Exact stochastic simulation of coupled chemical reactions J. Phys. Chem. 81:2340–2361.

50. Alfonsi, A., Cancès, E., Turinici, G., Di Ventura, B., and Huisinga, W. 2005. Exact simulation of hybrid stochastic and deterministic models for biochemical systems Technical report INRIA, Institut national de recherche en informatique et en automatique.

51. Rüdiger, S., Shuai, J. W., Huisinga, W., Nagaiah, C., Warnecke, G., Parker, I., and Falcke, M. 2007. Hybrid stochastic and deterministic simulations of calcium blips. Biophys. J. 93:1847–1857.

52. Zahradník, I., Györke, S., and Zahradníková, A. 2005. Calcium activation of ryanodine receptor channels–reconciling RyR gating models with tetrameric channel structure. J. Gen. Physiol. 126:515–527.

53. Laver, D. R. and Honen, B. N. 2008. Luminal Mg^{2+}, a key factor controlling RYR2-mediated Ca^{2+} release: cytoplasmic and luminal regulation modeled in a tetrameric channel. J Gen Physiol 132:429–446.

54. Mejía-Alvarez, R., Kettlun, C., Ríos, E., Stern, M., and Fill, M. 1999. Unitary Ca^{2+} current through cardiac ryanodine receptor channels under quasi-physiological ionic conditions. J. Gen. Physiol. 113:177–186.

55. Wang, S. Q., Stern, M. D., Ríos, E., and Cheng, H. 2004. The quantal nature of Ca^{2+} sparks and in situ operation of the ryanodine receptor array in cardiac cells. Proc. Natl. Acad. Sci. U. S. A. 101:3979–3984.